PRACTICAL WORKFLOWS FOR MICROFLUIDIC DEVICE DESIGN AND FABRICATION FOR MOLECULAR DIAGNOSTICS

by

Camden Jameson Long

A thesis submitted in partial fulfillment
of the requirements for the degree

of

Master of Science

in

Bioengineering

MONTANA STATE UNIVERSITY
Bozeman, Montana

August 2025

©COPYRIGHT

by

Camden Jameson Long

2025

All Rights Reserved

DEDICATION

To my loving and supportive wife, Grace—

I could never have done all of this without your unwavering encouragement and countless sacrifices.

ACKNOWLEDGEMENTS

First and foremost, I would like to express my deepest gratitude to Dr. Stephanie McCalla for her unwavering support and mentorship. I am truly grateful for the opportunities you have afforded me, the patience you have shown, and your guidance in helping me grow into the scientist I am today.

I would also like to thank Dr. Jennifer Brown for teaching me how to strengthen my mentoring relationships and develop lifelong practices in mindfulness. These invaluable skills have not only enriched me professionally, but personally as well.

To the many faculty and staff who took a personal interest in my project and played an integral role in my training—Dr. Andrew Lingley, Dr. Joshua Heineman, and Dr. Stephan Warnat—thank you for your time, guidance, and wisdom.

I am especially thankful to the incredible researchers and friends who have collaborated on this work: Dr. Michael Neubauer, Matthew Culp, and Grace Ducharme. Your insights, effort, and camaraderie have made this journey more impactful and enjoyable.

Lastly, I would like to acknowledge my fellow graduate students in the McCalla Lab. Malek Chreiki, thank you for being there through all the late-night projects, whether we were fixing a fridge or running acrylamide gels. Your willingness to jump in and support without hesitation never went unnoticed. To Esther Stopps—thank you for your support, guidance, and friendship. You've always been there to listen and help me push through the toughest days, and I'm deeply grateful for that.

TABLE OF CONTENTS

1. INTRODUCTION 1

Motivation 1
Thesis Outline 3
Background: Rapid Prototyping in Microfluidics 4
Soft Lithography and Other Replication Methods 4
3D Printed Microfluidics 6
Thermoplastics in Microfluidics 7
Direct Structuring Methods for Rapid Prototyping Microfluidics 9
Micromilling in COC 9
Research Goals, Hypotheses and Objectives 11

2. FABRICATION AND EVALUATION OF 3D PRINTED MICROFLUIDIC DEVICES FOR MOLECULAR DIAGNOSTICS 13

Introduction 13
Materials and Methods 15
Microfluidic Device Fabrication 15
Printing on Glass 15
Bonding Strategy Evaluation 16
Bonding to spin-coated glass cover slip 16
Bonding to substrate using double-sided adhesive 18
Fabrication of custom chip-to-world apparatus 19
Thermal Stability Assessments 20
Additional post-processing 20
Results and Discussion 21
Dimensional Fidelity of 3D Printed Devices 21
Integrity of 3D Printed Microchannels 21
Bonding Evaluation 24
Thermal Stability of 3D Printed Devices 28
Custom chip-to-world interface 28
Additional Post Processing 30
Conclusions and Future Work 32

3. A LOW-COST WORKFLOW FOR MICROMILLING CYCLIC-OLEFIN COPOLYMER DEVICES FOR NUCLEIC ACID DETECTION 34

Contribution of Authors and Co-Authors 34
Manuscript Information 35
Introduction 36

TABLE OF CONTENTS – CONTINUED

Materials and Methods 39
Fabricating Machinable COC Plaques by Hot Embossing 39
Micromachining 40
Tool Selection 40
Zeroing the Workpiece and Tool Loading 41
Computer-Aided Machining (CAM) 42
Toolpath Selection 42
Post Processing of Micromilled COC Chips 45
Surface Characterization 45
Roughness Measurements 45
Flatness Measurements 45
Evaluating Optimal Milling Parameters 45
Sealing the Chip 46
Chip-To-World Interface 46
Recombinase Polymerase Amplification in Micromilled COC 47
Temperature Control and Real-Time Fluorescent Imaging 48
Real-Time Fluorescence Analysis 48
Results and Discussion 48
Fabricating Machinable COC Plaques by Hot Embossing 48
Evaluating Optimal Milling Parameters 50
Machining Different Example Geometries 53
Importance of Workpiece Flatness 53
Drilling Inlets and Outlets 55
Milling Microchannels and Complex Geometries 55
Recombinase Polymerase Amplification in Micromilled COC Chip 58
Conclusion 61

4. FUTURE WORK: HOT EMBOSSING CYCLIC-OLEFIN COPOLYMER MICROFLUIDIC DEVICES FOR DIGITAL NUCLEIC ACID DETECTION 65

Introduction 65
Materials and Methods 68
Multiple Depth Photolithography 68
Surface Characterization of SU-8 Master 71
Machining Custom PMMA Frame and Aluminum Frame 71
PDMS Master Mold Fabrication 72
Hot Embossing COC Sheets 72
Device Characterization 73
Results and Discussion 73

TABLE OF CONTENTS – CONTINUED

Soft-Lithography For PDMS Master Fabrication 73
Hot Embossing Using A PDMS Master Mold 73
Conclusions and Future Work 75

5. CONCLUSIONS 79

REFERENCES CITED 81

LIST OF TABLES

Table Page

1. Table 1 Recommended printing parameters for silanized glass substrates (10 μm slice thickness) using the MiiCraft 50 DLP 3D printer and Bv007a resin. 17

2. Table 2 Summary of Parameters for embossing plaques from grade 8007 and 6013 TOPAS cyclic-olefin copolymer (COC). 49

3. Table 3 Recommended range of feeds and speeds for slotting operations in COC. 53

4. Table 4 Multi-Depth Photolithography SU-8 Spin Coating Parameters for Each Layer 71

5. Table 5 Summary of parameters for hot embossing COC sheets and pellets using the protocol summarized in Figure 30. 72

LIST OF FIGURES

Figure Page

1. Figure 1 Illustration of significant events in the history of microfluidics 2
2. Figure 2 Illustration of key characteristics of PDMS. Illustration made using BioRender. 4
3. Figure 3 Illustration of the photolithography and subsequent soft lithography microfluidic fabrication technique pioneered by George Whitesides in 1998.[8] 5
4. Figure 4 Schematic illustrating the differences between (A) stereolithography, (B) digital light processing and (C) liquid crystal display 3D printing. Image reproduced from Schittecatte et al. [20]. 7
5. Figure 5 A summary of citations using PDMS compared to other thermoplastics since the inception of polymer microfluidics in 1990.Giri and Tsao [9]. 8
6. Figure 6 Illustration to show the difference in three common direct structuring methods for fabricating microfluidic devices in thermoplastics: micromilling, xurography, and laser ablation. Illustration from [24] 10
7. Figure 7 Illustration of key characteristics of COC. Illustration made using BioRender. 11
8. Figure 8 Schematic of the glass silanization protocol to prepare glass slide to be used as the substrate for printing on glass.[36] 16
9. Figure 9 Schematic of the two bonding strategies evaluated for bonding 3D printed devices to glass cover slips using resin as an adhesive layer. 18
10. Figure 10 Schematic of the double-sided pressure sensitive adhesive bonding strategy. 19
11. Figure 11 Schematic of the prototype chip-to-world apparatus. 20
12. Figure 12 Field-emission scanning electron microscope (FE-SEM) images of 3D printed microfluidic channels. The CAD designed width is compared to the measured width and the measured with is much larger than the designed width. 22

LIST OF FIGURES – CONTINUED

Figure Page

13. Figure 13 Schematic of tilt mechanism used in MiiCraft 50 DLP 3D Printer. 23

14. Figure 14 Field-emission scanning electron microscope (FE-SEM) images of defects that are common due to the tilt and lift mechanism of bat-style digital light projection (DLP) 3D printers. 24

15. Figure 15 Schematic of the effects adhesive have on rough surfaces when bonding microfluidics devices. 25

16. Figure 16 Images of the failures for bonding devices to a spin coated glass slide. 26

17. Figure 17 Image of 3D printed device bonded to PMMA using doulbe-sided pressure sensitive adhesive. 27

18. Figure 18 Images of 3D printed microfluidic devices filled with water before and after two heating treatments 27

19. Figure 19 Images of functional clamp for filling and heating microfluidic devices fabricated using the EPAX 3D X1 4k 3D printer using eSUN PLA Pro resin. 29

20. Figure 20 UV/vis spectra of leachate from 3D printed devices. 31

21. Figure 21 Schematic of the CNC milling process. 38

22. Figure 22 Detailed schematic for the fabrication of cyclic-olefin copolymer (COC) plaques by hot embossing. 40

23. Figure 23 Summary of toolpathing methods used to manufacture microfluidic features. 44

24. Figure 24 Image and schematic of custom chip-to-world interface. 47

25. Figure 25 Summary of average roughness across 200 μm straight channels in grade 6013 and 8007 COC. 54

26. Figure 26 Comparison of complex geometries that were micromilled in grade 8007 cyclic-olefin copolymer (COC) compared to 6013 COC. 57

27. Figure 27 Quantitative results from real-time RPA on chip compared to RPA in tubes. 60

LIST OF FIGURES – CONTINUED

Figure Page

28. Figure 28 Schematic of the injection molding fabrication process. 66

29. Figure 29 Schematic of the hot embossing fabrication process. The mold and thermoplastic is first preheated, then the mold is pressed into the thermoplastic for several minutes. Then, the mold and thermoplastic are allowed to cool and then they are separated. 67

30. Figure 30 Detailed schematic of the hot embossing fabrication process with the PDMS master mold. 69

31. Figure 31 Summary schematic of multi-depth soft-lithography. 70

32. Figure 32 Optical profilometry result of multiple-depth SU-8 master. 74

33. Figure 33 Images of grade 8007 COC hot embossed using a PDMS master. 76

34. Figure 34 Detailed schematic of the proposed hot embossing fabrication process with the epoxy master mold. 77

ABSTRACT

Rapid design and fabrication of microfluidic devices is essential for accelerating the development of molecular diagnostic tools. However, there is a gap between academic prototyping and the refined fabrication methods needed for scalable, industrial production. This thesis addresses that challenge by evaluating and refining two rapid prototyping workflows for creating microfluidic devices: digital light processing (DLP) 3D printing and micromilling in cyclic-olefin copolymer. Then, future work is proposed for scaling manufacturing by hot embossing COC. First, DLP 3D printing was performed with a commercially available printer (MiiCraft 50) and resin (CADworks3D clear microfluidic resin V0.7a) to produce curved microchannels less than 100 µm in width. A comprehensive workflow is presented for accessible fabrication and device integration, including design strategies, bonding methods, thermal stability evaluation, and development of a prototype chip-to-world interface. Postprocessing treatments were also investigated to determine whether toxic inhibitory chemicals could be leached from the resin, with the goal of improving compatibility with sensitive biochemical assays. Second, a low-cost workflow for micromilling COC devices was developed using a desktop CNC mill (Nomad 3, Carbide 3D). By prototyping directly in an industry standard material, this approach facilitates smoother scaling to commercial manufacturing. A method was established for fabricating machinable COC plaques and critical milling parameters were evaluated to enable reproducible fabrication of complex microchannels as small as 200 µm. Then, a refined chip-to-world interface was designed and used to perform proof-of-concept recombinase polymerase amplification (RPA) within the micromilled chips. Third, hot embossing was evaluated as scalable manufacturing technique suitable for resource limited academic settings. Initial tests using PDMS molds were limited by mold deformation under heat and pressure, motivating future work a rigid epoxy mold to improve resolution and reliability. In conclusion, this thesis presents accessible, reproducible methods for fabricating microfluidic devices tailored for diagnostic applications. Ultimately, these workflows aim to lower technical barriers and accelerate the path from research innovation to practical impact.

1

INTRODUCTION

Motivation

Molecular biologist Thomas Brock discovered the thermophilic bacterium *Thermus aquaticus* in a Yellowstone National Park hot spring in 1966—a finding that later enabled one of the greatest revolutions in molecular diagnostics.[1] Nearly 17 years later, another now-infamous scientist, Kary Mullis, conceived the idea for incorporating the polymerase enzyme from *Thermus aquaticus* (Taq Polymerase) into the polymerase chain reaction (PCR), an existing method for the exponential amplification of DNA. At the time, PCR required researchers to manually add new polymerase enzyme after each heating cycle. Because Taq polymerase was isolated from a hot spring, it can naturally withstand the high temperatures in PCR without denaturing. Thus, its addition to the PCR reaction made the process far more efficient and allowed for complete automation. Mullis was later awarded the Nobel Prize in Chemistry in 1993 for his contributions to this work.[2–4]

PCR has since become a ubiquitous technology used for molecular diagnostics, particularly following its widespread use during the COVID-19 pandemic. For many, the pandemic underscored the immense utility of molecular diagnostics in detecting pathogens quickly and accurately.

One of the most transformative technologies of rapid, decentralized testing is microfluidics—miniaturized systems that manipulate fluids at the microliter to picoliter scale. These systems enable point-of-care diagnostics, which are tests that can be administered and interpreted near or at the site of patient care, without the need for centralized laboratory infrastructure.

The first example of commercially available microfluidics in molecular diagnostics was

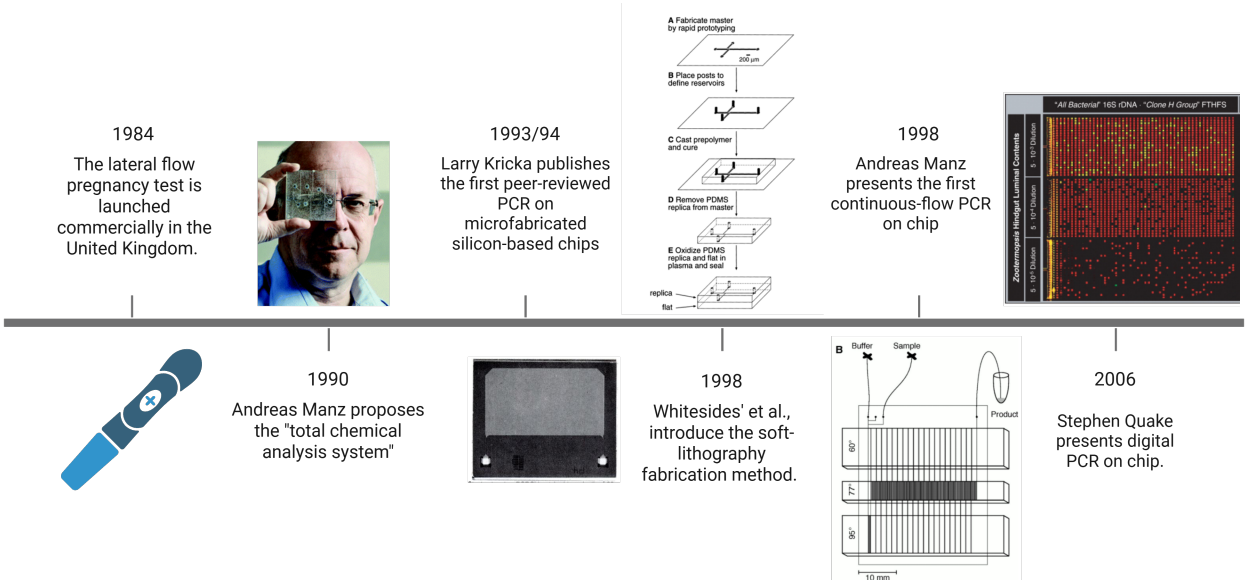


Figure 1: Illustration of significant events in the history of the development of microfluidics for molecular diagnostics. Illustration made using BioRender.

the lateral flow pregnancy test, which launched in 1984 in the United Kingdom.[5] This early innovation trailblazed the path for modern point-of-care and at-home microfluidic assays. Shortly after, Andreas Manz proposed the "total chemical analysis system" which was the seminal paper for polymer microfluidics.[6] Then in 1998, Manz presented the first continuous-flow PCR on chip, enabling PCR in under 15 minutes ([7]). Since then, the demand for accessible and rapid diagnostic tests has fueled global research collaboration to develop novel microfluidic platforms for molecular assays (Figure 1).

However, a major barrier to the widespread development of these technologies remains the difficulty of fabrication and the time-intensive nature of research and development. In this thesis, two rapid prototyping methods are presented that enable device fabrication from inception to a functional prototype within hours. Finally, directions for future research are proposed to bridge the gap between academic innovation and industrial adoption in the field of microfluidic-based diagnostics.

Thesis Outline

Chapter 1: Introduces the fabrication of microfluidic systems, with an emphasis on rapid prototyping methods such as 3D printing and micromilling. The chapter concludes by outlining clear research goals, hypotheses, and objectives that are addressed in Chapters 2–4.

Chapter 2: Details a fabrication strategy for microfluidic devices using digital light processing (DLP) 3D printing. Design constraints and printing parameters are discussed for producing sub-100 μm complex microchannels using a commercially available printer and resin. Groundwork is laid for future work evaluating post-processing techniques to enhance compatibility with sensitive diagnostic assays.

Chapter 3: Presents a practical, low-cost workflow for micromilling cyclic-olefin copolymer (COC) to create high-quality, complex microfluidic architectures. Manufacturing guidelines are provided, followed by the development of a custom chip-to-world interface for coupling devices to macro-scale fluidic fittings and a thermal stage. The chapter concludes by establishing a foundation for quantitative on-chip isothermal nucleic acid detection.

Chapter 4: Evaluates a fabrication method for hot embossing COC using a PDMS master mold. It includes detailed steps for producing multi-depth SU-8 molds and characterizing the quality of embossed COC devices. Future work proposes a mid-throughput manufacturing approach to bridge the gap between prototyping and industrial translation.

Chapter 5: Summarizes key conclusions and highlights future research directions. Additional efforts to develop practical bioanalytical assays in both 3D printed and micromilled devices are reviewed. The chapter concludes with a forward-looking perspective on refining the previously discussed microfluidic devices for integration with molecular diagnostics.

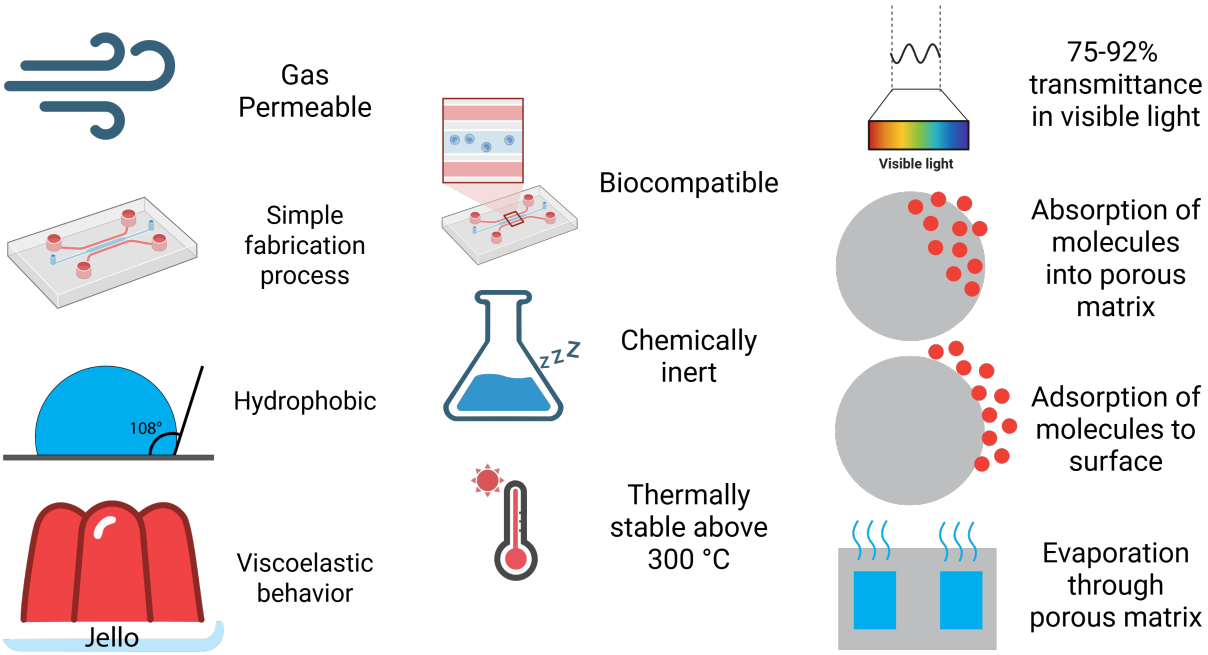


Figure 2: Illustration of key characteristics of PDMS. Illustration made using BioRender.

Background: Rapid Prototyping in Microfluidics

Soft Lithography and Other Replication Methods

In 1998, George Whitesides introduced the soft lithography fabrication method, which utilized microfabrication techniques to create a microfluidic device out of poly(dimethylsiloxane), or PDMS for short. In this landmark paper, "Rapid Prototyping of Microfluidic Systems in Poly(dimethylsiloxane)," the first method for soft-lithography is presented which enabled scientists to fabricate microfluidic devices within 24 hours.[8] Soft-lithography, a now widely adopted process, first requires the production of a rigid master mold commonly fabricated by photolithography using SU-8, an epoxy-based light sensitive resin (Figure 3). Then, PDMS is poured over the top of the patterned features to form the microfluidic device. With the advent of this technology, PDMS and soft lithography effectively took over the field with over 13,000 citations between its inception in 1998 and 2021.[9]

Despite its widespread adoption, there are several drawbacks to PDMS for many

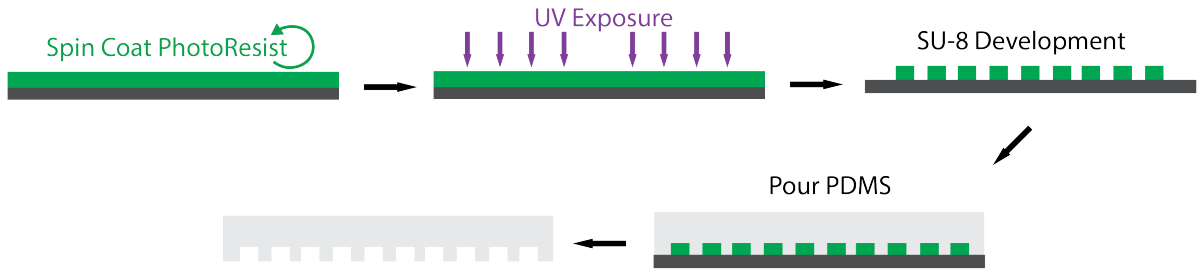


Figure 3: Illustration of the photolithography and subsequent soft lithography microfluidic fabrication technique pioneered by George Whitesides in 1998.[8] First, a photoresist is spin coated onto a substrate. Then, UV light is selectively exposed though a light mask to pattern the substrate. The unpolymerized photoresist is removed with a chemical solvent, called developer, leaving the polymerized photoresist patterned on the substrate. Lastly, poly(dimethylsiloxane) (PDMS) is poured atop the master to transfer the pattern into the PDMS.

sensitive bioanalytical applications (Figure 2). One of the most significant of these is that PDMS can both adsorb molecules to its surface and absorb molecules into its porous matrix.[10,11] Evaporation and absorption of liquids and small molecules can have significant detrimental effects on many applications of microfluidics. For example, Toepke and Beebe [10] point out how small-molecule permeability in PDMS presents a critical flaw in utilizing it for many sensitive applications such as drug-screening assays [10,11]. PDMS can also adsorb biopolymers, like proteins, to its surface.[12] For bioanalytical reactions, which rely on proteins as the molecular machinery to perform the reaction, this adsorption may cause reaction inhibition. Along with its absorption/absorption characteristics, evaporation of aqueous solutions through PDMS has been observed.[10,11]. For many biochemical reactions such as PCR, the reaction is heated to nearly boiling which can significantly increase diffusion through the PDMS matrix and evaporation. In conclusion, unmodified PDMS is not a viable option for the development of sensitive bioanalytical assays because of its characteristics adsorption/absorption and evaporation.

Although the Whitesides group dubbed soft-lithography a “rapid prototyping” method,

in a modern context, this is not the case. Although the fabrication of the PDMS device requires only a few hours, the up front cleanroom costs and time investments for fabricating the master mold turn the prototyping process into a time-consuming and resource-intensive task. The cleanroom-based lithography process is a costly and time consuming process which requires trained, experienced personnel to operate equipment. In contrast, over the past two decades, several bench top microfabrication techniques have emerged which can produce functional prototypes within hours. Further, some have not only been widely adopted for rapid prototyping but also as a cleanroom replacement for producing master molds for soft lithography.

3D Printed Microfluidics

The most common rapid prototyping technique in microfluidics is 3D printing. There are many different types of 3D printing utilized for fabricating microfluidic devices: Selective Laser Sintering, Fused Deposition Modeling, Photopolymer Inkjet Printing, Three-Dimensional Printing, Laminated Object Manufacturing and Stereolithography.[13]

Of these methods, resin-based 3D printing has become very popular because it can produce the smoothest and highest resolution features.[14,15] There are three main types of resin 3D printing technologies: stereolithography (SLA), digital light processing (DLP), and liquid crystal display (LCD) (Figure 4). For stereolithography (SLA) 3D printing, a laser scans across the design to selectively cure the resin pixel by pixel. Digital light processing (DLP) 3D printing reflects the light source off of a projected image to expose microfeatures layer-by-layer. In LCD 3D printing, the channel microstructures are patterned by light emitted an LCD.

With recent advancements in technology, resin-based 3D printers have become much more affordable with printers available for less than $500 that are capable of achieving less than 100 μm feature resolution.[16] The affordability of these printers can be attributed to

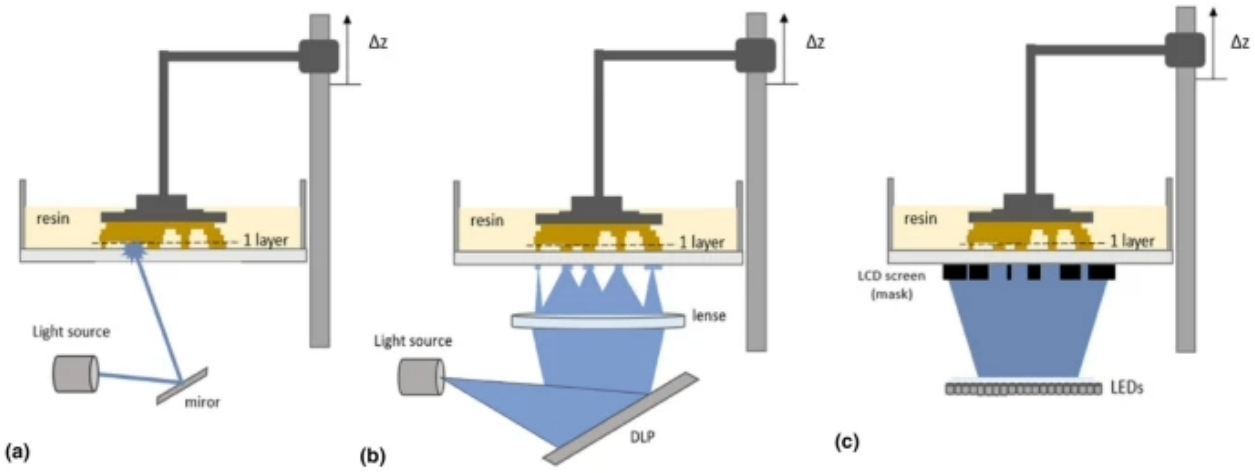


Figure 4: Schematic illustrating the differences between (A) stereolithography, (B) digital light processing and (C) liquid crystal display 3D printing. Image reproduced from Schittecatte et al. [20].

the improvements to the LCD technology, which are working to maximize the number of pixels possible on the display. Further, 3D printing technology requires simple operation and can produce grassroots prototypes within a few hours. However, 3D printing is not ideal for many biological and biochemical applications. This is mainly due to the leaching of residual photoinitiators or uncured monomers into the working fluid.[17] These compounds have been shown to inhibit PCR amplification–specifically polymerase enzymes–rendering 3D printed devices often incompatible with many molecular diagnostic reactions.[18,19] In one study, the effects of post-processing 3D printed polymers on PCR found that basic post-processing significantly inhibited PCR product formation, but additional post-processing with hot water and extensive UV curing protected from this inhibition.[19] Further, it has been demonstrated that even recent biocompatible or medical-grade resins may still leach enough contaminants to interfere with sensitive applications.[17]

Thermoplastics in Microfluidics

Microfabrication techniques such as soft lithography and resin 3D printing have become ubiquitous among microfluidic scientists and researchers, but they have not been as widely

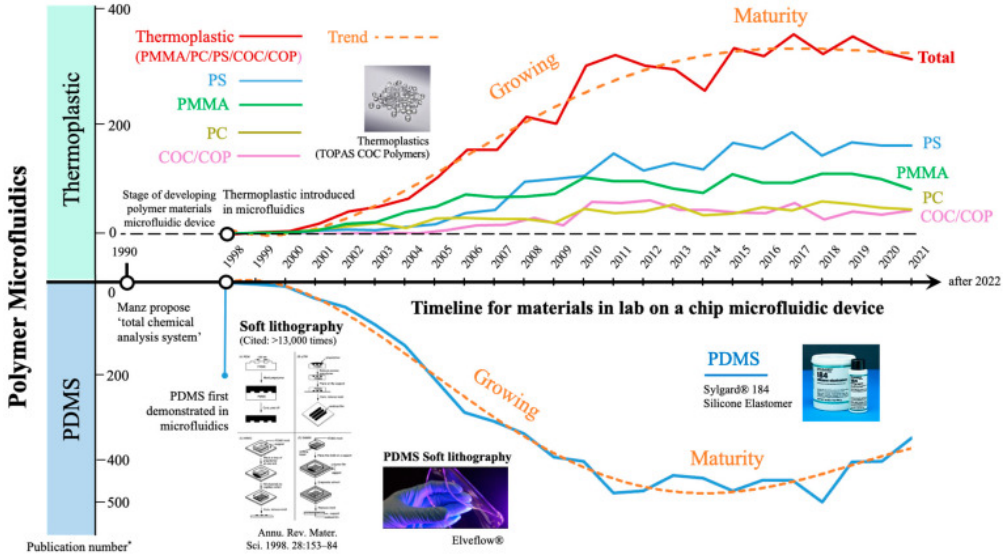


Figure 5: A summary of citations using PDMS compared to other thermoplastics since the inception of polymer microfluidics in 1990. Data was collected using the Web of Science database through December of 2021 by Giri and Tsao [9]. Figure reproduced from Giri and Tsao [9].

adopted in industry. Edge Precision Manufacturing and Potomac microfluidics, industry leaders in plastic-based micro-manufacturing, describe a bottleneck in commercial translation of PDMS due to the low-throughput fabrication and poor scalability.[21,22] Concerns with chemical and biological compatibility, as well as low through-put fabrication also inhibit clinical translation of 3D printed devices. As a result, industry manufacturers of biomedical microfluidic devices, like Edge Precision Manufacturing and Potomac, have made the switch to thermoplastics–namely cyclic-olefin copolymer/polymer (COC/COP), poly(methyl methacrylate) (PMMA) and polycarbonate (PC).[21,22] Thermoplastics have been so widely adopted in industry for their high-throughput manufacturability, and low cost-per-unit at scale.[23] However, thermoplastics are much less prevalent in academia: the cumulative number of citations for PDMS is approximately equivalent to the sum of all of the citations for PC, PMMA, COC/COP and PS from 1998-2021 (Figure 5).[9]

Direct Structuring Methods for Rapid Prototyping Microfluidics

Direct structuring fabrication methods involve removing material from base stock material to fabricate microfluidics devices. Of these rapid prototyping methods, there are three main methods: laser ablation, xurography, and micromilling.[24] Laser ablation utilizes computer numerical control (CNC) to manipulate a CO_2 or UV laser to selectively remove material. This method has been adopted industrially by Paul Yager, a professor at the University of Washington, who started a company called Micronics who specialized in laser-cut microfluidic devices for molecular diagnostics.[25] However, the largest drawback of laser ablation are poor surface finish and thermal damage from the laser.[26] In contrast, Xurography utilizes a digital cutter plotter that cuts polymers using a blade, then the cut thermoplastic can be laminated on both sides to form the channels.[24] This method is increasing in popularity especially due to companies such as adhesives research who advertise double-sided pressure sensitive adhesive which is made specifically for this application. Lastly, micromachining or micromilling is a direct structuring method that utilizes a CNC router to control micro end mills to remove material from the substrate.[19,24] This method can be quite costly with expensive custom machinery, but with the recent advancements of low-cost desktop CNCs, micromilling is a viable low-cost rapid prototyping method.Direct structuring methods are advantageous over soft-lithography and 3D printing because they allow researchers to prototype in the end-use material that is utilized for industrial technologies.

Micromilling in COC Cyclic-Olefin Copolymer (COC) offers significant advantages for microfluidics due to its chemical inertness, biological compatibility, optical clarity, and high thermal stability (Figure 7).[24] These properties make COC and excellent material choice for many microfluidic applications. However, traditional fabrication methods for COC, such as hot embossing and injection molding, require costly equipment and are time consuming,

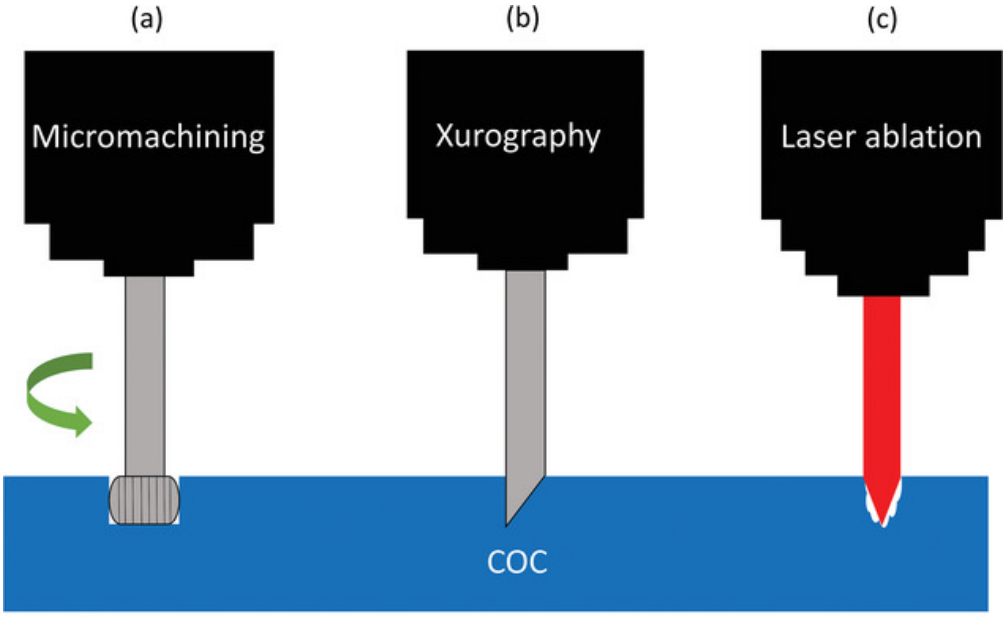


Figure 6: Illustration to show the difference in three common direct structuring methods for fabricating microfluidic devices in thermoplastics: micromilling, xurography, and laser ablation. Illustration from [24]

limiting accessibility for many labs and prototyping environments.[27,28]

For rapid prototyping, direct structuring methods like laser ablation, xurography and micromilling allow single device fabrication with greater fabrication flexibility compared to traditional thermoplastic fabrication methods. Among these, micromilling is particularly promising. Micromilling has demonstrated the ability to achieve feature sizes as small as 30 microns, comparable to the precision of indirect methods like hot embossing and injection molding.[28] However, previously presented methods utilize expensive, often custom specialty micro-CNCs, which makes micromilling appear inaccessible due to equipment costs and complexity.[29–31] Additionally, due to the high variability between CNC machines and tools, practical guidance for fabrication is limited.

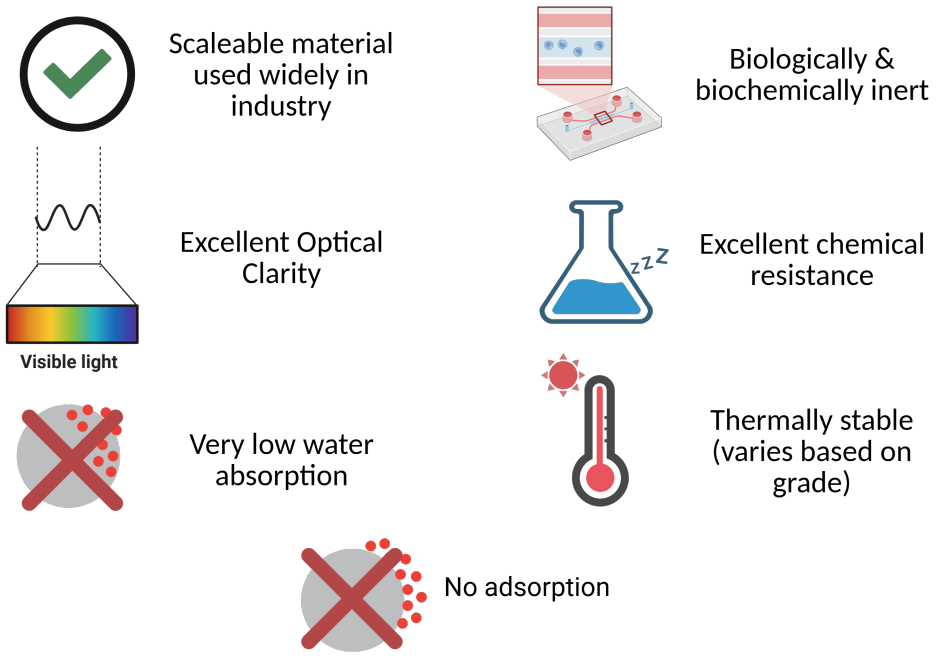


Figure 7: Illustration of key characteristics of COC. Illustration made using BioRender.

Research Goals, Hypotheses and Objectives

The broader impact of this work is to develop a nucleic acid detection diagnostic device for point-of-care applications by lowering barriers-to-entry for fabricating microfluidic devices. This work investigates two rapid prototyping methods–digital light processing (DLP) 3D printing and micromilling in cyclic-olefin copolymer (COC)–and introduces a pathway for scaling fabrication by hot embossing in COC. Ultimately, the goal is to enable future researchers to fabricate high resolution, biochemically compatible microfluidic devices using accessible and reproducible workflows.

Objective 1: Develop a comprehensive fabrication workflow for high-resolution 3D printed microfluidic devices. Using a commercially available 3D printer and resin, it is hypothesized that microfluidic devices can be fabricated that are capable of prototyping point-of-care diagnostics. To accomplish this, an accessible fabrication

workflow complete from design to bonding and chip-to-world integration is presented. Lastly, preliminary investigations into post-processing treatments are evaluated to reduce toxic chemicals and improve device performance in diagnostic assays.

Objective 2: Establish an accessible micromilling workflow in cyclic-olefin copolymer (COC) for integrated microfluidic device and assay development. With optimized milling parameters and substrate preparation, it is hypothesized that micromilling in COC can reliably produce reproducible, high-resolution microfluidic devices that are suitable for biochemical reactions such as recombinase polymerase amplification (RPA). To address this, a detailed end-to-end workflow for COC micromilling is developed, including tooling, feed rate, and spindle speed optimization. Then, future directions for RPA assay development are evaluated for compatibility and to support future scalable prototyping.

Objective 3: Develop a scalable hot embossing workflow for fabricating COC microfluidic devices that is accessible for academic labs. A previously reported PDMS-based master mold method is validated for its compatibility with COC embossing. Based on the challenges encountered, a new workflow is proposed utilizing a rigid epoxy-based master mold and a benchtop hot embosser to enable future fabrication of high-resolution COC devices for digital nucleic acid detection.

13

FABRICATION AND EVALUATION OF 3D PRINTED MICROFLUIDIC DEVICES FOR MOLECULAR DIAGNOSTICS

Introduction

Rapid prototyping of microfluidic devices offers significant advantages for microfluidics, especially in the development of point-of-care diagnostic tools. Among these methods, digital light processing (DLP) 3D printing has been widely adopted for microfluidics because it can produce the smoothest and highest resolution features.[14,15] Previous studies have shown the potential of 3D printed devices for cell-based assays or general fluid handling. However, the use of commercial DLP printers and resins for sensitive molecular diagnostics–such as recombinase polymerase amplification (RPA) or loop-mediated isothermal amplification (LAMP)–has been limited due to inhibition due to residual photoinitiators and uncured monomers in the material.[18,19] Studies have been performed to evaluate whether post-processing treatments, such as soaking in phosphate buffered saline (PBS), autoclaving, or extensive UV treatment, can reduce inhibition in 3D printed devices.[17,32] These studies demonstrate that these treatments are sufficient for cell culture applications, however information on downstream compatibility with sensitive diagnostic reactions is limited.

Beyond biochemical compatibility, fabricating functional microfluidic devices for molecular diagnostics presents several technical challenges, particularly in producing complex microstructures smaller than 200 μm. While larger structures may suffice for general microfluidics or cell-based assays, sub-100 μm features are often required for some bioanalytical assays.[32] In DLP-based 3D printing, resolution is fundamentally constrained by the projector's pixel size, which determines the smallest discrete unit of light exposure. Most commercially available systems have pixel sizes near 30 μm, which sets a theoretical minimum feature size on that scale.[16] However, practical limitations arise due to resin viscosity, incomplete polymerization, and resin entrapment, especially in narrow or curved

architectures.

The CADworks3D clear microfluidic resin V0.7a (also marketed as MiiCraft Bv007a) was developed specifically for microfluidics and exhibits a low viscosity (75-100 mPa*s at room temperature).[33] This resin's viscosity is more than ten times lower than other popular resins like FormLabs BioMed (1350 mPa*s) or FormLabs Clear (850–900 mPa*s).[33] Achieving consistent, high-quality complex microstructures requires not only careful print parameter selection but also a design-driven approach tailored to the mechanical and optical characteristics of the printing system. Previous work using the Bv007a resin has generally been limited to producing simple, straight microchannels at widths of 200 μm or larger.[32,33] Microfluidic devices for molecular diagnostics often feature more geometrically complex structures–such as curved paths, intersecting channels, or 3D elements–which can further amplify common print defects such as resin entrapment, stair-stepping artifacts, and light scattering.[34,35]

This work presents a fabrication workflow and design considerations that enable printing of sub-100 μm, complex microchannels using a commercially available DLP 3D printer (MiiCraft 50) and resin (CADworks3D clear microfluidic resin V0.7a, also referred to as MiiCraft Bv007a). Then, several bonding strategies were evaluated to determine their efficacy in producing sealed devices suitable for molecular diagnostics. In addition, a bespoke chip-to-world interface was developed to address common operational issues in fluid loading and thermal control. Finally, preliminary experiments were performed to assess whether post-processing treatments can reduce biochemical inhibition by pre-leaching residual photoinitiators and uncured monomers from the printed devices. These results lay the groundwork for future development of point-of-care diagnostic devices based on 3D printed microfluidics.

Materials and Methods

Microfluidic Device Fabrication

Microfluidic devices were fabricated using a MiiCraft 50 DLP 3D printer and the CADworks3D clear microfluidic resin V0.7a, a low viscosity, optically transparent resin specifically formulated for microfluidics. Designs were generated in AutoCAD and exported into the MiiUtility slicing and printing software. Full print parameters are summarized in Table 1. Devices were printed both directly on the build plate and on a silianized glass substrate. Once removed from the build plate, the print was placed in a 90% isopropanol bath and ultrasonicated for 30 seconds. The print was then scraped off of the glass using a razor blade (if applicable), rinsed with 90% isopropanol, and dried with compressed air. The printed device was then bonded using methods described below. Finally, a 20 second UV cure was performed in a UV light box (B9Creations, B9 Model Cure).

Printing on Glass To maximize print quality and minimize feature occlusion, most all devices were printed on silanized glass slides using a modified protocol previously presented by Neubauer et al. [36]. Glass slides (Globe Scientific #1321) were first plasma treated for one minute with room air using the Harrick Plasma Cleaner (Harrick Plasma, Model: PDC-32G), then submerged in a freshly prepared 2.0% (%vol/%vol) solution of 3-(trimethoxysilyl)propyl methacrylate (Sigma-Aldrich, M6514) in ethanol for five minutes. Slides were then submerged in 200-proof ethanol for five minutes. Residual ethanol was evaporated off the slides in a 105 °C oven for five minutes before being stored for up to 24 hours at 4 °C until use. A schematic of the silanization workflow is shown in Figure 8.

Glass slides were affixed to the center of the aluminum build plate using double-sided polyimide tape (kaptontape.com, PPTDE-3/4). Devices were printed with a single base layer at three seconds exposure to minimize over-curing and the print offset height was set

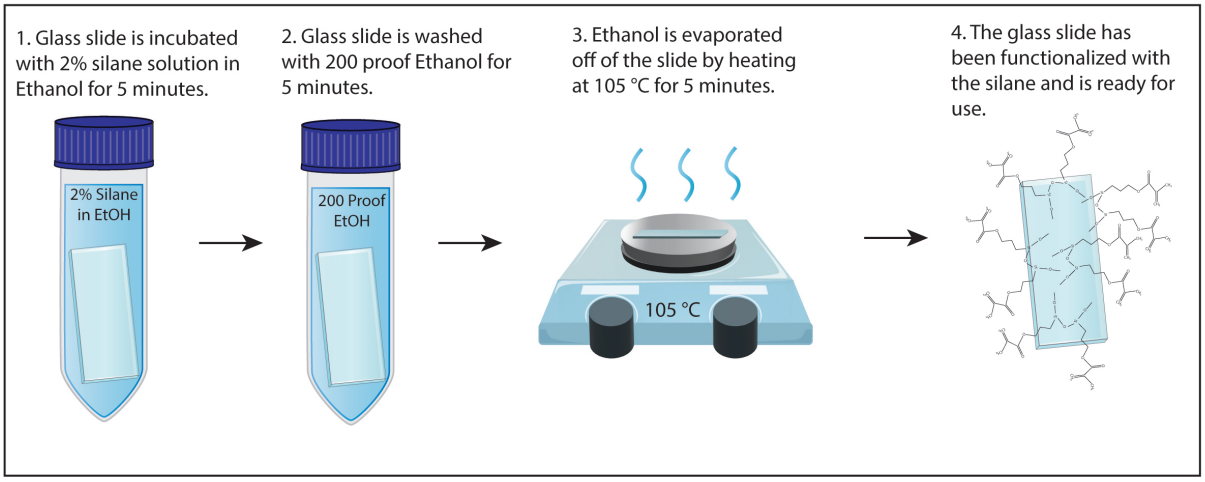


Figure 8: Schematic of the glass silanization protocol to prepare glass slide to be used as the substrate for printing on glass. Glass slides are functionalized with 3-(trimethoxysilyl)propyl methacrylate, which provides a covalent connection between the glass and the 3D printed device.[36]

to 1.1 mm to accommodate the slide and tape thickness.

Bonding Strategy Evaluation

Three primary strategies were evaluated for bonding open channel 3D printed microfluidic devices: (1) spin-coating resin onto a glass cover slip (VWR, 48366067) for direct and (2) indirect bonding to a clean glass cover slip, and (3) using double-sided pressure sensitive adhesive (Adhesives Research, ARCare 90445Q) with a glass slide (Globe Scientific #1321 or poly(methyl methacrylate) (PMMA) substrate (McMaster-Carr, item #8560K178).

Bonding to spin-coated glass cover slip This method was introduced by Kecili and Tekin [37] and is summarized in Figure 9. First, a bespoke spin coater chuck was 3D printed from eSUN eRESIN-PLA Pro resin using the EPAX X1 4k 3D printer. This ensured a quality seal was obtained between the cover slip and the vacuum chuck on the spin coater. Then, a glass cover slip was silanized using the same protocol discussed previously Figure 8. Next, the slide was placed on the spin coater chuck and 0.2 mL of CADworks3D clear microfluidic

Table 1: Recommended printing parameters for silanized glass substrates (10 μm slice thickness) using the MiiCraft 50 DLP 3D printer and Bv007a resin.

Printing Parameter	**Value**	**Description**
Curing Time	0.70 s	Amount of UV exposure per layer.
Speed	Slow	Peeling speed between layers. Slower speed allows more time for resin to evacuate.
Gap Adjustment	0.10 mm	Thickness of the first printed layer above the glass slide.
Base Layers	1	Number of overcured base layers to improve adhesion to the glass.
Base Layer Curing Time	3 s	Curing time for base layer exposure. Shorter time reduces overcuring artifacts on the glass.
Buffer Layer	1	Transitional layer between base layer and normal exposure, helps minimize delamination.
Power	75%	Percentage of UV light source output during exposure.
Antialiasing	Max	Surface smoothing from the z-axis to reduce stair-stepping artifacts.
Sharpness	0	Sharpness control for digital projection edges. 0 minimizes overexposure of fine features.
Resin Shrinkage Compensation	X: 0%, Y: 0%	Adjusts for dimensional changes caused by resin shrinkage during curing.

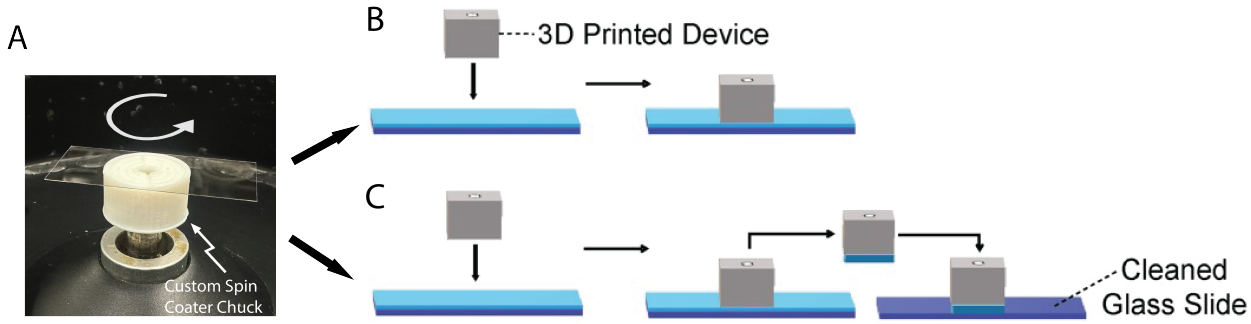


Figure 9: Schematic of the two bonding strategies evaluated for bonding 3D printed devices to glass cover slips using resin as an adhesive layer. (A) A glass cover slip is spin coated with resin following the protocol in Table 4. (B) Direct Bonding: The 3D printed device is adhered directly to the spin coated slide. Then, UV light is used to polymerize the uncured resin to adhere them together. (C) Indirect Bonding: The spin coated glass slide is used to stamp the resin onto the 3D printed device, which is then adhered to another clean glass slide. Then, UV light is used to polymerize them together. This figure is reproduced from Kecili and Tekin [37], who this method is adapted from.

resin V0.7a was dispensed in the middle of it using a micropipette. Then, a three step spin coating process is performed: 500 rpm for 30 seconds with a 10 second ramp time and 4000 rpm for 30 seconds with a 5 second ramp time. Then, a clean 3D printed device, without the additional UV cure, was aligned and pressed onto the glass cover slip. Both indirect bonding by first stamping the device with resin and directly bonding to the spin coated glass were evaluated. A handheld UV flashlight (uvBeast, uvBeast V1) was used to polymerize the resin for at least 2 minutes while holding constant manual pressure.

Bonding to substrate using double-sided adhesive This method is summarized in Figure 10 and is used for adhering to both glass slides and PMMA substrates. Initially, PMMA substrates were cut to 22 x 30 mm using a BOSS LS-3655 150W CO_2 laser cutter. First, the substrate (glass slide or PMMA) is cleaned using 90% isopropanol and dried with compressed air. Then, a double-sided pressure sensitive adhesive tape (Adhesives Research, ARCare 90445Q) is gently rolled onto the substrate with care to minimize bubbles between the tape and the substrate. Next, the clean 3D printed microfluidic device is manually pressed

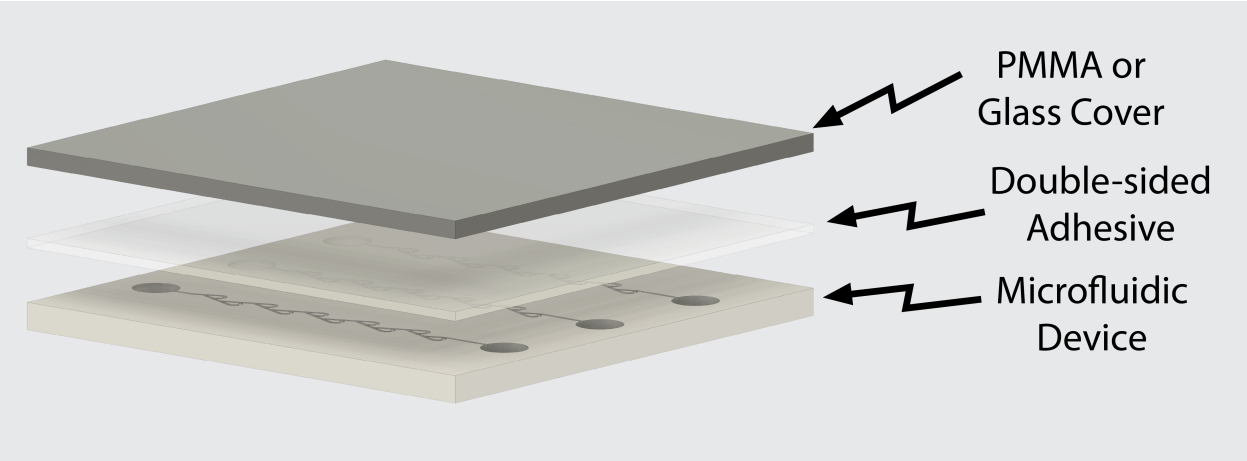


Figure 10: Schematic of the pressure sensitive adhesive bonding strategy. A glass slide or PMMA substrate is first laminated with a double-sided pressure sensitive adhesive (ARcare 90445Q). Then, the microfluidic device is pressed into the adhesive and air bubbles are rolled away using a plastic seam roller.

onto the open adhesive and a plastic seam roller (McMaster-Carr, item #:62395T12) is used to ensure homogeneous contact between the 3D print and the adhesive. Finally, the bonded chip is returned to the UV box for an additional 20 second final cure.

Fabrication of custom chip-to-world apparatus

To address difficulties with reliably filling 3D printed microfluidic devices, a bespoke chip-to-world apparatus was 3D printed from eSUN eRESIN PLA Pro resin using the EPAX X1 4K 3D printer. A schematic of the apparatus is shown in Figure 11. Square nuts (McMaster-Carr, 97259A111) are press fit into place and thumb screws (McMaster-Carr, 96016A552) are used to hold the two pieces of the clamp together. Lastly, rubber o-rings (McMaster-Carr, 9452K11) are recessed into the clamp to provide a gasket between the device and the apparatus when filling with reagents. In addition to the filling apparatus, a custom heating apparatus was also fabricated. The heating apparatus features a recess to maintain thermal contact between the temperature controller/heater and the 3D printed device. It also uses the same press fit square nuts and thumb screws to clamp the device in

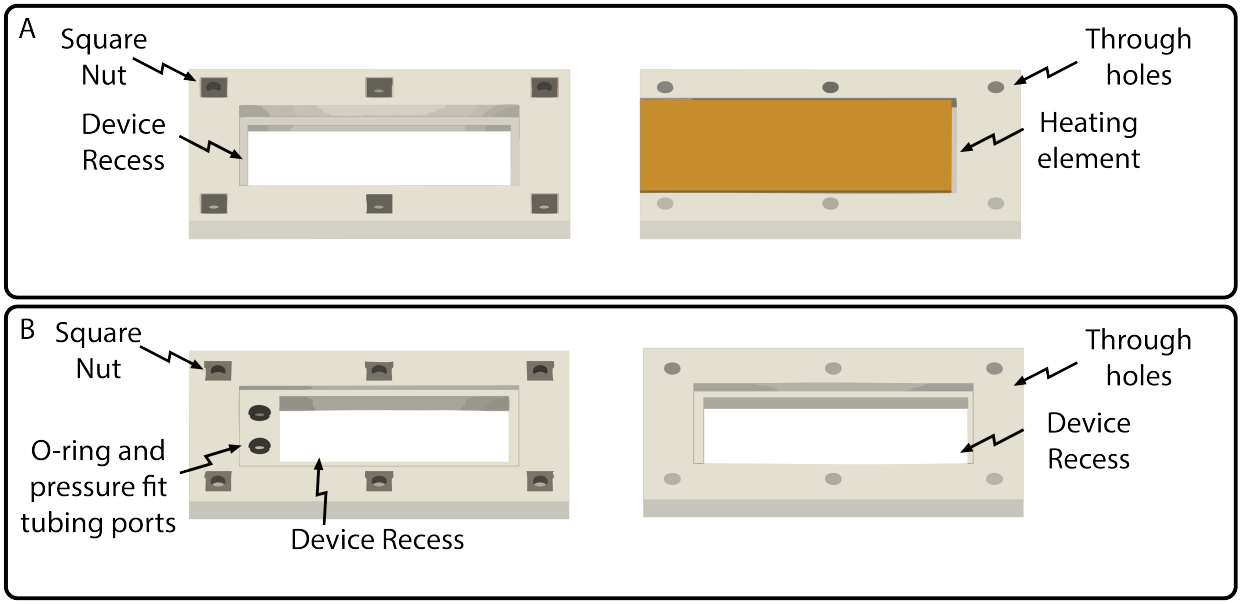


Figure 11: Schematic of the prototype chip-to-world apparatus. For both apparatuses shown, thumb screws (not shown) are used to clamp the device together. (A) Heating apparatus used to clamp device in direct thermal contact with heating element. (B) Clamp for filling device. O-rings press into inlets on the devices, then tubing can be pressure fit into the inlet ports on the back side (not shown) of the filling clamp.

place.

Thermal Stability Assessments

To evaluate the thermal stability of the 3D printed devices, an empty device was heated to reaction conditions for PCR and LAMP. A thermal heater previously developed by Cruz et al. [38]. First, the device and heater were fastened into the heating chip-to-world apparatus (Figure 19). Then, two experiments were performed: constant temperature at 55 °C for one hour, and PCR thermal cycling (40 PCR cycles of 30 seconds at 95 °C, 30 seconds at 55°C, and 45 seconds at 68 °C). Images were taken before and after each treatment.

Additional post-processing

To evaluate whether residual photoinitiators and uncured monomers can be measured in liquid leachate from 3D printed devices, a preliminary leaching experiment was performed.

First, 10 x 10 x 50 mm columns were 3D printed using the MiiCraft 50 DLP 3D printer and the MiiCraft Bv007a resin. Three samples were soaked in PBS (Sigma-Aldrich, P3813) for 4 hours at 37 °C, and another three samples were soaked in 200 proof ethanol for ten minutes, then soaked in PBS for 4 hours at 37 °C. Samples were taken every hour with liquid replacement, then UV/vis spectra were obtained using the Nanodrop 2000 and a quartz cuvette.

Results and Discussion

Dimensional Fidelity of 3D Printed Devices

Microfluidic devices were fabricated by DLP 3D printing using a commercially available 3D printer (MiiCraft 50) and resin (CADworks3D clear microfluidic resin V0.7a). Although curved channels less than 100 μm in diameter were achieved, the measured dimensions varied significantly from the nominal width (Figure 12). The dimensional fidelity, the degree to which fabricated features match the original design, was found to be quite poor for channel width. As shown in Figure 12, there is a significant discrepancy between the designed dimensions and the actual channel geometry. 3D printed tesla valves designed to have a widths of 60 μm, 100 μm, and 200 μm actually measured 103.5 $\pm$ 6.1 μm, 160.6 $\pm$ 18.2 μm, and 196.7 $\pm$ 6.1 μm, respectively. This may be due to the anti-aliasing setting which adds grayscale pixels to curved edges to generate smoother curved features. Additionally, these effects may be more drastic due to printing defects due to poor resin adhesion. Future experimentation may explore this by evaluating whether increasing the size of island-like features can protect from these defects.

Integrity of 3D Printed Microchannels

The MiiCraft 50 3D printer utilizes the constrained surface technique, commonly referred to as the “bat” configuration, which is characterized by the upside-down orientation

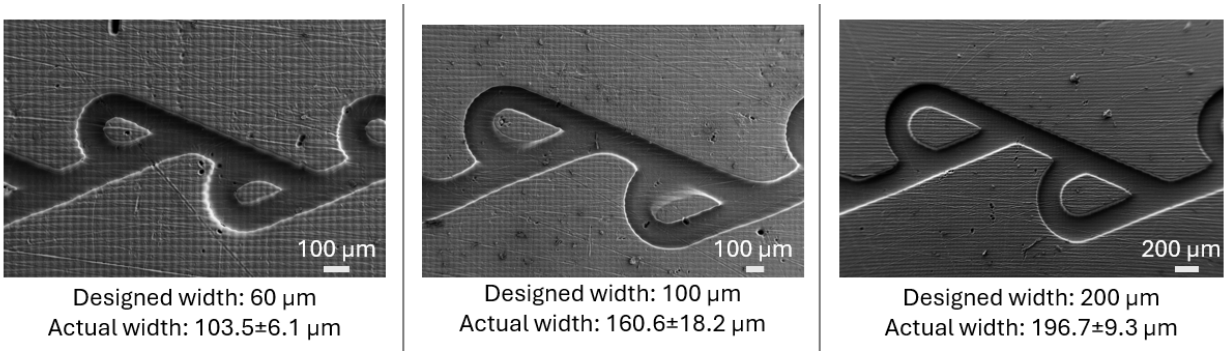


Figure 12: Field-emission scanning electron microscope (FE-SEM) images of 3D printed microfluidic channels. The CAD designed width is compared to the measured width and the measured with is much larger than the designed width.

that the print is polymerized–similar to how a bat sits on the top of a cave.[13] In the bat configuration, the build plate is dipped into the vat of resin, a layer is polymerized, then the build plate lift and peels off of the bottom of the vat and returns back to the vat to repeat the process for each layer (Figure 13).

With this style printer, the build plate lifts up while the vat simultaneously tilts to peel each layer off of the transparent bottom of the vat. It is proposed that these mechanisms may lead to several types of print defects due to the pressure required to break the surface tension between the resin vat and the print. When the build plate lifts up, a "cupping" effect from the pressure differential is formed from the release of the vacuum between the printed device and the bottom of the vat.[33] As a result, resin in some features can be physically torn during separation. This effect can be visualized in Figure 14.

One of the largest limitations of resin 3D printing is resin evacuation. Resin is typically a very viscous liquid, which can lead to excess resin occluding features. In this case, unpolymerized resin is adhered between layers, which results in a weak area of the print. Then, during print removal from the build plate, the print will break off from those weak points. Additionally, asymmetric shear stress from the pressure differential caused by the tilt mechanism is associated with consistent defects around square features. As shown in

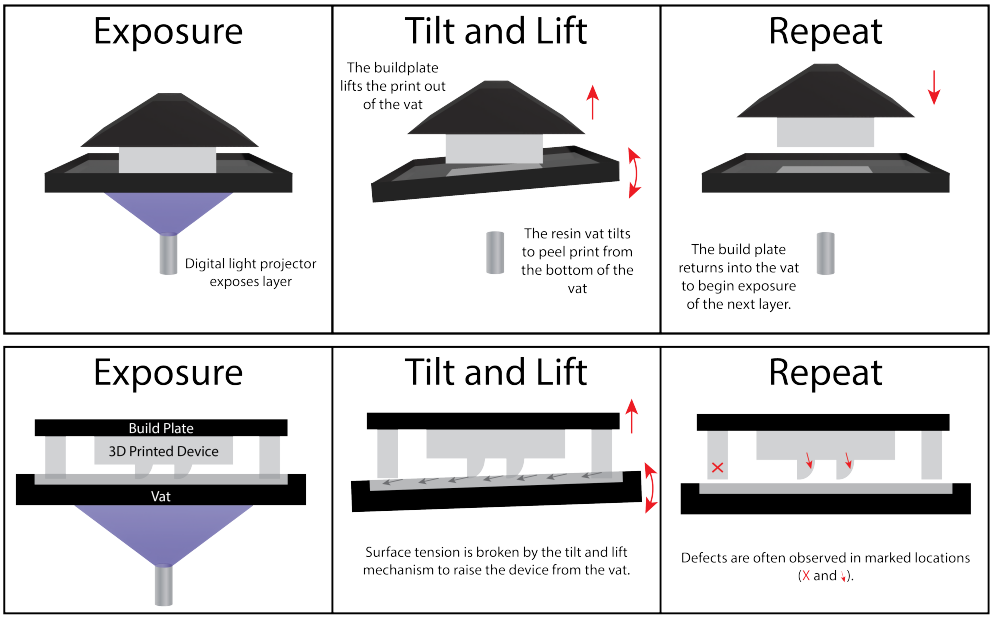


Figure 13: Schematic of tilt mechanism used in MiiCraft 50 DLP 3D Printer. To break the surface tension between the 3D print and the resin vat, the vat tilts while the build plate lifts up and out of the vat. This mechanism may lead to defects that can be observed in Figure 14.

Figure 14, initial layers of the features appear to be wicked away resulting in a filleting effect on the corners of square features. After trial-and-error, it was found that the best way to increase device-to-device reproducibility was to simply filet square features in CAD. For islands, or other designs which struggle with similar defects, increasing the surface area of those features was the most successful.

Additionally, a common print defect on inlets placed on the side of the print that is lifted out of the vat was associated with the tilt mechanism (Figure 14). In this case, it appears that resin is wicking away to release the internal pressure from those larger features. As a result, consistent defects which appear to be air pockets streaming from the inlets are observed. After experimentation, it was found that simple adjustments to the design of the device are protective against some of these defects. For example, defects can be minimized if the inlets are made smaller, or if an air relief is made in larger features. However, the best

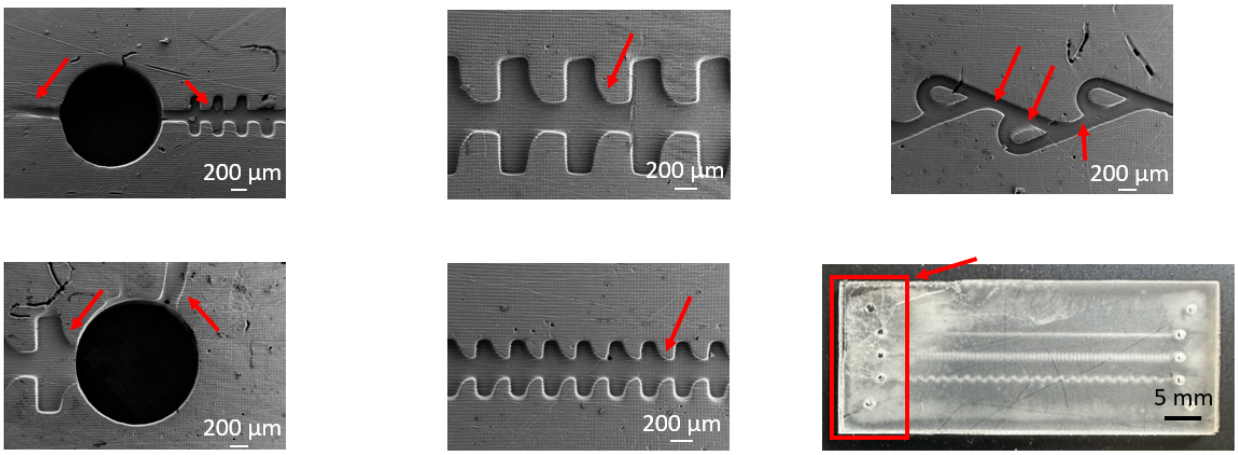


Figure 14: Field-emission scanning electron microscope (FE-SEM) images of defects that are common due to the tilt and lift mechanism of bat-style digital light projection (DLP) 3D printers. On the left small islands polymerized poorly and were physically torn during separation from the bottom of the vat. On the right straight channels failed to polymerize fully and the asymmetric shear stress caused by separation of the device from the vat produces asymmetric features.

practice that was found was to place the inlets on the same side of the device, and orient the print so that the side with the inlets is tilted off of the bottom of the vat first. Most likely, this ensures that the surface tension inside them is broken early which provides extra time for the resin to evacuate from the inlets.

Bonding Evaluation

Bonding the devices serves two essential functions: (1) sealing open-faced microfluidic channels and (2) reducing surface roughness to enable optical clarity and improve bond quality. Both the top and bottom surfaces of 3D printed devices often exhibit imperfections due to printing artifacts or resin contamination (Figure 15). On the patterned side, these artifacts may result from scratches on the transparent vat bottom, resin debris, or local defects in the print. A suitable bonding method must therefore both seal the channel and conform to surface irregularities to ensure a strong bond and a smooth surface for imaging.

To address this, three bonding strategies were investigated: (1) direct bonding to a

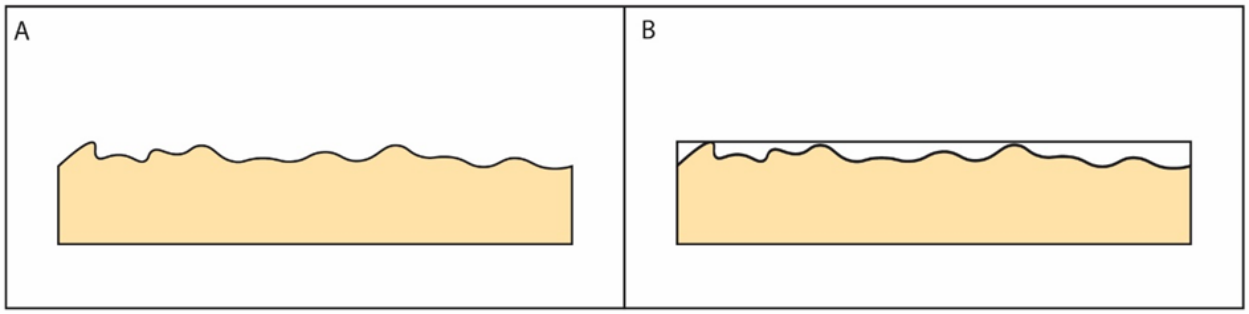


Figure 15: (A) Illustration of the rough surface of the microfluidic prints prior to bonding. (B) Once adhesive is applied to the rough surface, it flattens out the surface of the print which makes it optically transparent.

resin-coated glass cover slip, (2) indirect bonding via stamping onto a spin-coated resin layer, and (3) using double-sided pressure-sensitive adhesive (PSA) laminated to either glass or PMMA substrates.

Bonding to a resin-coated cover slip provides an advantage by limiting the working fluid's exposure to only polymerized resin and glass, reducing the variety of material interfaces. However, replicating this method was challenging due to the fragility of the glass slide and the bowed 3D printed device (Figure 9). The bowing arises from the strain forces from the resin shrinkage after polymerization, and for successful bonding, the substrate must either conform to this shape or flatten the print during bonding. Attempts at both stamping and direct bonding revealed that cover slips were too fragile to confirm to its shape and the spin coated resin was too weak to impose sufficient force to flatten the print. Additionally, achieving a homogeneous resin coating via spin coating was inconsistent. Even when a uniform layer was achieved, misalignment during handling often led to channel occlusion before UV curing. Furthermore, once polymerized, the resin sometimes failed to establish a complete and permanent seal with the printed surface, resulting in poor adhesion and uneven bonding.

In contrast, bonding with double-sided PSA provided a more reliable and straightforward alternative. The adhesive was first laminated onto a flat substrate, then the 3D printed

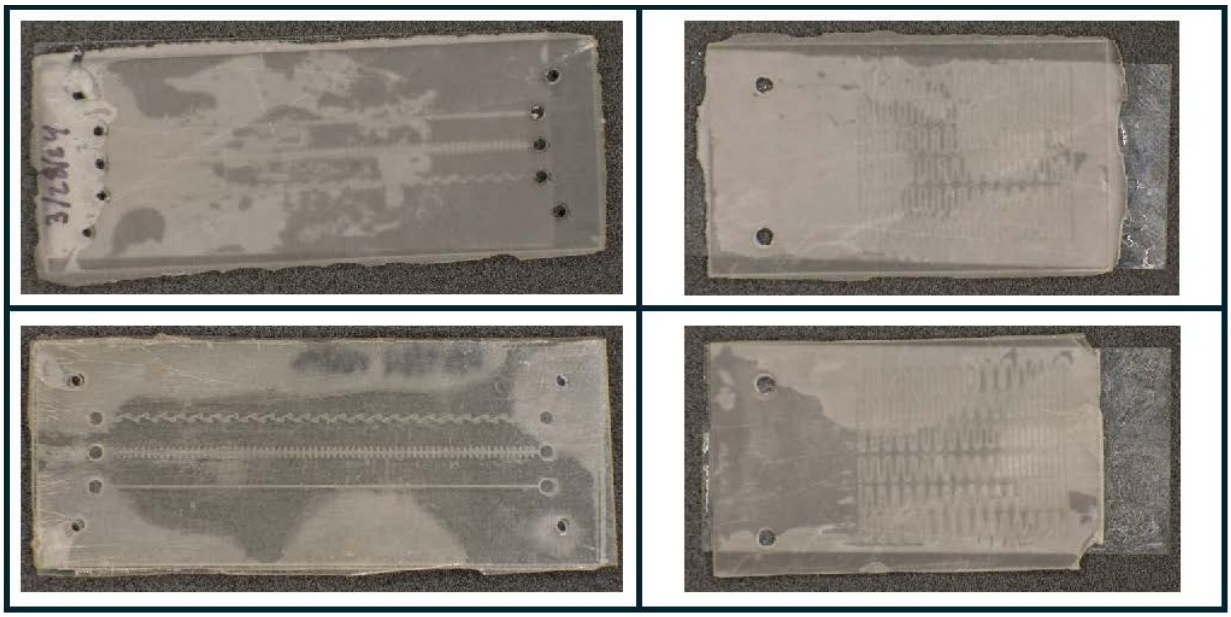


Figure 16: Images of the failures for bonding devices to a spin coated glass slide. Devices were bonded to spin-coated glass, via both the stamping and direct bonding methods (Figure 9). However, there was poor bond strength due to a non-homogeneous bonding surface and microchannel occlusion

device was pressed directly onto it (Figure 17). Two substrates were compared–glass and PMMA–with PMMA performing better due to its slight flexibility, which allowed it to better conform to the bowed surface of the print. In contrast, devices bonded to glass were more brittle and prone to failure. Among the three methods tested, bonding to PMMA using ARCare 90445Q double-sided PSA produced the most reproducible and high-quality results. Further, the use of ARCare 90445Q with Bv007a resin has been validated in previous studies for several biological applications.[39,40] This adhesive features a homogeneous adhesive layer, high optical transparency in the visible light spectrum, and has been shown to work with the bioanalytical assay, loop-mediated isothermal amplification (LAMP).[39,40] Given its ease of use, reproducibility, and performance in prior bioanalytical workflows, this bonding method was selected for continues development and downstream testing.

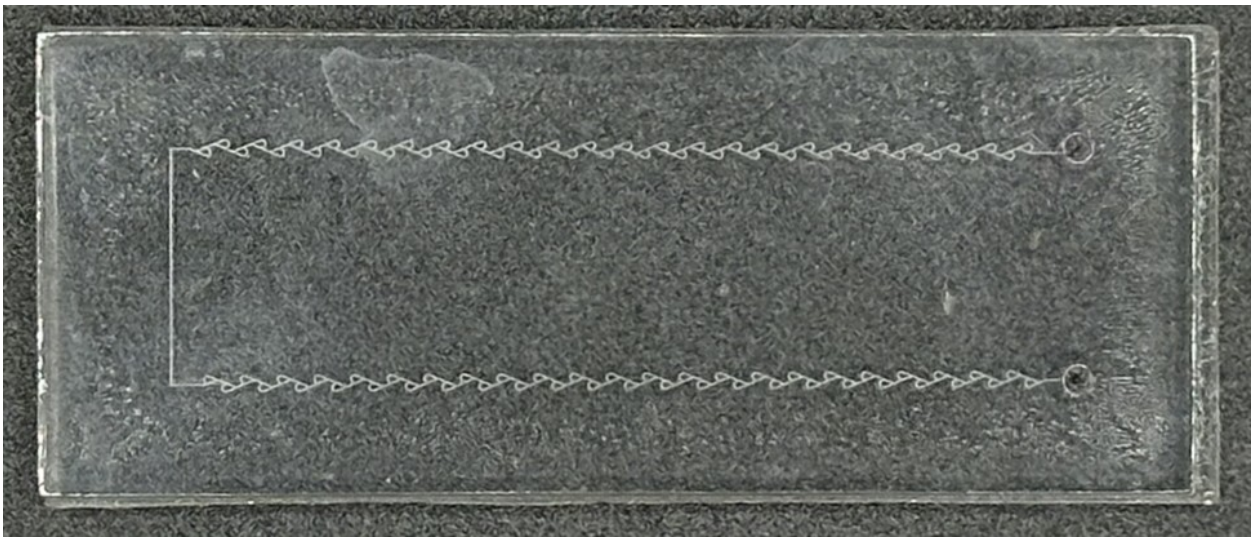


Figure 17: Image of 3D printed device bonded to PMMA using doulbe-sided pressure sensitive adhesive (Adhesives Research, ARcare 90445Q).

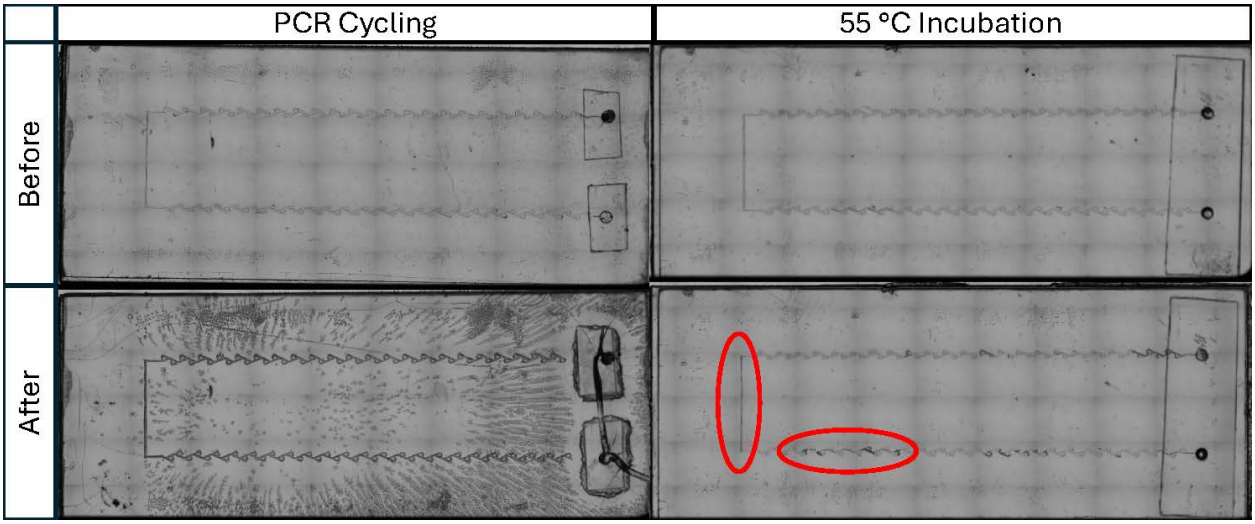


Figure 18: Images of 3D printed microfluidic devices filled with water before and after two heating treatments: (Left) 40 PCR cycles (30 seconds at 95 °C, 30 seconds at 55°C, and 45 seconds at 68 °C). (Right) 55 °C for 60 minutes. Both devices were unable to withstand the temperatures without cracking. The 55 °C treatment showed smaller cracking within the channels (circled in red), whereas the PCR treatment showed very large cracking from the inlets, within the channels, and delamination of the adhesive between the PMMA and the device.

Thermal Stability of 3D Printed Devices

The thermal stability of a 3D printed device was evaluated both empty and filled to determine its suitability for elevated-temperatures required in bioanalytical applications. When heated while filled, internal pressure can exacerbate mechanical stress, leading to adhesive failure or device fracture. To assess the thermal tolerance, bonded devices were subjected to two treatments: (1) 55 °C for one hour, and (2) 40 PCR cycles (30 seconds at 95 °C, 30 seconds at 55°C, and 45 seconds at 68 °C).

It has previously been demonstrated that this resin is stable at 37 °C without any noticeable evaporation or cracking.[33,41] Similarly, in this study fractures began to appear at 55 °C, leading to sample evaporation. Despite this, an additional device was subjected to thermal cycling, which resulted in far worse structural damage as very large fractures formed and delamination of the adhesive. Unfortunately, these results indicate that the devices bonded to PMMA with double-sided PSA are unable to withstand sustained conditions above 37 °C.

To isolate the influence of internal pressure, an additional experiment evaluated unfilled devices under the same temperature conditions. Unfortunately, cracking was still observed at 55 °C after one hour, suggesting that the resin itself–not just internal channel pressure–is a limiting factor. These results reinforce the conclusion that Bv007a resin becomes mechanically unstable above 37 °C. Therefore, the use of this material is not recommended for applications involving temperatures exceeding 37 °C.

Custom chip-to-world interface

A custom chip-to-world interface was prototyped using LCD vat polymerization 3D printing. The system included two distinct clamps: a filling clamp and a heating clamp. The filling clamp served as an interface for introducing fluids into the microfluidic devices. To attach tubing to the 3D print, the tubing was simply pressure fit into the ports. However, this

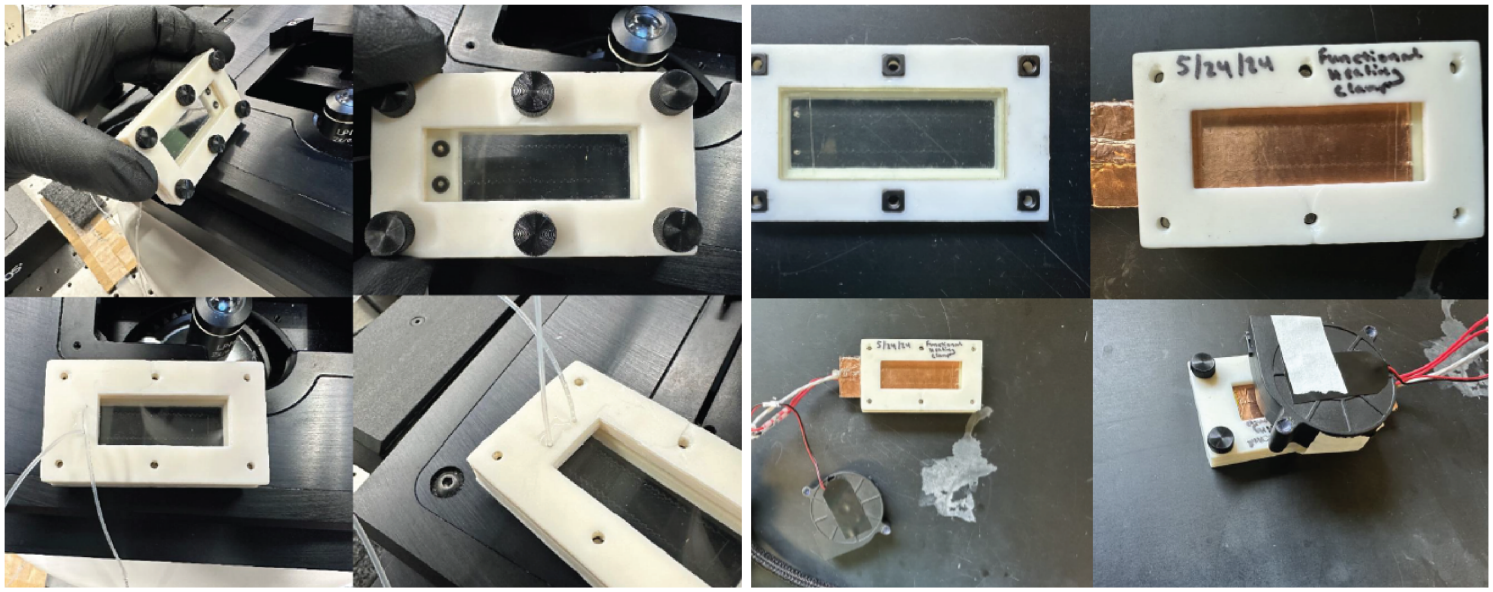


Figure 19: Images of functional clamp for filling (left) and heating (right) microfluidic devices fabricated using the EPAX 3D X1 4k 3D printer using eSUN PLA Pro resin. A detailed schematic is shown in Figure 11. The microfluidic device is clamped down so that rubber o-rings press against the inlet holes. Then, tubing is pressure fit into the ports to fill the devices. However, some leaking is observed when filling the devices between the port holes and the tubing. Thus, future development is necessary to avoid leaking.

approach led to some leakage around the tubing interface (Figure 19). Although the devices could still be filled, the leakage introduced concerns about sample loss and reproducibility.

For preliminary testing and evaluation of the 3D prints, the heating clamp was adequate. However, it lacked the mechanical rigidity required to maintain uniform pressure over extended periods of time. After several uses, delamination was observed along the clamp walls, and the embedded square nuts began to loosen.

Despite these limitations, the prototypes were valuable for identifying key design constraints and failure points prior to committing resources to more advanced fabrication techniques. In the following chapter, these insights are used to guide refinements to produce a final, improved chip-to-world interface.

Additional Post Processing

Residual uncured monomers and photoinitiators present in 3D printed devices are known to negatively impact cytocompatibility and enzyme function.[18,19,33] The CAD-works3D clear microfluidic resin V0.7a (also sold as MiiCraft Bv007a resin) contains a higher concentration of additives than other resins commonly used in microfluidics, most likely to reduce the viscosity of the resin.[33] Consequently, it is considered incompatible with biological experiments. Regardless, several groups have attempted to manipulate the 3D printed devices to make them cytocompatible–even if only for a few minutes.[42] However, further investigation is required to evaluate whether post-processing can create devices that are compatible with sensitive bioanalytical applications. To investigate whether toxic leachables could be removed through pre-treatment, two post-processing methods were evaluated: (1) a PBS soak for three hours at room temperature, and (2) a 10-minute soak in 200-proof ethanol followed by a PBS soak for three hours at room temperature. It was hypothesized that the ethanol would swell the 3D print's polymer matrix, thereby enhancing diffusion of residual monomers and other leachables. These treatments were limited to three

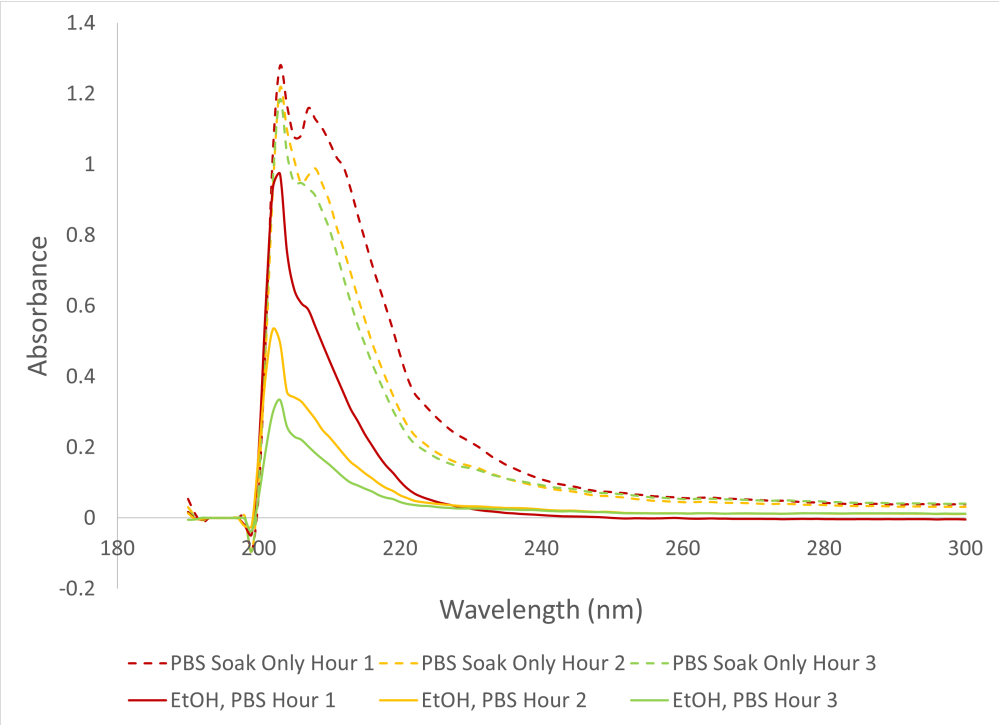


Figure 20: UV/vis spectra of leachate from 3D printed devices. Two treatments are shown:a PBS soak for 3 hours at room temperature, and an initial soak in 200 proof ethanol for 10 minutes followed by a PBS soak for 3 hours at room temperature. Samples were taken every hour for three hours and fluid replacement was performed after each sample.

hours because previous work with the MiiCraft Bv007a resin has shown that prolonged liquid exposure can cause the resin to degrade.[33]

Absorbance spectra of the leached compounds showed peaks between 200 and 280 nm (Figure 20). During the three hour leaching treatment, Samples were collected hourly, with complete fluid replacement after each time point. It was anticipated that absorbance would decline over time and approach baseline by the third hour. However, significant detectable absorbance persisted after three hours, indicating that substantial amounts of leachable compounds remained even after four hours.

The ethanol pre-treated group exhibited markedly lower absorbance at each timepoint relative to the PBS-only control. This suggests that the ethanol soak either facilitated initial bulk removal of leachables or altered the diffusion efficiency during subsequent PBS

treatment. Although spectra were analyzed for the ethanol soak solution, contamination from permanent marker ink on the sample interfered with interpretation, and no conclusions could be drawn from that data.

Overall, the data suggests that ethanol pre-treatment may enhance the removal of toxic leachables from Bv007a 3D prints. However, substantial residual leaching persists after three hours, indicating that longer treatment times may be necessary. However, excessive leaching could lead to removal of the resin's additives which may have an effect on the structural integrity of the 3D printed devices.[33] Future studies should combine quantitative leaching analysis with functional testing of enzyme/reaction inhibition to determine the optimal post-processing protocols.

Conclusions and Future Work

Digital light projection (DLP) 3D printing has become a widespread phenomenon for rapid prototyping in microfluidics. However, obtaining features smaller than 200 μm is extremely difficult using commercially available printers and resins. While many applications do not require features on that scale, many bioanalytical applications require extremely low sample volume that generally has to be obtained from other manufacturing methods. In this work, it is demonstrated that a commercially available DLP 3D printer (MiiCraft 50) and resin (CADworks3D clear microfluidic resin V0.7a) can reliably produce functional microfluidic devices with curved channel features less than 100 μm. Although extensive parameter optimization was not performed, successful fabrication required design iterations to avoid defects that are made worse by minimizing feature resolution. Modifications included inlet placement, designing pressure reliefs for larger open areas and printing on silanized glass. As a result, high resolution microchannels were obtained while minimizing print defects. Next, several established bonding techniques were evaluated for their long term stability, ease-of-manufacturing and reproducibility. Of the methods evaluated, double-

sided PSA bound to PMMA produced the most consistent results while maintaining optical transparency and biochemical inertness. Then, thermal testing of the 3D printed devices revealed that the resin is unstable above 37 °C, where sustained exposure leads to internal cracking of the device allowing evaporation of the channel contents. For sensitive bioanalytical applications, maintaining a closed system is essential, therefore this resin may not be useful for applications such as polymerase chain reaction (PCR) or loop-mediated isothermal amplification (LAMP), but may be applicable for isothermal reactions performed at lower temperatures, like recombinase polymerase amplification (RPA). To address the major difficulty of interfacing microfluidics with the world, custom clamps were developed for both filling devices and for maintaining thermal contact during heating and imaging. These prototypes laid the groundwork for the development of a refined product whose utility will be demonstrated in the next chapter. A large drawback of 3D printed microfluidics is inhibition and poor compatibility with polymerase enzymes which are critical to many bioanalytical reactions, like RPA. Further, the CADworks3D clear microfluidic resin V0.7a is not considered a biocompatible resin, but others have demonstrated the ability to leach out many toxic chemicals that can inhibit these reactions, like residual photoinitiators or uncured monomers.[17] This work inspired an exploration into pre-leaching the printed devices to minimize inhibition from the toxic chemicals present in the material. Early observations suggest that post-processing protocols, such as ethanol and PBS soaks–may help pre-leach the inhibitory chemicals and improve compatibility for sensitive biochemical reactions. Future work will aim to evaluate whether a sensitive bioanalytical assay can be developed in a microfluidic device made from CADworks3D clear microfluidic resin V0.7a by removing residual photoinitiators and uncured monomers from the chips.

A LOW-COST WORKFLOW FOR MICROMILLING CYCLIC-OLEFIN COPOLYMER DEVICES FOR NUCLEIC ACID DETECTION

Contribution of Authors and Co-Authors

Manuscript in Chapter 3

Author: Camden Long

Contributions: Technology development, Investigation, Microfabrication, Conceptualization, Methodology, Formal analysis, Data curation, Manuscript writing and editing.

Co-Author: Matthew Culp

Contributions: Microfabrication, Critical analysis, Data curation, Manuscript writing and editing

Co-Author: Stephan Warnat

Contributions: Investigation, Conceptualization

Co-Author: Stephanie McCalla

Contributions: Investigation, Conceptualization, Critical analysis, Manuscript editing

Manuscript Information

Camden Long, Matthew Culp, Stephan Warnat, Stephanie McCalla

Microfluidics and Nanofluidics

Status of Manuscript:
_X_ Prepared for submission to a peer-reviewed journal
____ Officially submitted to a peer-reviewed journal
____ Accepted by a peer-reviewed journal
____ Published in a peer-reviewed journal

Springer

Introduction

Rapid prototyping enables researchers to design and test microfluidics within the same day, which accelerates assay development and design iteration. Over the past decade, many benchtop fabrication methods have emerged that, in many cases, can replace traditional cleanroom-based fabrication. Among these, 3D printing has become especially popular for its accessibility, low cost and ability to produce high resolution microstructures. However, 3D printing is not ideal for many biological and bioanalytical applications. This is mainly due to the leaching of residual photoinitiators or uncured monomers into the working fluid.[18] These compounds have been shown to inhibit PCR amplification, rendering 3D printed devices often incompatible other biochemical reactions as well.[19] Even recent biocompatible or medical-grade resins may still leach enough contaminants to interfere with sensitive applications.[17] Further, 3D printed devices are less common in commercial applications due to the poor material properties of the resin and its inherently low-throughput production. This disconnect introduces additional variability which ultimately slows development. In contrast, prototyping directly in the end-use material allows for concurrent development of both the device and the biochemical assay, ultimately streamlining iteration.

Industry manufacturers of biomedical microfluidic devices fabricate in thermoplastics: cyclic-olefin copolymer/polymer (COC/COP), poly(methyl methacrylate) (PMMA) and polycarbonate (PC).[21,22] Thermoplastics have been widely adopted in industry for scalability through high-throughput manufacturing and they have a low cost-per-unit at scale[23]. Thus, enabling rapid prototyping in the final device material bridges a critical gap between early-stage research and technology translation.

Cyclic-Olefin Copolymer (COC) offers significant advantages for microfluidics due to its chemical inertness, biological compatibility, optical clarity, and high thermal stability.[24] These properties make COC and excellent material choice for many microfluidic applications.

However, traditional fabrication methods for COC, such as hot embossing and injection molding, require costly equipment and are time consuming, limiting accessibility for many labs and prototyping environments.[24]

For rapid prototyping in COC, direct structuring methods like laser ablation, xurography and micromilling allow single device fabrication with greater fabrication flexibility compared to traditional thermoplastic fabrication methods. Among these, micromilling is particularly promising, as it can produce a prototype in minutes and the microstructures are similar to those produced by hot embossing. Micromilling is a subtractive process that uses miniature cutting tools to create micro-scale features on a workpiece (Figure 21). A rotating tool cuts material as it moves along a specified toolpath to produce the desired shape. Further, previous work has demonstrated that micromilling can produce feature sizes as small as 30 microns, comparable to the precision of indirect methods like hot embossing and injection molding.[28] Unfortunately, many presented methods for micromilling require specialty micro-CNCs and expensive end mills.[29–31,43] Additionally, due to the high variability between CNC machines and tools, practical guidance for fabrication is limited. Enhancing access to micromilling could enable researchers to refine and test designs before committing to the costly fabrication of master molds for hot embossing or injection molding.

Our motivation is to develop a microfluidic device that is capable of performing bioanalytical assays such as polymerase chain reaction (PCR), loop-mediated isothermal amplification (LAMP), and recombinase polymerase amplification (RPA). This stems from the vast clinical need for accessible diagnostic tools. For example, according to the American Cancer Society, it is estimated that over 13,000 new cases of invasive cervical cancer will be diagnosed and more than 4,000 women will die from cervical cancer in 2025.[44] Despite the widespread screening available, cervical cancer rates are increasing disproportionally, by 4.4% annually since 2007 in women living in low income communities.[45] A much less invasive diagnostic option, liquid biopsy of cell-free DNA (cfDNA) present in the

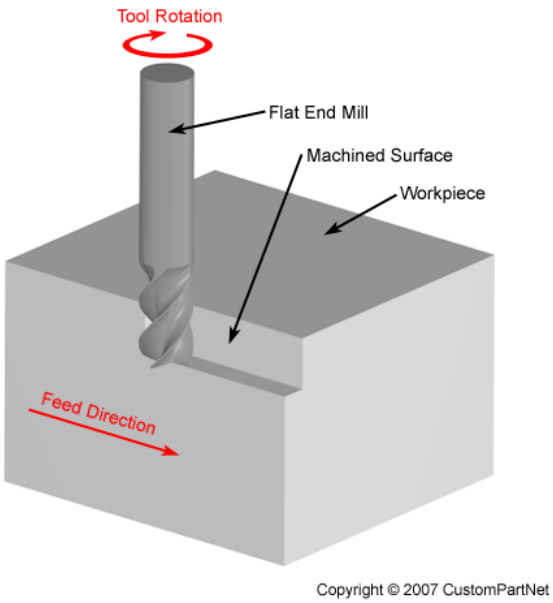


Figure 21: Schematic of the CNC milling process. A flat cutter rotates about its central axis as it moves axially. This movement removes material from the workpiece to pattern the substrate. Image utilized from custompartnet.com

blood stream, offers a promising alternative to traditional pap smear screening and has potential to increase access to women who are less likely to seek preventive screening options. However, cfDNA is extremely low in abundance in the blood stream, and is unable to be detected by clinically available diagnostic methods like quantitative polymerase chain reaction (qPCR).[46] Therefore, further development is needed to develop assays capable of detecting cfDNA. In this work, rapid prototyping is employed for the development of a microfluidic device capable of HPV16 DNA detection by RPA. With future scalability and clinical translation in mind, prototyping in COC will ultimately streamline innovation towards a highly sensitive and specific microfluidic HPV16 cfDNA diagnostic tool.

By developing a low-cost, replicable workflow for micromilling in COC using readily available equipment, we aim to make rapid prototyping in COC more accessible to research labs. Using this workflow, concurrent prototyping with the fluidic design and assay development can be achieved directly in the material intended for clinical or commercial

use. First, to address the challenge of sourcing machinable COC stock, custom COC plaques were created from COC pellets by hot embossing. Then, micromilling parameters, feed rate and spindle speed, where evaluated to generate practical guidelines for producing clean, high-resolution features in COC with a low-cost CNC milling machine (Nomad 3, Carbide 3D). To evaluate these parameters, channel bottom roughness and burr formation were used to assess channel quality and reproducibility. Finally, the utility of this workflow was demonstrated by fabricating a microfluidic device capable of performing quantitative recombinase polymerase amplification (RPA) for HPV16 detection. This proof-of-concept highlights the potential for affordable, iterative development of microfluidic assays in COC, without the need for costly, or high barrier-to-entry equipment.

Materials and Methods

Fabricating Machinable COC Plaques by Hot Embossing

A custom aluminum mold and press was fabricated to produce machinable COC plaques. The mold consists of two parts, a rigid frame and a minimal-tolerance insert that acts as a press. The bottom of the frame consists of shallow recesses to allow excess COC to escape during molding.

The frame was placed into a heated vacuum press (Sublym, Eden Tech), and was equipped with eight mm spacers. The spacers prevented the aluminum insert from fully passing through the frame, which defined a consistent plaque thickness. Spacer height was optimized for the thickness of the mold and press.

To fabricate the plaques, a polyimide (Kapton) sheet was placed on the bottom of the aluminum frame , which provides a smooth surface for the bottom of the plaque. Two grams of COC pellets (Polyplastics USA) were loaded into the press and preheated for three minutes. After preheating, approximately 6-10 psi of pressure is used to force the press into the mold for five minutes. For higher grade COC (6013), often the top side does not

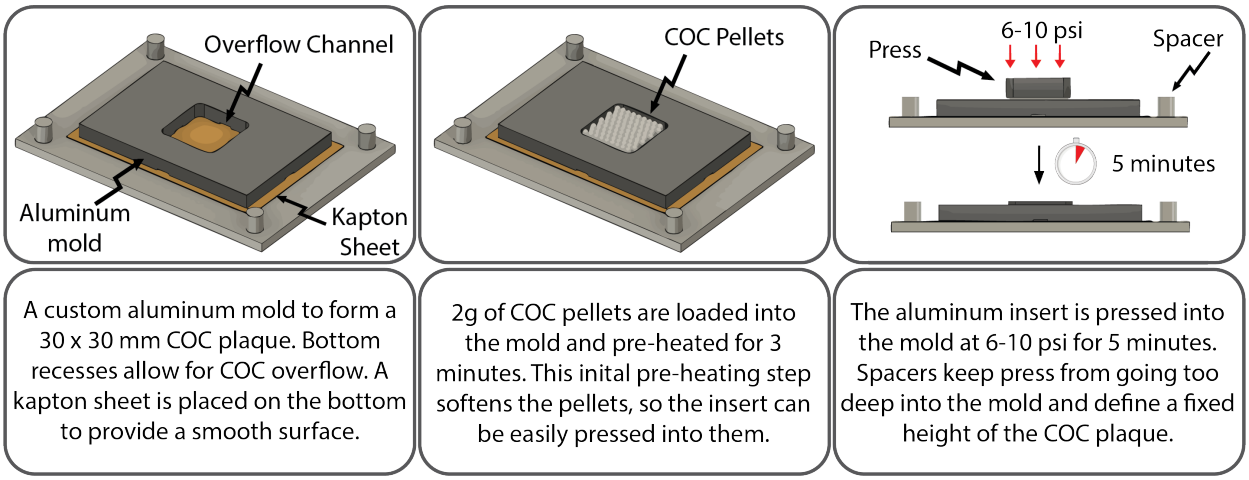


Figure 22: Detailed schematic for the fabrication of cyclic-olefin copolymer (COC) plaques by hot embossing. This method first heat the pellets above their glass transition temperature, then utilizes a rigid aluminum frame and insert to press two grams of COC pellets into a 2±0.2 mm plaques on average. Additional details on fabrication parameters are listed in Table 2

completely homogenize. In these cases, the plaques were trimmed to remove excess material at the edges, flipped over, and re-pressed with the rougher side facing the Kapton sheet. This second embossing step improved uniformity and made the plaques more suitable for downstream machining. The whole embossing workflow is summarized in Figure 22.

Micromachining

Using a consumer-grade CNC (Nomad 3, Carbide 3D, USA) and budget-friendly end mills (Microcut, USA), we demonstrate methods to create precise microstructures without high-end specialty micro-CNCs or specialize tools. This setup increases accessibility for more researchers to prototype microfluidic devices efficiently, reducing both cost and technical barriers to entry.

Tool Selection Carbide square end mills were obtained from Microcut, USA: 51205 (0.5 x 1.5 mm LOC), 51204 (0.4 x 1.5 mm LOC), 51202 (0.2 x 0.4 mm LOC), 82004 (0.004“ x

0.012" LOC), 82002 (0.002" x 0.006" LOC). Additional end mills were obtained from various sources: 1/8 inch square end mill (#201E, Carbide 3D), 1/32 inch square end mill (#122, Carbide 3D), and a 2.9 mm circuit board drill (30211420, M.A. Ford). End mills are cutters that operate similarly to drill bits but are designed to cut material on the diameter of the cutter rather than along the length of the cutter. Instead of drilling down, end mills are intended to cut sideways.

End mill geometry was determined by material properties. Two flute end mills were used to provide the most clearance for evacuation of cuttings. Polymers have a tendency to stick to cutting tools, so providing as much room as possible for cuttings to leave the cutter reduces the likelihood of clogging the end mill and causing the COC to melt instead of cut. The shortest length of cut, the length of the end mill sharpened to be able to cut material should be used to maintain the highest possible tool stiffness. A end mill should not be used to cut a feature deeper than the length of cut or COC is more likely to stick to the tool, preventing cutting from escaping. Only carbide cutting tools should be utilized, due to the ability to run at higher spindle speeds, withstand heavier cutting loads and achieve higher tool sharpness than high speed steel. Tool coatings were not utilized due to sourcing difficulties, but coatings that improve lubricity were considered such as titanium nitride. McMaster-Carr was chosen as the source due to common availability and short shipping times allowing for rapid development of a COC machining process. PCB drills were utilized for creating inlets and outlets due to the low cost and availability. Drilling offers faster material removal than end mills, and was therefore ideal for speeding up the machining process.

Zeroing the Workpiece and Tool Loading In order to locate the COC plaques on the machine's coordinate system a combination of visual alignment was utilized. In the X and Y axes, visual alignment of the tool over the center of the left and back edges can be performed

and then the axis zero set. For the Z axis, a gauge block (McMaster-Carr #1809A152), a precision ground block of a known length, can be utilized with an end mill or drill bit over 2 mm in diameter to find the lowest point at which the block is able to move between the bottom of the tool and the workpiece without binding. The CNC machine can then set the height as the length of the gauge block.

Loading the tool presents one of the greatest risks for tool breakage. To minimize this, a small plastic sleeve was used to protect the tip of the cutter, so only the thickest part of the end mills are being held. Then, to minimize tool runout, the length of the tool below the holder was limited to only the length of the small plastic sleeve. Runout refers to the off axis rotation of the end mill, and while is generally to a very small degree, it can have a significant effect on the quality of cut. High precisions collets (McMaster-Carr #4560N12) should be utilized in order to minimize runout. To zero the loaded end mills, the Nomad includes automatic tool length measuring, where the length of tool below the holder is measured by the machine. Using this method with smaller tools (less than 200 μm) is likely to break the tools during the zeroing process.

Computer-Aided Machining (CAM) Fusion 360 (Autodesk) was utilized as the CAM and design package for this work due to the free availability to researchers while providing a robust CAD and CAM package. Combined CAD and CAM functionality allows for rapid development of iterations by reducing the time needed to toolpath iterations on a design.

Toolpath Selection Toolpaths, how the end mill or drill moves through and around a piece of material, are used to cut devices. Toolpathing of geometry that is not a slot, the width of the tool can become challenging. Figure 23 provides insight on toolpathing common microfluidic features. Facing operations were performed to flatten the COC plagues prior to machining microfluidic channels. Larger cutting tools should be utilized for facing operations, ideally, three-six mm in diameter, since larger tools will require less passes. Cutters over

six mm in diameter may be utilized for this, but higher cutting forces may require a more secure method of workholding. However, using precision clamping may reduce the amount of machinable surface area, so for most microfluidic applications double-sided PSA is the best option for workholding.

Drilling offers a fast method for creating cylindrical features or providing an entry location for an end mill. Inlets and outlets are some of the most common drilled features. Drill bits do not offer a flat bottom, but remove material faster than end mills.

2D contour toolpaths were utilized for cutting channels due to the high degree of control offered in selecting the path and cutting parameters of the tool. Most channels are only as wide as the tool, so this path that follows along a wall gave the control needed to follow this geometry while controlling cut depth and entry and exit parameters.

Clearing features wider than the tool diameter will require multiple passes and selection of the needed area. It is recommended that channel clearing be performed prior to clearing larger areas. For clearing these areas, a 2D adaptive clearing (known as trochoidal milling in other CAM packages) toolpath is recommended. These toolpaths will maintain a consistent axial and radial load on the tool. The consistency of this toolpath is advantageous compared to linear area clearing, which has increased tool contact at corners. The recommended entry method for these paths is a helical ramp at a 2° angle, which will reduce forces on the tool compared to plunging.

Microfluidic devices often feature repeating patterns, so toolpaths can be patterned at the design spacing to speed up device fabrication. Tool libraries with the correct speed and feed rates also speed up toolpath creation. Templates of commonly used toolpaths with the proper settings can also be utilized, so that only the geometry (slot or area) needs to be selected by the user, further reducing the time to toolpath a device. Tool libraries and selected templates for Fusion 360 can be found in the supplemental materials.

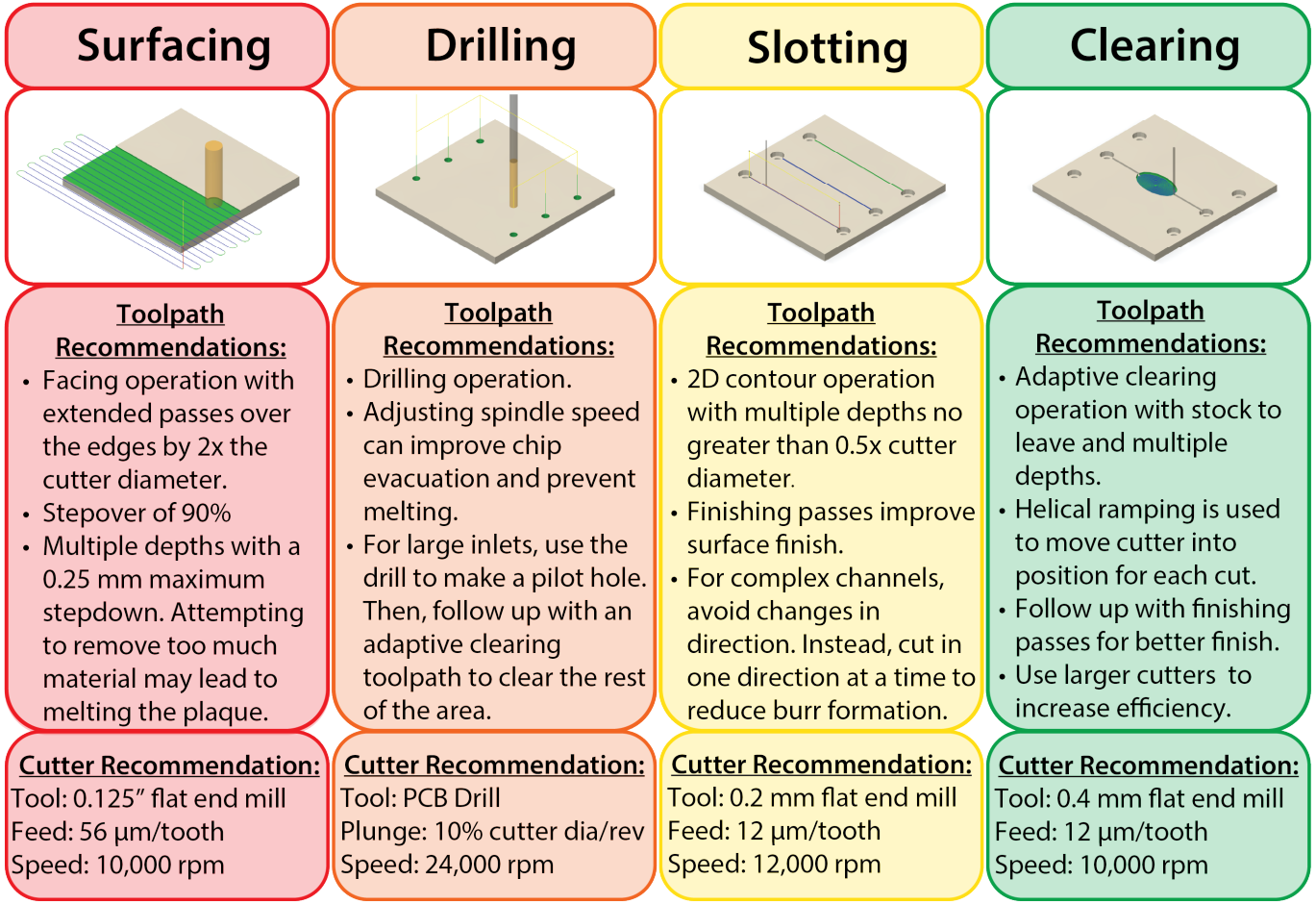


Figure 23: Summary of toolpathing methods used to manufacture microfluidic features. Four main types of toolpaths were used to provide workflow recommendations for fabricating common microfluidic features. Surfacing takes a large end mill remove material so that the future operations have a flat workpiece. Drilling takes a drill bit to cut holes through the material for ports. Slotting operations describe a variety of linear toolpaths that are used to remove material–most commonly used to cut both curved and straight channels. Clearing toolpaths use a larger end mill and are used to remove large amounts of material for relatively large features.

Post Processing of Micromilled COC Chips Brush with toothbrush, then clean in a ultrasonic cleaner in 70% IPA until visibly clean To deburr these channels, a fine toothed brush (Colgate 360 Enamel Health Extra Soft Toothbrush) is first run through all channels and then sonicated in 70% Isopropyl alcohol. If burrs are still visible, then this process is repeated until the device is clean and visibly free of burrs.

Surface Characterization

Surface characterization was performed after surfacing operations, and for the feeds and speeds experiments.

Roughness Measurements Roughness measurements were obtained using a Dektak XTa. After measurements were obtained, a two point normalization was performed on the top of the channels. When evaluating the roughness after surfacing operations, one measurement was obtained for four quadrants each with a 1 mm measurement length. When evaluating the average roughness at the bottom of the microchannels, only approximately 70 μm was evaluated due to the larger size of the stylus.

Flatness Measurements Flatness was measured using a Zeiss Duramax CMM (Model 63651-9905). COC plaques were fabricated from 6013 COC, then a 1/8 inch square carbide end mill was used to perform a surfacing operation. Maximum step size was set to 100. Flatness was measured using 30 points that were manually measured across the surfaced face of the plaque.

Evaluating Optimal Milling Parameters

To characterize the quality of the channels for varying feed rates and spindle speeds, COC plaques were fabricated, surfaced, then straight channels were cut at multiple different feeds and speeds. To evaluate feed rates, the spindle speed was constant at 12,000 rpm

as the following feed rates were evaluated: 0.004, 0.008, 0.012, 0.016, 0.020, 0.024, 0.048 mm/tooth. To evaluate spindle speeds, the feed rate was held constant at 0.012 mm/tooth as the following spindle speeds were evaluated: 6000, 8000, 10000, 12000, 14000, 16000, 18000, 20000, 22000, 24000 rpm. For each of the conditions analyzed, three channels were cut for each to improve statistical power. Then, average surface roughness was measured in three different regions on the bottom of each channel.

Sealing the Chip

To seal the chip, double-sided pressure-sensitive adhesive (ARcare 90445Q) was used to adhere PMMA to the micromilled chip. First, the PMMA was milled down to a 30 x 30 mm chip, then the adhesive was pressed onto it using a soft plastic seam roller (McMaster-Carr #62395T11). Then, the post-processed COC chip was pressed onto the adhesive using the seam roller. Additionally, the chip was placed in the Sublym by Eden Tech and 6-10 psi of pressure was placed on the chip for up to an hour.

Chip-To-World Interface

In order to load the bonded chips with reagents, a custom PMMA frame was milled using the Nomad 3 CNC. The bottom part of the frame features an appropriately sized recess for the sealed chip and the top part has 10-32 tapped holes for each of the inlet/outlet ports. Then, a rubber o-ring was pressed into the bottom of the port holes and the frame was assembled using screws. Next, plastic quick-turn tube coupling sockets (McMaster-Carr #51525K235) were screwed into the ports until the o-ring was visibly compressed against the chip. To fill the chip with reagents, the appropriate volume was dispensed into the plastic fitting, then positive pressure was applied manually using a 3 ml syringe. A detailed schematic is shown in Figure 24.

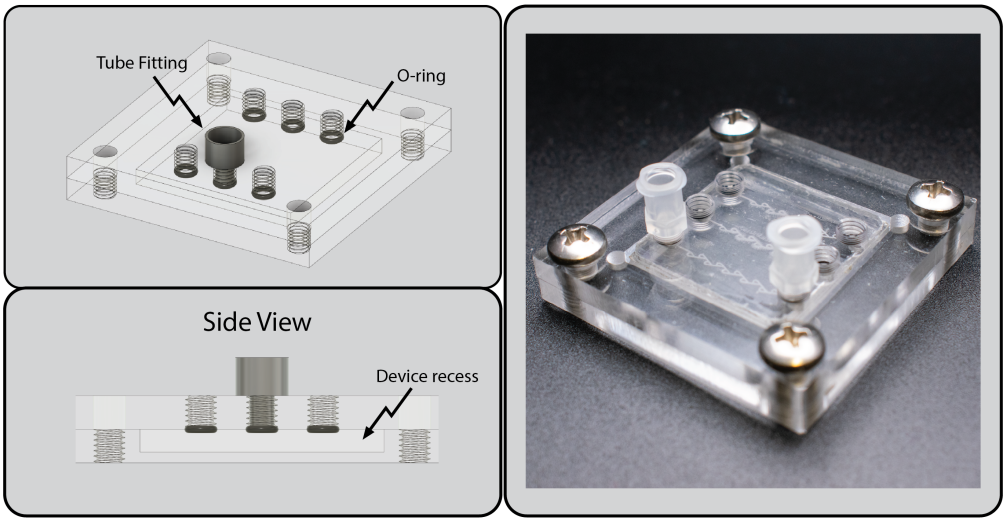


Figure 24: (Left) Schematic of custom chip to world interface. The PMMA clamp holds microfluidic chip in place. An external fitting is screwed into the inlet hole, which presses the rubber o-ring down–acting as a gasket to maintain a seal between the chip's inlet and the fitting. (Right) Image of actual chip-to-world interface with a micromilled COC chip for visualization.

Recombinase Polymerase Amplification in Micromilled COC

To demonstrate the utility of ultra-rapid prototyping in the desired end-material, a recombinase polymerase amplification (RPA) assay was developed. RPA is an isothermal reaction that can perform the exponential amplification of DNA at a range of temperatures between 35 and 45 °C. For simplicity, the TwistAmp Liquid Basic RPA reaction kit (TwistDx, United Kingdom) and the supplied positive controls were utilized to validate the performance of the RPA reaction in the micromilled chip. So real-time reaction monitoring could be performed, 1x EvaGreen (Biotium, USA) was added to the reaction kit. A device was fabricated with a single channel containing a postive control. The device was heated to 40 °C for 90 minutes and fluorescent images were taken at approximately two minute intervals. To evaluate the effects of the reaction on chip, reactions were run simultaneously in tubes using the BioRad CFX96 real-time PCR detection system.

Temperature Control and Real-Time Fluorescent Imaging Temperature control was performed using a programmable temperature controller developed by the McCalla group.[38] A custom clamp was fabricated from PMMA to hold the heating element in direct thermal contact with the micromilled chip (Figure 24). Precise temperature control and homogeneity of heating is imperative for RPA on chip, which performs optimally between 37 and 42 °C.[47] To validate this, as well as homogeneity of heating a FLUKE TiX560 (Everett, Washington) was employed using an emissivity of 0.95.

Real-time fluorescent imaging was performed using a Nikon Ti-E microscope equipped with a Andor EM-CCD (DU-897) camera with a 4x magnification objective and a FITC filter set for illumination.

Real-Time Fluorescence Analysis Fluorescent images were imported into ImageJ for analysis. Using a custom macro, pixel intensity was analyzed for a fixed region of interest for each partitioned reaction. Intensity was normalized to the initial measurement, then the mean inflection point was calculated using excel for each varying concentration. Using this information, a standard curve was generated to validate the initial concentrations of the two positive control samples. These results were compared to the in-tube data, which was analyzed in excel identically.

Results and Discussion

Fabricating Machinable COC Plaques by Hot Embossing

Obtaining machinable COC is difficult because it is most commonly sold in sheets less than 200 μm thick, or as pellets for injection molding applications. Therefore, an alternative method was developed for fabricating machinable COC plaques for grade 8007 and 6013 TOPAS COC.

Table 2: Summary of Parameters for embossing plaques from grade 8007 and 6013 TOPAS cyclic-olefin copolymer (COC). Embossing temperatures vary based on the glass transition temperature of the respective grade of COC. An additional pre-heating step is performed once the pellets are loaded into the mold to soften them prior to the embossing process. This method is summarized in Figure 22

	COC Grade	
	8007	6013
Temperature	130 °C	180 °C
Pressure	6–10 psi	6–10 psi
Time	300 s	300 s

[1] For grade 6013 plaques, the process may need to be repeated on both sides.

Using a custom aluminum mold, COC plaques were successfully fabricated under simple conditions (Table 2). Specifically, two grams of COC pellets were placed inside the aluminum mold, then heated and pressed for five minutes at approximately 6-10 psi. The temperature and pressure conditions for embossing both 8007 and 6013 TOPAS COC plaques are summarized in (Table 2). While plaques from grade 8007 COC homogenized easily, the higher grade 6013 COC often required additional time–often up to 15 minutes–to remove air within the plaques. The mold dimensions and spacer distance were optimized for 2 grams of COC pellets, producing plaques 30 mm $\times$ 30 mm in area and were approximately 2 ± 0.2 mm thick on average. However, this setup can be modified for different plaque sizes as needed.

Due to the press design, one side of the resulting plaques–the side in contact with the Kapton sheet–was consistently smoother than the opposite side. Surface roughness was not crucial at this step, since all plaques were surfaced prior to microchannel fabrication to ensure uniform depth. However, the smoother side provided better optical clarity for imaging and was preferred for the bottom surface of finished devices.

Evaluating Optimal Milling Parameters

In the machinist community, the term "Feeds and Speeds" is commonly used to describe two fundamental parameters: the feed rate of the cutter and the spindle speed. The feed rate is defined by the length of material that is being cut per tooth on the end mill, or expressed in the linear speed of the machine. Feed rate per tooth is defined as how far the cutter advance per each cutting edge on the tool, generally in units for mm/tooth. End mills have varying numbers of cutting edges (teeth) called flutes, generally two to five. The end mills used for these results all have two flutes. The other feed rate number used is the linear speed of the machine, usually expressed in mm/min, which is what the CNC machine will show as the feed rate. If the feed rate is too high, then too much material is being cut leading to tool clogging or tool breakage. If too low, then the cutter will skip along the workpiece without removing material and instead melts it. Speed refers to the number of rotations per minute (RPM) of the spindle; excessively high or low speeds can cause excess heat generation at the cutter-workpiece interface, which can cause the material to melt. In general, manufacturers will provide recommendations for the feeds and speeds for their cutters in different materials; however, when using microscopic end mills in unique materials, there are not recommendations. To address this gap, reference parameters were developed for the feed rate and spindle speed for machining in TOPAS COC grade 8007 and 6013 (Polyplastics USA).

Surface quality during micromilling was evaluated based on two metrics: the average surface roughness at the bottom of the channels and the extent of thermal damage along the channel walls. Surface roughness was measured using a stylus profilometer (Dektak XTa), and thermal damage was assessed via optical imaging using a stereoscope. A detailed summary of surface roughness is found in Figure 25. To evaluate optimal machining parameters, both feed rate and spindle speed were systematically varied, and the effects on channel surface roughness and heat-induced wall damage were evaluated.

Statistical analysis was performed to identify significant trends and evaluate process variability.

To establish a range of feed rate recommendations for milling in COC, a series of straight channels were cut using a 200 μm flat end mill (Microcut USA, 51202) across a range of feed rates between 0.004 mm/tooth and 0.048 mm/tooth. Data was first evaluated for normality and homogeneity of variance. For grade 8007 COC, surface roughness measurements passed tests for normality and equal variance (Shapiro-Wilk, Levene's test); therefore, one-way ANOVA followed by Tukey pairwise comparisons was used. For grade 6013 COC, normality assumptions were not fully met, so Kruskal-Wallis testing followed by Dunn's comparisons were employed. Both grades of COC were able to be cut at a wide range of feed rates. For 8007 grade COC, melting is observed above 0.024 mm/tooth, whereas grade 6013 tolerated feed rates up to 0.048 mm/tooth. When evaluating the effects on increasing feed rate on the surface roughness at the bottom of the channel for grade 8007 COC, the only statistically significant ($p=0.0304$) increase in surface roughness was observed between the lowest feed rate (0.004 µm/tooth) and the highest feed rate (0.024 mm/tooth). Furthermore, for grade 6013 a wider range of feed rates were evaluated (0.004 to 0.048 mm/tooth) where the only statistically significant ($p=0.0625$) increase in surface roughness was observed between 0.012 and 0.020 mm/tooth. These findings suggest that there are a wide range of feed rates that can produce an acceptable quality surface finish at the bottom of the channel. Additionally, it is important to note that these findings are agnostic to the extent of burr formation from poor chip evacuation, and heat effects along the walls of the channels.

The spindle speed also can influence surface quality. While increasing spindle speeds is generally favored for micromilling in polymers, preliminary testing showed that excessively high speeds in 8007 led to thermal damage, an effect which did not appear in 6013 grade COC under our operating parameters. To evaluate the optimal spindle speed, a series of straight channels were cut using a 200 μm flat end mill (Microcut USA, 51202) at spindle

speeds ranging between 6,000 and 24,000 rpm and quantified. Surface roughness data across spindle speeds were analyzed using Kruskal-Wallis tests, as assumptions of normality were not consistently met. Then, pairwise comparisons were performed with Dunn's test. As found with feed rates, both grades of COC were able to be cut at a wide range of spindle speeds. For grade 8007 COC, the 14,000 rpm spindle speed is outlying from the data due to excessive burr formation within those channels. This may be due to many factors including excessive runout, tool breakage, or melting of the material. Therefore, the recommended range of spindle speeds for 8007 is between 8000-12000 rpm. While no statistical significance was found between the spindle speeds for grade 6013, more moderate spindle speeds (between 10000-20000) will prevent excessive heat at the cutter-material interface. For 8007 grade COC, melting is observed above 16000 rpm, whereas grade 6013 tolerated up to 24000 rpm. This further demonstrates that higher grade COC protects from the side effects of the extremes of high/low feeds and speeds. This is most likely due to the higher thermal stability of the 6013 grade (due to the increased % norbornene).

Despite the wide range of acceptable feed rates, better quality surface finishes were observed around 0.012 mm/tooth and 12,000 rpm for both grades. After cleaning the channels with a soft bristle brush, many of the burs are effectively cleaned out, which can hide the effects of a poor quality cut. However, 8007 grade COC still has a significant amount of burring and thermal damage. So, it is recommended that higher grades of COC are used for most micromilling applications to prevent excessive burr formation. To combat this issue, others have effectively enhanced the surface finish along the walls of the channels using a chemical solvent to dissolve the channels, rendering them must more flat.[48] Although this may be effective, improving the quality of the channels obtained from optimized cutting parameters is more advisable than excessive post-processing techniques. This ensures the highest quality of microchannel, rather than attempting to hide the effects of poor milling technique.

Table 3: Recommended range of feeds and speeds for slotting operations in COC. These recommendations are based on iterative prototyping and optimal parameters can vary greatly for different applications and different machines. Feeds and speeds for the 200 μm end mill were evaluated based on the results from Figure 25.

	Cutter Diameter				
	1/8 in	1/32 in	0.5 mm	0.4 mm	0.2 mm
Feed Rate[1]	36-64 μm	16-48 μm	10-24 μm	6-16 μm	8-12 μm
Plunge Rate[2]	18-32 μm	8-24 μm	5-12 μm	3-8 μm	4-6 μm
Speed (rpm)	10k	12k	12k	12k	12k
SMM (m/min)	99.7	29.9	18.8	15.1	7.54

[1] Feed rate is defined by the μm/tooth. [2] Plunge rate is defined by the μm/revolution.

Based on surface roughness measurements, optical assessments, and observed thermal damage, moderate feeds (approximately 0.012 mm/tooth) and spindle speeds (10,000-16,000 rpm) are recommended for rapid prototyping in both grades of COC using a 200 μm end mill. For other diameter end mills, spindle speed is kept within the recommended range, and feed rates are representative of the results obtained from iterative prototyping, as shown in Table 3. Using these parameters, consistent channels were fabricated using a consumer grade CNC mill with minimal burr formation and thermal defects, while remaining robust to the inherent variability of a low cost machine.

Machining Different Example Geometries

There are several features that are common to most all microfluidic chips: inlets/outlet ports and interconnected channels. To demonstrate the utility of the optimized milling parameters, several basic geometries were fabricated in COC plaques. These examples illustrate key considerations when translating computer-aided manufacturing (CAM) designs into functional devices.

Importance of Workpiece Flatness Uniform thickness of the workpiece is crucial for consistent microchannel depth and quality sealing during device assembly. When attempting

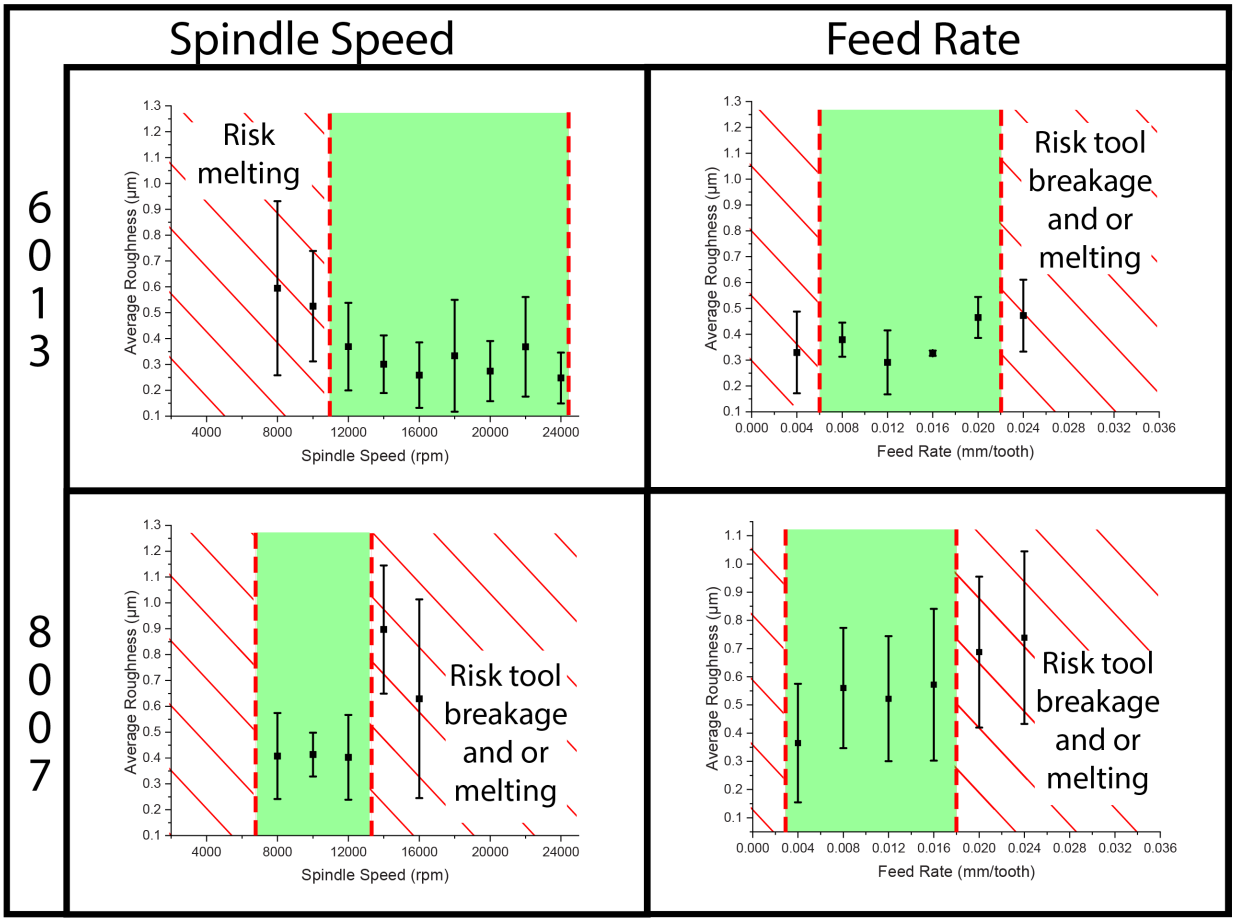


Figure 25: Summary of average roughness across 200 μm straight channels in grade 6013 and 8007 COC. For feed rate measurements, spindle speed was held constant at 12,000 rpm. For spindle speed measurements, feed rate was held constant at 12 μm per tooth.Regions shaded in green are considered moderate feed rates and spindle speeds, which were used define the recommended range described in Table 3. Regions that are hatched highlight feed and speed rates that caused the material to melt and adhere to the end mill and or caused tool breakage; therefore, roughness measurements were not able to be obtained.

to mill features for microfluidics, it is imperative that the workpiece is flat. During the fabrication of the COC plaques, large differences in thickness can be observed across the plaque (average thickness was 2±0.2 mm. Therefore, a facing operation was performed on each plaque prior to microfabrication. Facing was performed using a 1/8 inch flat end mill (#201E, Carbide 3D). This tool size provided a balance between minimizing step lines and staying Within the capabilities of the Nomad 3 CNC from Carbide 3D. Ideally, a larger fly cutter would further reduce surface irregularities, but in this case, flatness was measured to be 6.12±1.25 μm flatness on average, which is sufficiently flat for prototyping applications. Additionally, average roughness of surfaced 6013 plaques was measured to be 0.5425 ±0.178 μm.

Drilling Inlets and Outlets Cutting ports for fluidic connections was performed by drilling through the COC plaques using a PCB drill bit of the appropriate diameter (M.A.Ford 3020550). Drilling was performed at a plunge feed rate of approximately 10% of the cutter diameter per revolution, with a starting spindle speed of 24,000 rpm. If melting or poor chip evacuation was observed during drilling, reducing the spindle speeds proved effective in minimizing the thermal damage and improving hole quality. Through-holes produced with this method exhibited clean edges and consistent diameters, enabling reliable external connections.

Milling Microchannels and Complex Geometries The machine used for milling (Nomad 3, Carbide 3D) features a minimum motion resolution of 25 μm and uses an open loop stepper control system. Since there is not feedback for machine position, the machine can have error on the location of the cutter, causing inconsistent channel width and depth. Dimensional accuracy was assessed by measuring channel widths and depths relative to design values (Figure 26. To evaluate the consistency of channel width and depth, profilometry measurements were taken for 18 straight channels (9 were milled in 6013 and

the other half in 8007) with a desired depth of 200 μm. It was found that the average width was 216.4 $\pm$9.2 μm and the average depth was 122.8 $\pm$3.4 μm. These results demonstrate that there is variability in channel dimensions, which should be taken into account for any advanced applications, however, is sufficient for many prototyping applications. The most likely source of error in channel width is tool runout, when the tool is not spun along the geometric centerline, causing eccentricity. The amount of eccentricity leads to a wider channel since the tool no longer rotates about the shank's geometric centerline. This eccentricity is a major source for why smaller diameter end mills were not run successfully, since eccentric rotation causes uneven loading on the cutting edges of the tool. When this difference exceeds 2% there is a significant load imbalance between the cutting edges, causing bending and tool breakage.[49] Tool runout is affected by the spindle design, tool tolerances, and holder geometry and quality. A high-quality collet (McMaster-Carr #4560N12) was utilized to improve runout in the Nomad 3 spindle. Decreasing the length of the tool that sticks out of the collet also reduces runout, so the minimum stick out should be used whenever possible.

Channels and more complex features were machined using two-dimensional contour toolpaths. During prototyping, the most common issue that arose was burr formation. Burrs are small pieces of the material that were removed from the workpiece, but melted and adhered to the walls of the channel. To minimize burr formation, depth-of-cut strategies were adjusted to include multple shallow passes, reducing the load on the tool and improving chip evacuation. For more intricate features, adjusting the toolpath so that it follows the direction of fluid flow also helped protect from burr formation. Figure 26 demonstrates the toolpathing for three geometries, which produced the high quality features during the prototyping process. Although proper toolpathing is crucial, machine dynamics–particularly during directional changes–also significantly impact surface finish. When the CNC mill decelerates, accelerates, or changes in direction sharply, minor imperfections arise–

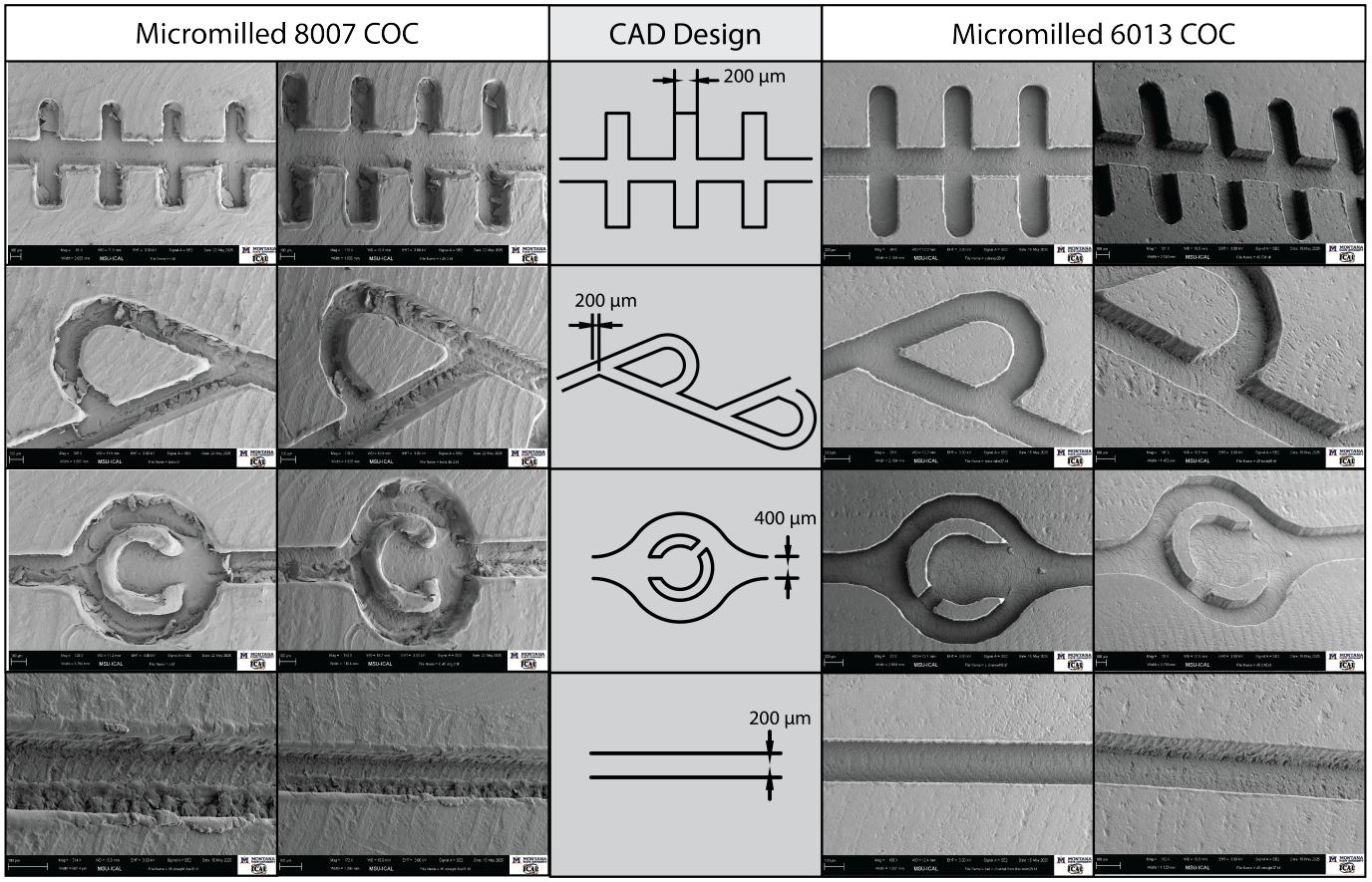


Figure 26: Comparison of complex geometries that were micromilled in grade 8007 cyclic-olefin copolymer (COC) compared to 6013 COC. Grade 6013 COC displayed much higher resilience to the thermal effects, whereas grade 8007 COC has channel deformation, excessive burr formation and additional large defects. The original design in illustrated in the middle and the feature height for all designs is 100 μm. All designs were milled using a 200 μm end mill with a 12 μm/tooth feed rate and 12,000 rpm spindle speed. All images were taken using the field emission scanning electron microscope (Zeiss SUPRA 55VP) at the Imaging and Chemical Analysis Laboratory (ICAL) at Montana State University.

particularly burring. To minimize these effects, finishing passes were successful at removing larger defects. Additionally, after machining several cycles cleaning with a hard bristle brush and ultrasonic cleaning in a 70% IPA bath were successful at removing burrs. Although some defects remained, the bonding process described in the next section was agnostic to them.

6013 grade COC was used for functional devices. It was found that the lower glass transition temperature of 8007 grade COC 78 °C, led to more burr formation, heat transfer into chips and an observed less reliable surface finish (Figure 26). The more substantial burr formation is likely linked to thermal effects since in most materials, most of the heat generated by cutting goes into the cuttings and a small amount is transferred into the bulk material. 8007 grade COC has a low enough glass transition temperature that the heat being generated in the bulk material is sufficient to soften the material enough to cause material deformation instead of cutting, leading to more burr formation than 6013 grade COC. This deformation also explains the more reliable surface quality, since 6013 grade COC with a glass transition temperature of 142 °C was more tolerant of heat generation, leading to more consistent surface quality. Heat generation is linked to the speed and feed rates, with lower speeds causing less heat generation than higher speeds. An ideal feed rate will cut fast enough to transfer most heat into the cuttings instead of the workpiece. Too high a feed rate can generate enough heat to soften the cuttings and cause adhesion to the end mill, making the removal of the cuttings from the tool challenging.

Recombinase Polymerase Amplification in Micromilled COC Chip

The goal of this work was to develop a microfluidic device capable of supporting real-time quantitative recombinase polymerase amplification (RPA) for nucleic acid detection. To evaluate compatibility, the TwistAmp Liquid Basic RPA kit (TwistDx, United Kingdom) and its supplied positive controls were used to validate reaction performance within the micromilled chip. Use of the commercial kit minimized risk of contamination and provided

a reliable baseline for evaluating compatibility in-chip. The reaction was prepared as instructed, except 1x EvaGreen intercalating dye was added to allow real-time fluorescence monitoring. For this initial testing, a single micromilled microchannel featuring a series of Tesla valves was filled with the reaction mix. In parallel, three positive control reactions and one non-template control (NTC) were performed in standard PCR tubes.

Fluorescent images were obtained at fixed intervals, then analyzed in ImageJ. A measurable increase in mean fluorescence intensity—quantified via mean gray value—was observed in the on-chip reaction over time (Figure Figure 27). The in-tube positive control samples demonstrated a similar reaction shape to the on-chip sample. Interestingly, the NTC sample also exhibited a slight increase in fluorescence, reaching a final intensity approximately 20% that of the positive controls. This may indicate low-level nonspecific amplification or minor contamination. These results are preliminary and limited by several experimental factors. Most notably, approximately 30 minutes elapsed between reaction initiation at room temperature and the start of external heating and fluorescence imaging. This delay likely impacted the onset and progression of amplification. Furthermore, the on-chip reaction was performed without replicates, and the extended room-temperature incubation could have permitted premature amplification prior to proper thermal control. Despite these limitations, this experiment demonstrates that RPA is functionally compatible with micromilled COC devices bonded using ARCare 90445Q double-sided adhesive. The reaction proceeded without obvious inhibition, suggesting that neither the COC substrate nor the adhesive interferes significantly with enzymatic function.

These results are promising and future work to optimize RPA on-chip should be performed. First, mechanisms to reduce the delay between reagent loading and heating, potentially by automating the process, or redesigning the chip to have fewer ports. Additionally, a custom reaction mix may be developed to incorporate a hot-start BST polymerase to prevent premature amplification during loading. Also, alternative quantification strategies,

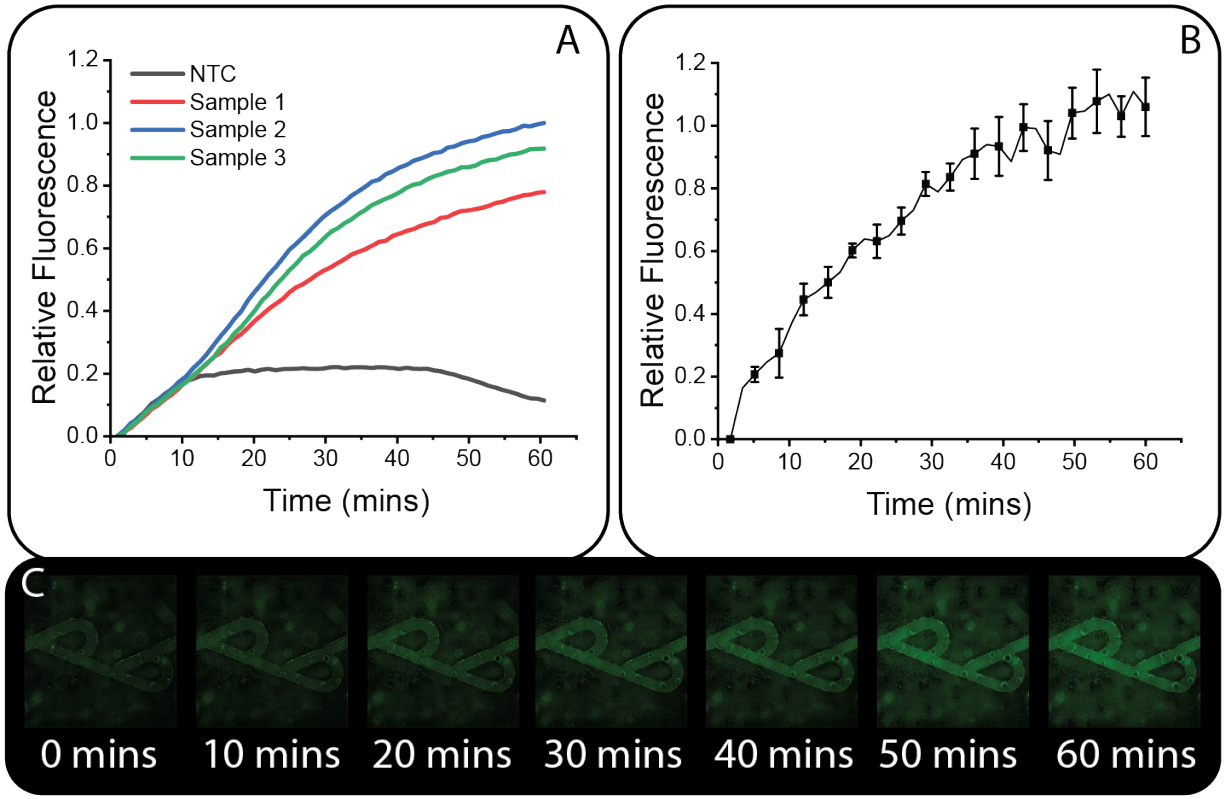


Figure 27: (A) Graph of the real time fluoresence of RPA performed in tubes performed concurrently with the micromilled chip. (B) Graph of the average real time fluorescence of RPA performed in micromilled COC chip. Three data points were taken across the microchannel and the mean gray value was determined for each point at approximately two minute intervals over a hour. (C) Images taken throughout the 60 minute reaction incubation in micromilled chip. Brightness was enhanced and green pseudocolor was overlayed in ImageJ for ease-of-visualization.

such as end-point analysis through digital RPA can be investigated. However, digital RPA in micromilled devices remains a challenge due to the difficulty of fabricating sufficiency reaction partitions at the sub-nanoliter scale. Lastly, for future experiments, additional replicates with a non-template control and expanded target concentrations should be evaluated to validate the measurable detection range. As operation of the custom chip-to-world integration is refined, increased consistency and efficiency in channel are anticipated. In summary, these findings support the feasibility of performing RPA in bonded COC chips and motivate continued development toward a fully quantitative diagnostic platform.

Conclusion

Rapid prototyping tools are critical for bridging early-stage research and development with downstream clinical translation. The most popular method for rapid prototyping is stereolithography (SLA) 3D printing which is often incompatible with many biological and bioanalytical applications.[17,19] Further, thermoplastics, like cyclic-olefin copolymer, are much more widely utilized industrially because they are easily scalable and have excellent material properties. Specifically, COC demonstrates excellent chemical resistance, biological compatibility, optical clarity and very low water absorption, to name a few.[24] Unfortunately, rapid prototyping methods for COC are limited to three main methods: micromachining, laser ablation and xurography. All three methods have been historically minimally documented by researchers, which presents a critical knowledge barrier in using these methods. Of the three methods, micromachining was particularly advantageous due to the low barrier of entry to desktop CNC mills, however there is a critical gap in information on best practices for micromachining in COC. This work addresses the critical gap between rapid prototyping and end-use material fabrication for microfluidic diagnostics by enabling device fabrication directly in COC using an affordable benchtop CNC (Nomad 3, Carbide 3D) and end mills (Microcut USA).

Prior to working at micromachining in COC, the lack of accessibility to machinable COC substrates had to be addressed. COC is commonly distributed as pellets for injection molding, or as sheets for hot embossing or lamination. Therefore, we developed a reproducible method for hot embossing machinable plaques from two grades of COC (8007 and 6013). We demonstrated that using a simple aluminum frame and heated press can create uniform (2 $\pm$ 0.2 mm thick) machinable plaques from two grams of COC pellets. Next, we sought to add to existing work with micromilling COC by evaluating the optimal feed rates and spindle speeds in both grades of COC using a 200 μm end mill. It was found that at the extreme feeds and speeds, COC would melt or the tool would break. As such, only a moderate range of feeds and speeds were evaluated: feed rates between 4-36 μ/tooth and spindle speeds between 8000-24000 rpm. Grade 6013 COC demonstrated much higher resilience to the thermal effects at the tip of the cutter compared to grade 8007 COC. As such, grade 8007 COC was only able to be evaluated for feed rates between 4-24 μ/tooth and spindle speeds between 8000-16000 rpm before melting or tool breakage was observed. This is consistent with the nearly 15% more norborene present in 6013 COC compared to COC (35% total) which increases its glass transition temperature to 142 °C–64 °C higher than grade 8007 COC. Further, it was found that there are a wide range of moderate feeds and speeds that can be used to produce high quality straight channels which are presented in Table 3.

While the optimal feeds and speeds are an important starting point, optimizing the toolpathing–the way the machine is programmed to cut material–has a large impact on the quality of produced device. As such, extensive iterative trial-and-error led to the loss of many consumables, but also yielded toolpathing techniques which can help guide future researchers towards producing higher-quality prototypes. These practical techniques are described extensively in the methods section, but are also summarized in Figure 23. Beyond this, to increase the accessibility and reproducibility of this workflow, all fabrication steps

utilized widely available equipment: the Nomad 3 CNC ($2800 at the time of publication), microcut end mills (approximately $50 each), McMaster-Carr consumables and Fusion 360 for CAM software. This pipeline is accessible to most academic labs, requiring only a consumer CNC and basic CAD/CAM software. Additionally, practical and accessible post-processing strategies, such as soft-bristle toothbrushes and IPA sonication, where utilized to achieve clean channels without specialty solvents or tools. This post-processing, while minimal, was effective at clearing all minor burrs from micromilled 6013 COC, producing microchannels that are suitable for many rapid prototyping–or low-throughput academic or industrial applications–without requiring chemical polishing or cleanroom infrastructure.

Important limitations to these findings are due to inherent variability between machines, tooling and operators. For example, dimensional variability was observed due to the Nomad 3's open-loop stepper control system and spindle runout. It was observed that the average channel width for a 200 μm straight channel was 216.4 $\pm$9.2 μm and the average depth for a 100 μm deep channel was 122.8 $\pm$3.4 μm Additionally, miniature end mills (<200 μm) were evaluated, however they are not discussed because they were extremely unreliable due to breakage and runout sensitivity. This is likely due to poor rigidity of the cutter, and the imbalance of the spindle when operating at higher rpm. This highlights a tradeoff between resolution and tool stability on lower-cost platforms. Despite this, future investigations into optimization of even smaller end mills should be explored because they would have massive utility for rapid prototyping extremely small microfluidics. Lastly, due to the poor quality result observed with 8007 COC compared to 6013 COC, toolpath optimization and further experimentation was performed in 6013 COC. Therefore, there may be value in additional investigations to toolpath optimization for applications where lower grade COC is necessary.

To demonstrate the feasibility of concurrent development of a bioanalytical assay and the microfluidic device, preliminary testing was performed on recombinase polymerase amplification in micromilled COC devices. This preliminary testing supports the hypothesis

that RPA can be performed in micromilled COC bonded to ARCare 90445Q double-sided pressure sensitive adhesive. It was found that there was a measurable and observable increase in fluorescent signal of RPA positive controls performed in chip. Additionally, in-tube controls run concurrently further support this hypothesis. These preliminary tests provided great insight into future pain points with performing quantitative RPA on chip. The largest of these being the excessive amount of time it took to fill individual channels. As a result, there was an over 30 minute delay between the reaction initiation and heating the device and obtaining fluorescent imaging. As such, future development will explore alternative, more efficient methods for filling devices, exploring the design of a custom RPA reaction mix containing a warm-start BST polymerase, and end-point quantification methods (like digital RPA). Prototyping in COC allowed for a platform to begin development of point-of-care nucleic acid detection devices, much earlier than what would have been possible with prototyping via hot embossing or injection molding.

In conclusion, a reproducible, low-barrier workflow for fabricating COC microfluidic devices by micromilling is presented. This method lays the groundwork for future efforts to integrate biochemical assays into industry-relevant platforms without sacrificing fabrication speed or accessibility. Specifically, future work will explore more efficient and reliable methods for integrating nucleic acid detection reactions into micromilled devices.

FUTURE WORK: HOT EMBOSSING CYCLIC-OLEFIN COPOLYMER MICROFLUIDIC DEVICES FOR DIGITAL NUCLEIC ACID DETECTION

Introduction

Rapid prototyping methods for fabricating microfluidic devices are excellent for producing proof-of-concept devices and prototyping. As shown in previous chapters, the lower limits of feature resolution were reached in both 3D printing and micromilling without upgrading to custom equipment. DLP 3D printing produced 100 μm wide channels and micromilling in COC produced 200 μm channels. However, these methods are not suitable for industrial manufacturing for poor scalability and consistency. Further, for some bioanalytical applications much smaller resolution is required so that sufficiently small volumes can be achieved. For example, for digital polymerase chain reaction (dPCR) reactions need to be partitioned into nanoliter volumes which requires microfluidic architectures that cannot be achieved with most rapid prototyping methods. Soft-lithography methods can be employed to develop these architectures, however as discussed previously, PDMS is not an optimal material for most bioanalytical applications because it can adsorb and absorb the reaction contents. Additionally, as discussed previously PDMS is the most widely used material for research-based microfluidic applications, but thermoplastics are used industrially because they can be manufactured using high-throughput methods that produce consistent, high-resolution devices.

High-throughput manufacturing of thermoplastic-based microfluidics is enabled through methods such as hot embossing and injection molding. Injection molding involves heating a thermoplastic until it is in a liquid state, then injecting it into a mold under high pressure (Figure 28). This is the most commonly used method for manufacturing at the industrial scale because it is the most scalable and is the most consistent and reproducible. Hot embossing involves pressing sheets of thermoplastic into a rigid mold at high heat and

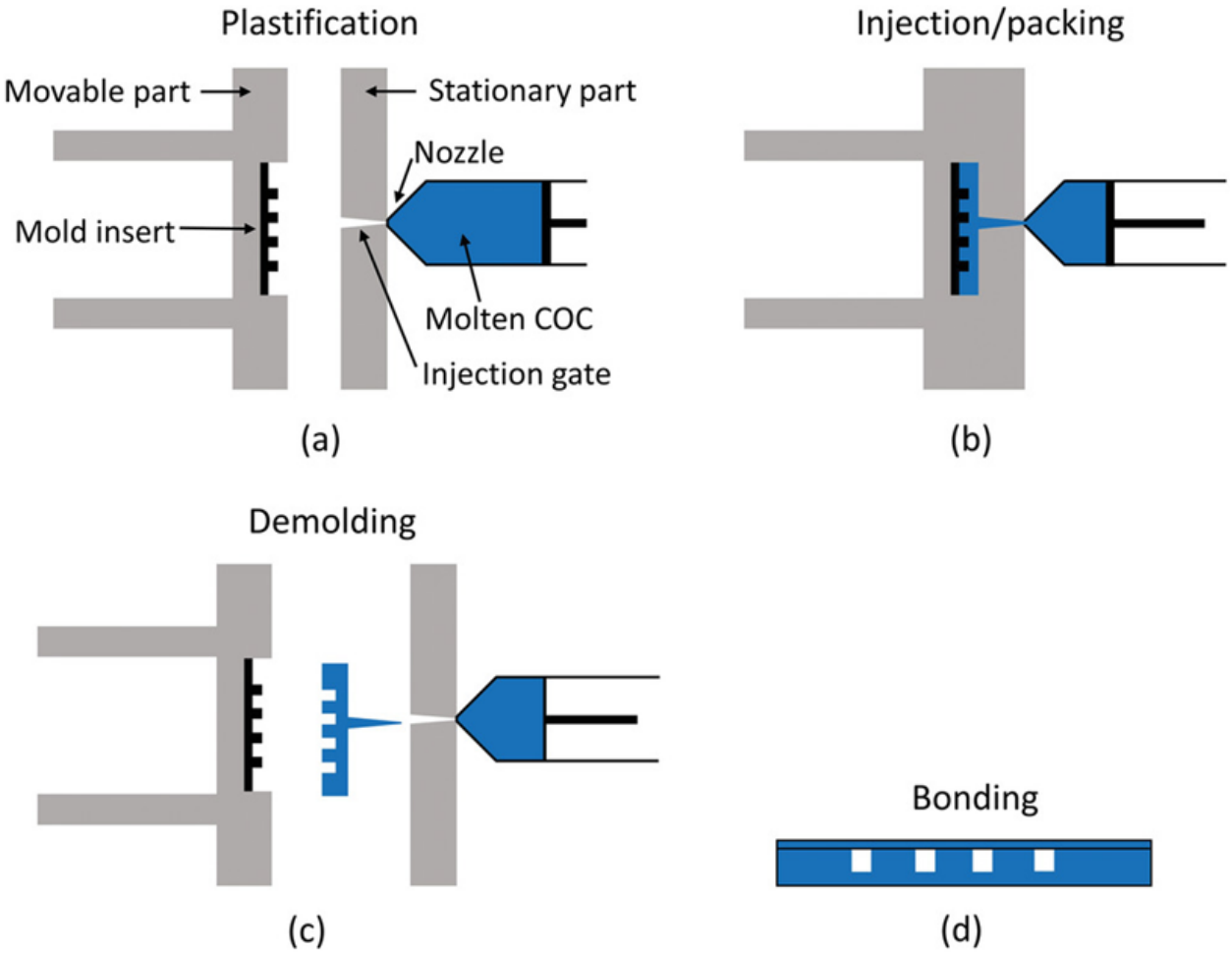


Figure 28: Schematic of the injection molding fabrication process. (a/b) Molten thermoplastic is injected into the mold chamber under high heat and pressure. (c) Then, the formed device is cooled and removed from the mold. (d) Lastly, the microfluidic device must be bonded to enclose the microchannels. Figure used from Agha et al. [24].

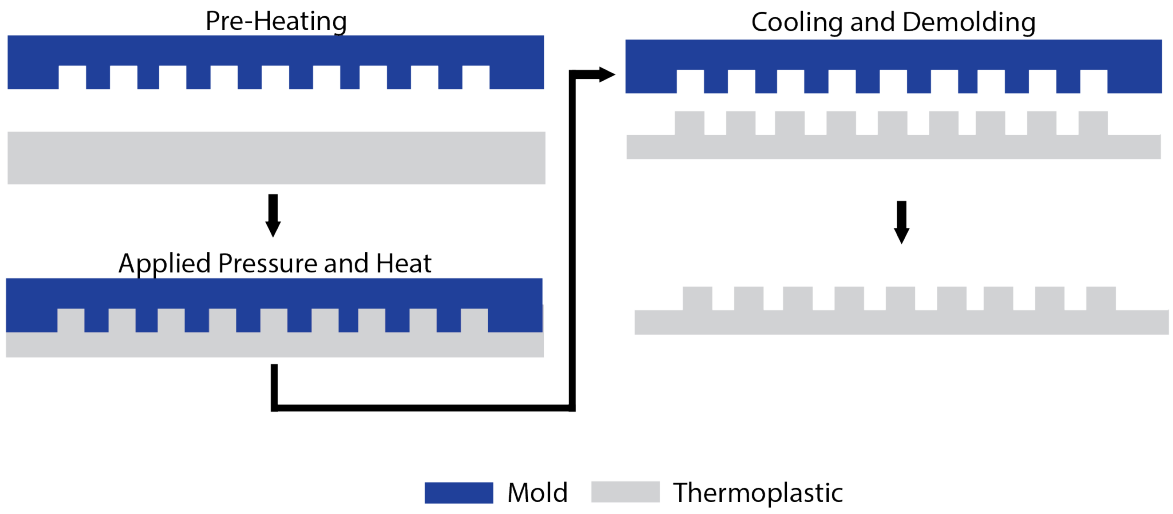


Figure 29: Schematic of the hot embossing fabrication process. The mold and thermoplastic is first preheated, then the mold is pressed into the thermoplastic for several minutes. Then, the mold and thermoplastic are allowed to cool and then they are separated.

pressure to mold the device (Figure 29). Hot embossing, though still considered to have moderate throughput, is not as widely used for very large scale production processes, but is still commonly found in processes where injection molding is not possible, or moderate throughput is acceptable.

Combining both of these methods, the Fraden group introduced a hot embossing protocol that utilizes soft-lithography to fabricate the master mold for hot embossing COC [27]. A schematic overview of this method is provided in Figure 30. Soft lithography enables the production of high resolution microstructures, however it is used to mold PDMS which has a low young's modulus–1.32–2.97 MPa.[50] Due to it's low young's modulus, PDMS will deform under high pressure, which is required for hot embossing workflows. To overcome this, the Fraden group created a low-tolerance aluminum mold to prevent lateral deformation of the PDMS master while using it as a mold during hot embossing. Using this method, Aghvami et al. [27] produced high resolution triple depth microchannels in COC by hot

embossing both COC sheets and pellets. In this chapter, attempts toward reproducing this method to fabricate hot embossed COC devices is discussed. Challenges with replicating the method are discussed and suggestions are provided for future directions for scaling the designs presented using the rapid prototyping methods in previous chapters.

Materials and Methods

Multiple Depth Photolithography

To produce complex geometries that are capable of partitioning individual reactions for digital nucleic acid detection, multi-depth soft-lithography was utilized. An overview schematic of this method is described in Figure 31.

Cleanroom equipment was made available through the Montana Microfabrication Facility (MMF) at Montana State University. The first layer was designed to be 5 μm thick and is patterned only with the alignment markers. SU-8 3010 (Kayaku Advanced Materials, Westborough, MA) was spin coated onto a 100 mm silicon single-side polish wafer (University Wafer, Boston, MA) using a Laurel Spin Coater (Model: WS-400-6NPP) with a two step protocol (Table 4). Then, a soft bake was performed on a hot plate for 130 seconds at 95 ∘C, followed by a 19.8 second light exposure (110 mJ/cm^2 total exposure energy) with an in line PL-360LP filter (Omega Optical, Brattleboro, VT) to pattern the features on the mylar mask (ArtNetPro, San Jose, CA). Then, a post exposure bake was performed first for 1 minute at 65 ∘C on one hot plate, then transferred to another hot plate for 70 seconds at 95 ∘C. Lastly, a 2 minute developing bath with agitation was performed in 100% SU-8 developer (Kayaku Advanced Materials, Westborough, MA).

Layer 2 was designed to be 10 μm thick, so a slower spin coating step was performed (Table 4). Then, a 10 minute soft bake at 95 ∘C, followed by a 23.1 second exposure– overexposing by 150%. Then, a post exposure bake was performed for 1 minute at 65 ∘C and 2 minutes at 95 ∘C. Layer 3 repeated layer 2, but required a post-exposure bake at 65 ∘C

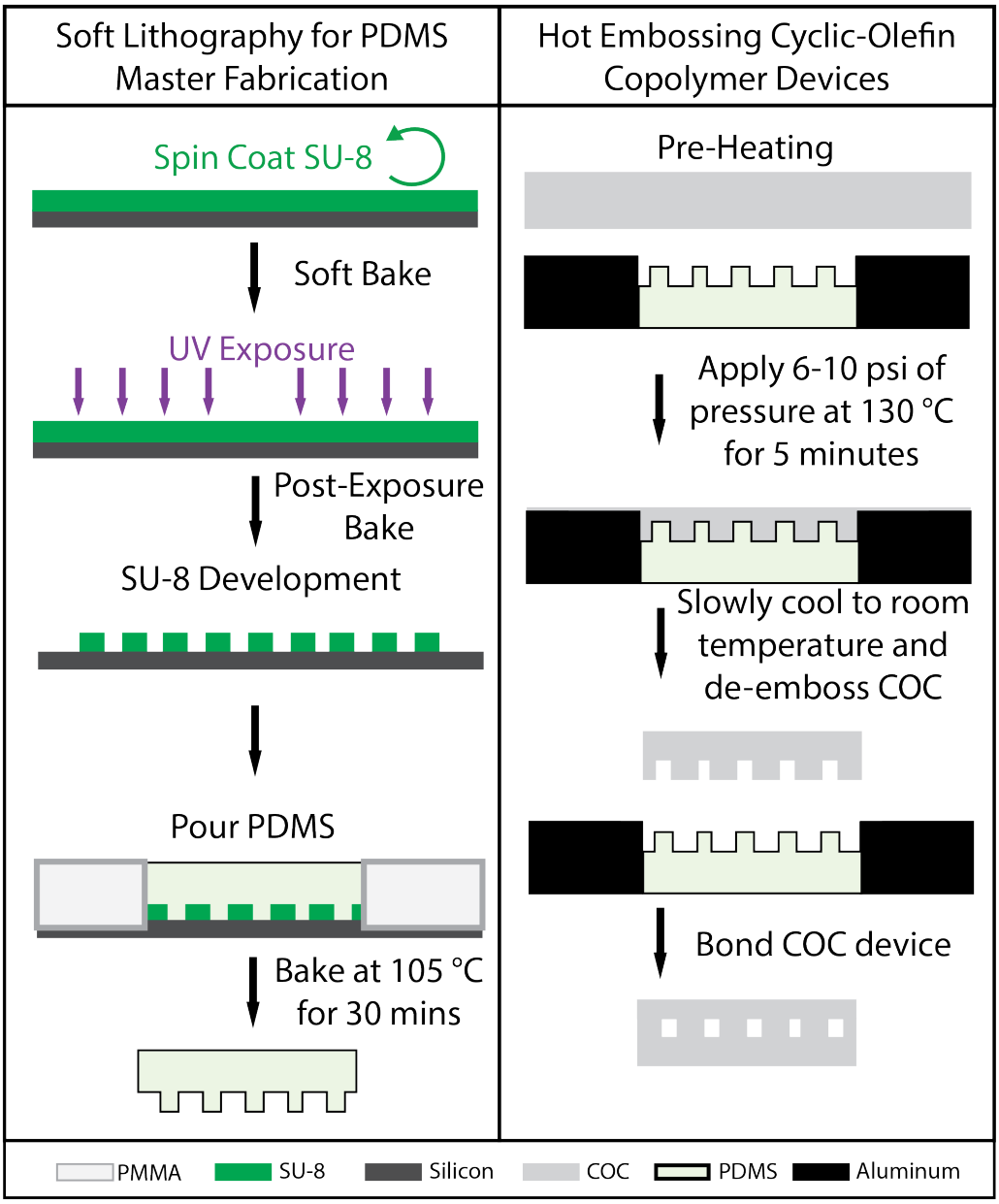


Figure 30: Detailed schematic of the hot embossing fabrication process with the PDMS master mold. This protocol is adapted from Aghvami et al. [27]. (Left) Multi-depth SU-8 photolithography is performed in the cleanroom to create a high-resolution master to form the epoxy mold from. (Middle) The SU-8 master is used to create the PDMS mold. (Right) The PDMS mold is placed in a rigid aluminum frame to prevent lateral expansion during the hot embossing process. Then, the traditional hot embossing process is employed to fabricate the cyclic-olefin copolymer (COC) microfluidic device from the PDMS master mold.

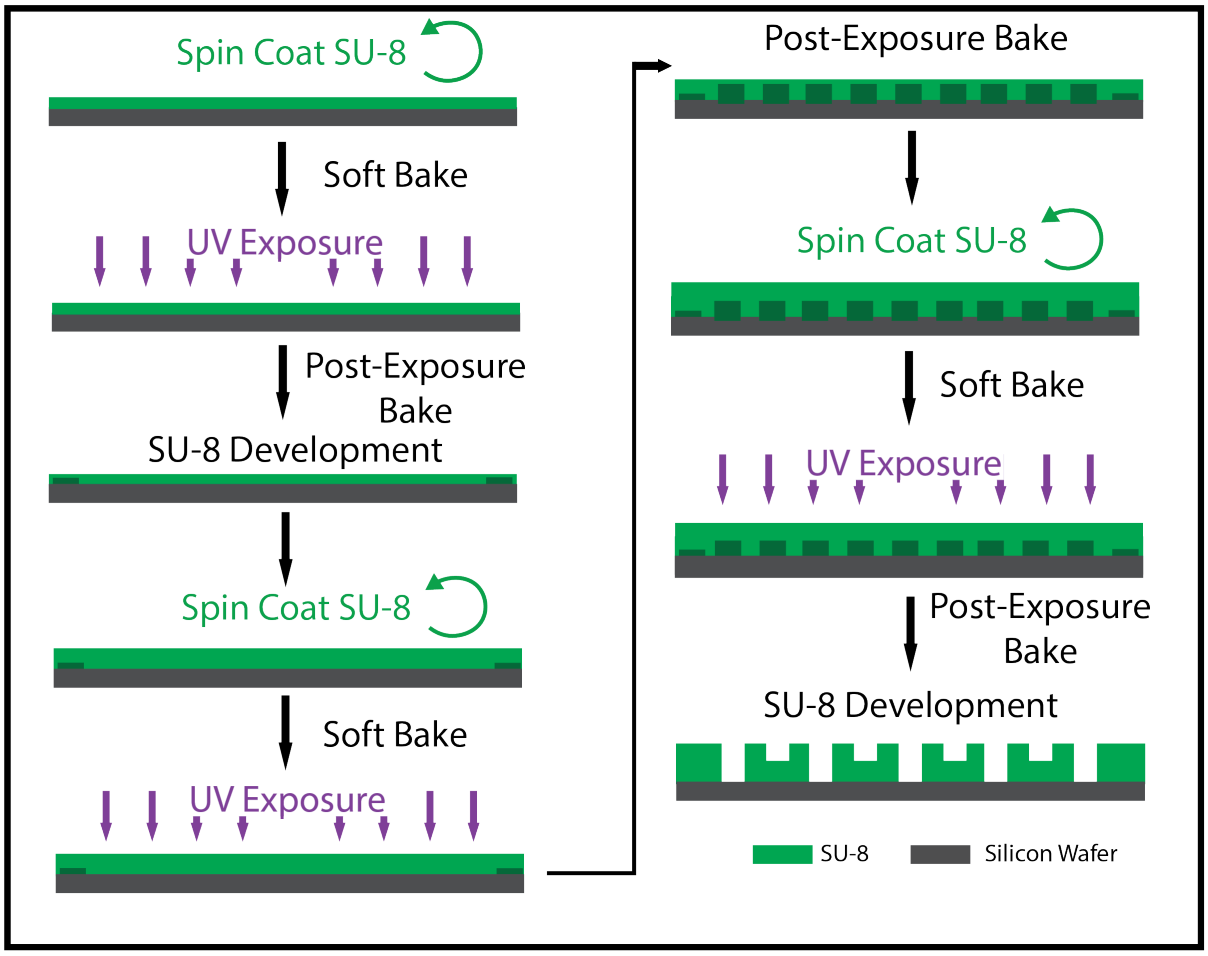


Figure 31: Summary schematic of multi-depth soft-lithography. Multi-depth SU-8 photolithography is performed in the cleanroom to create a high-resolution master to form the epoxy mold from. The first layer patterns alignment markers for the subsequent layer mask, then the second and third layer pattern the features onto the silicon wafer.

Table 4: Multi-Depth Photolithography SU-8 Spin Coating Parameters for Each Layer

Layer 1				
Step	**Spin Speed**	**Ramp Rate**	**Duration**	**Desired Final Thickness**
1	500 rpm	100 rpm/second	10 seconds	5 µm
2	4000 rpm	300 rpm/second	30 seconds	
Layer 2				
Step	**Spin Speed**	**Ramp Rate**	**Duration**	**Desired Final Thickness**
1	500 rpm	100 rpm/second	10 seconds	10 µm
2	3000 rpm	300 rpm/second	30 seconds	
Layer 3				
Step	**Spin Speed**	**Ramp Rate**	**Duration**	**Desired Final Thickness**
1	500 rpm	100 rpm/second	10 seconds	10 µm
2	3000 rpm	300 rpm/second	30 seconds	

for 1 minute followed by 190 seconds at 95 ∘C. The wafer was cooled to room temperature, then developed for 6 minutes with agitation.

Finally, the SU-8 patterned wafer, referred to as the SU-8 master, was coated with a fluoropolymer coating to prevent PDMS adhesion (Oxford Plasmalab System 100, Precursor gas: C_4F_8, ICP power: 500 W, CCP power: 0 W, Time: 10 s).

Surface Characterization of SU-8 Master

To evaluate the dimensional fidelity of the SU-8 master, an optical profilometer was employed (Filmetrics Profilm 3D optical profilometer).

Machining Custom PMMA Frame and Aluminum Frame

A custom aluminum (McMaster-Carr #89015K275) frame and poly (methyl methacrylate) (PMMA) (McMaster-Carr #8560K163) frame were both fabricated using a CNC mill (Nomad 3, Carbide 3D). Fusion 360 (Autodesk) was used for computer aided design (CAD) and computer aided manufacturing (CAM). For machining operations in aluminum, a single-flute ZrN coated carbide end mill was utilized (Carbide 3D, #247Z). For machining operations in PMMA a two-flute carbide end mill was utilized (Carbide 3D, #102E).

Table 5: Summary of parameters for hot embossing COC sheets and pellets using the protocol summarized in Figure 30.

	8007 Sheets	**8007 Pellets**	**6013 Sheets**	**6013 Pellets**
Temperature	90 °C	130 °C	150 °C	180 °C
Pressure	40 psi	40 psi	40 psi	40 psi
Time	300 seconds	300 seconds	300 seconds	300 seconds

PDMS Master Mold Fabrication

First, a 10:1 ratio by weight of Sylgard 184 PDMS Elastomer Base (Dow Silicones Corp., Midland MI) to Sylgard 184 PDMS Elastomer Curing Agent (Dow Silicones Corp., Midland MI) was prepared. It was mixed thoroughly using a widely available, ergonomically optimized, multipronged plastic dispersion tool (i.e., a plastic fork). Then, the mixture was placed in a vacuum desiccator for at least 20 minutes, or until all of the bubbles were gone. The PMMA frame was aligned and secured in place using a high-tension, spring-loaded compression device repurposed from advanced office supply technology (i.e., a binder clip). Then, PDMS was poured into the mold, and a mylar sheet was placed on top of it. Then, a glass slide was used clamped on top of the mold. The whole apparatus was placed in the oven at 105 °C for 30 minutes.

Hot Embossing COC Sheets

Grade 6013 and 8007 COC sheets and pellets (Polyplastics USA) were hot embossed utilizing the protocol developed by Aghvami et al. [27]. A wide range of different pressures between 20 and 120 psi and temperatures between 80 and 230 °C were evaluated to attempt to emboss the COC sheets and pellets. While these ranges of pressures and temperatures were not systematically varied, the parameters that performed the best are shown in Table 5.

Device Characterization

To evaluate the quality of the devices that were fabricated by hot embossing in COC, the field emission scanning electron microscope (Zeiss SUPRA 55VP) at the Imaging and Chemical Analysis Laboratory (ICAL) at Montana State University was used.

Results and Discussion

Soft-Lithography For PDMS Master Fabrication

Multiple-depth photolithography was utilized for the fabrication of the SU-8 master so that unique architectures capable of partitioning individual reactions could be evaluated. However, this was an involved process which required high precision and many protocol iterations to produce a quality master device. The initial base layer was essential for patterning the alignment markers onto the wafer. These markers were then utilized to ensure both of the subsequent layers were aligned in the x, y and theta dimensions. In the next layer, the typical development step was eliminated because it would produce bubbles in the resist, which ruined the subsequent layers pattern. Instead, it was found that the uncured photoresist could be effectively removed with an extended final development step after the last layer was patterned. To validate the dimensional fidelity of the multiple depth SU-8 master, optical profilometry was employed. It was found that both layer 2 and layer 3 were the expected height of 10 μm each (Figure 32).

The custom PMMA clamp apparatus was successful at producing the PDMS master mold for hot embossing. The mylar sheet and glass clamped on top provided a smooth, flat surface for the back of the mold, so that the embossed COC substrate is as flat as possible.

Hot Embossing Using A PDMS Master Mold

PDMS is a soft, malleable polymer, which has advantageous characteristics for many microfluidic applications. However, a material like this would often not be considered a

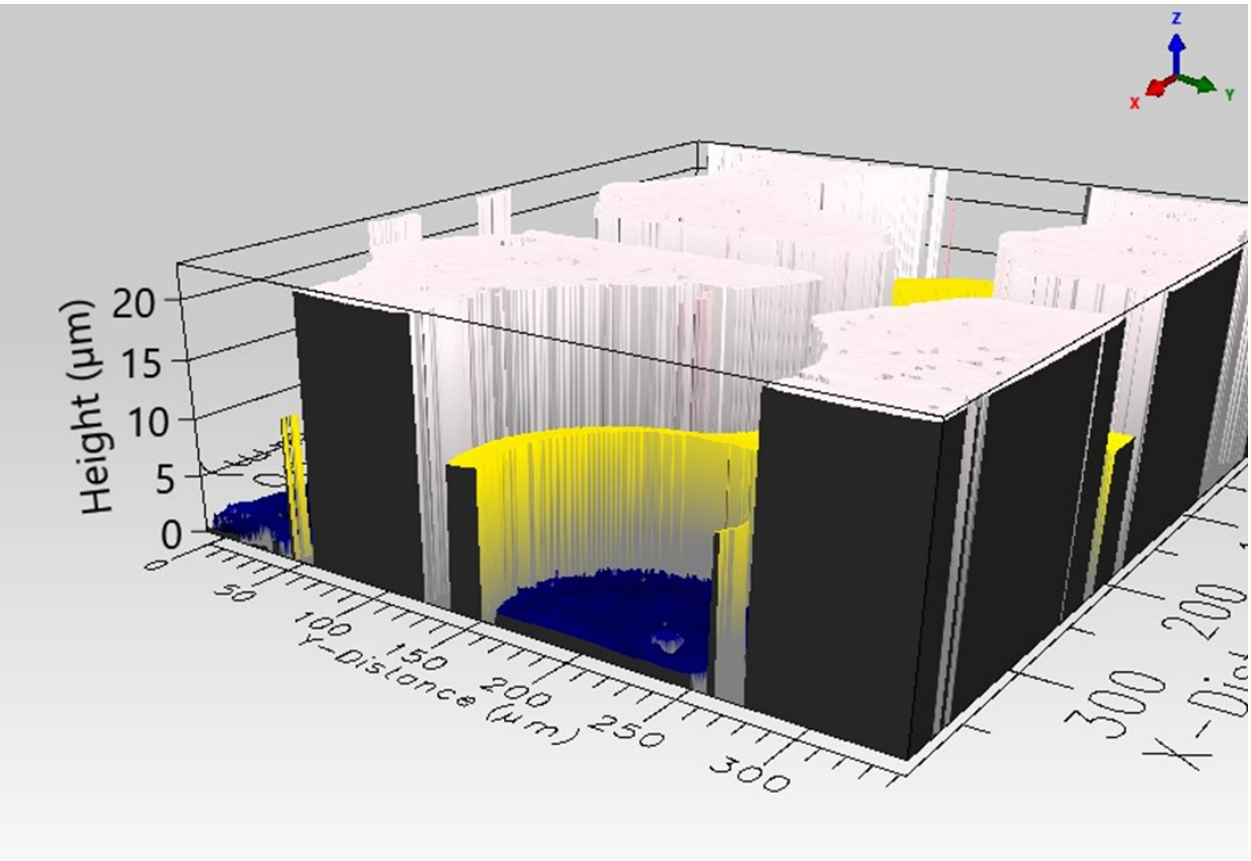


Figure 32: Optical profilometry result of multiple-depth SU-8 master. The two layers of photoresist, displayed in white and yellow, were each designed to be 10 μm in height, which is confirmed by the profilometry measurements.

good option for a hot embossing master mold. But, Aghvami et al. [27] found that the rigid aluminum frame prevented lateral expansion of the PDMS, which allowed them to successfully pattern COC with the PDMS master mold. In this attempt to replicate their method, several issues were encountered. For example, molding the PDMS to have accurate dimensions, so that it fit tightly into the aluminum mold was difficult. The different thermal characteristics of aluminum and PDMS was aggravated at the very high embossing temperatures. As a result, the PDMS mold expanded much quicker than the aluminum frame, which caused the PDMS to crumble under the additional stress while trying to emboss the COC. This expansion was relatively unpredictable, and prototyping was difficult because the production of the PDMS master mold took several hours to produce each one. Despite this, several COC devices were able to be embossed, and images were taken of the devices on the FE-SEM at ICAL at Montana State University (Figure 33). The smallest channels embossed were 20 μm in width and wells that were 90 μm in diameter. These smallest features showed some rounding at the edges of the channels, whereas the largest channels and wells (95 μm in width, 380 μm in diameter) exhibited the sharpest embossed features. The deformation along the edges of the channels is most likely due to the poor rigidity of the PDMS master mold, which can have a significant effect on the fluid flow along the walls of the channels. However, for larger scale features (>100 μm) this effect is much less noticeable, so this may be a viable method for producing COC devices for larger scale applications.

Conclusions and Future Work

Fabrication of microfludic devices in thermoplastics presents a challenge due to the lack of low barrier-to-entry fabrication protocols. Injection molding is inherently a very difficult process to employ in the academic setting due to its high set-up costs, but also for safety concerns with the conditions required. In contrast, several groups have employed hot embossing as a fabrication tool using COC to produce high-quality microfluidic

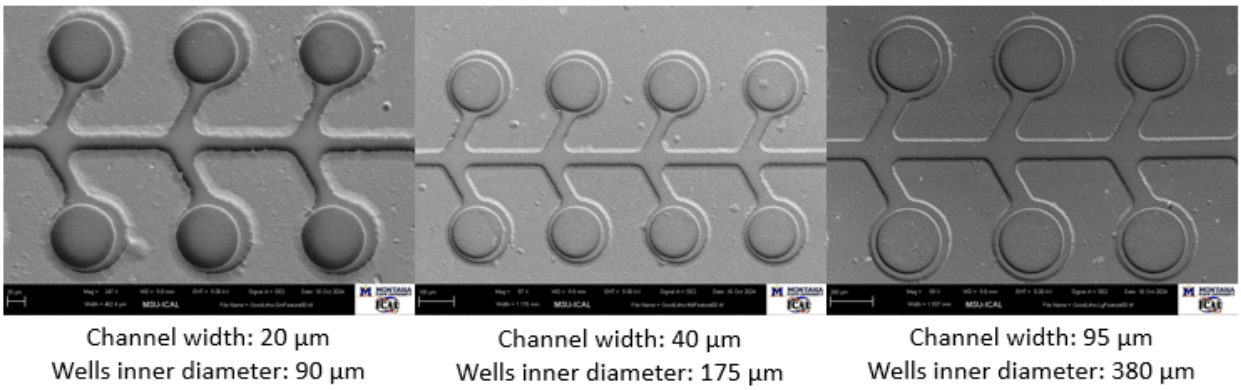


Figure 33: Images of grade 8007 COC hot embossed using a PDMS master. Images were taken using the field emission scanning electron microscope (Zeiss SUPRA 55VP) at the Imaging and Chemical Analysis Laboratory (ICAL) at Montana State University

devices.[24,27] In this chapter, one of these methods is evaluated for producing a hot embossed COC substrate using a PDMS master mold. Unfortunately, PDMS as a master mold produced very inconsistent embossing results and often would fall apart from uneven stresses applied by the hot embossing process. As a result, this method for hot embossing is not going to be utilized going forward.

To increase access and lower the barriers-to-entry for hot embossing thermoplastics for microfluidics, Eden Tech Microfluidics has produced a hot embossing machine, Sublym, which has capabilities for hot embossing a variety of thermoplastics. Additionally, Eden Tech has another product, Epoxym, which can produce an epoxy mold for producing a rigid master mold for patterning substrates. The Epoxym can turn a traditional soft-lithography master made from a photoresist patterned on a silicon wafer into an epoxy mold for hot embossing. Using a rigid epoxy master, in conjunction with the Sublym hot embosser provides a much more reliable alternative method for scalable manufacturing of COC devices. The rigid epoxy mold does not compromise on feature resolution and is advertised to be able to produce features as small as 0.2 μm.[51] The proposed fabrication protocol is shown in Figure 34. In the next stage of this work, it will be evaluated whether the proposed epoxy-based master mold for hot embossing can produce hot embossed COC microfluidic devices for digital

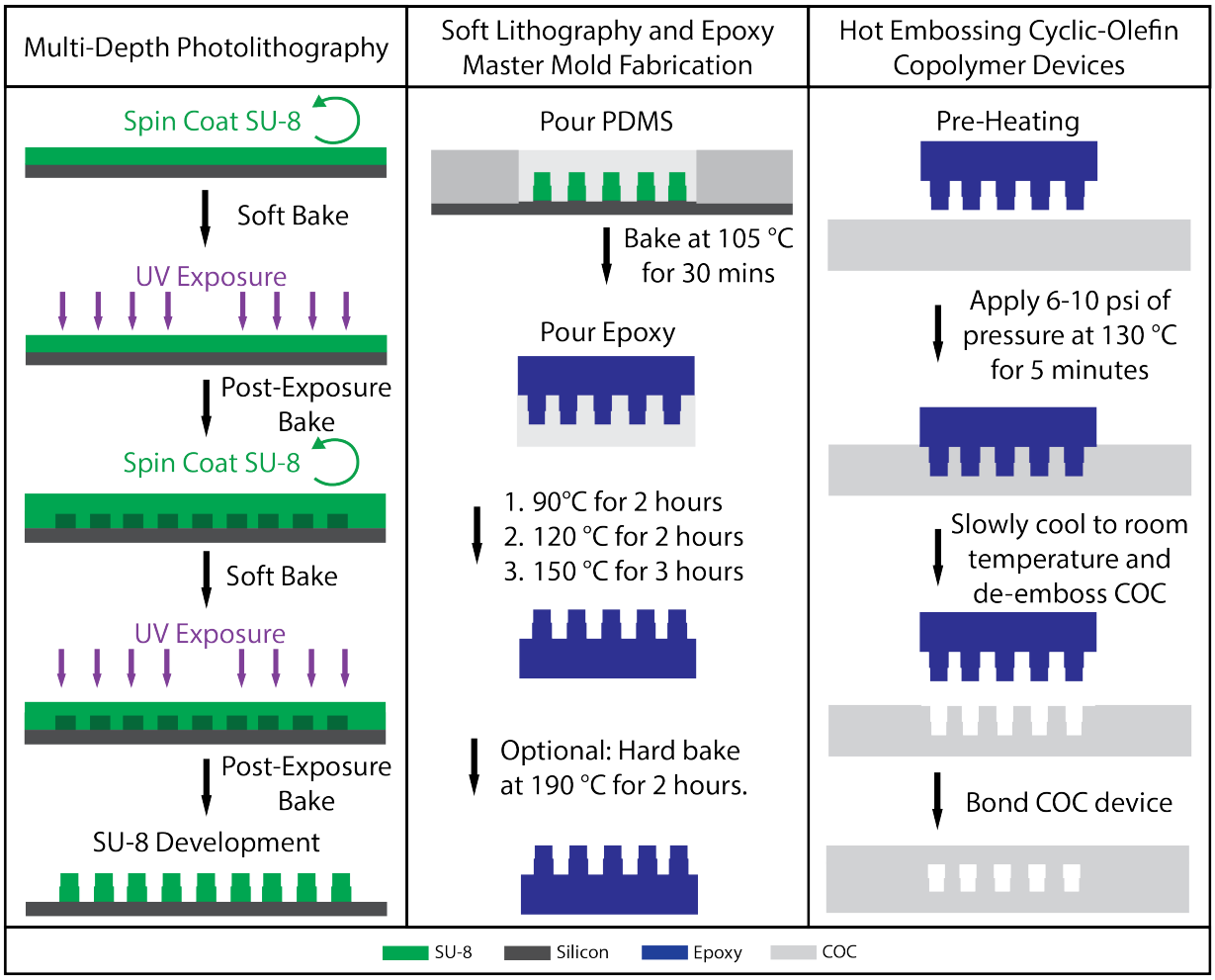


Figure 34: Detailed schematic of the proposed hot embossing fabrication process with the epoxy master mold. (Left) Multi-depth SU-8 photolithography is performed in the cleanroom to create a high-resolution master to form the epoxy mold from. (Middle) The SU-8 master is used to create the epoxy master mold using the Epoxym kit from Eden Tech Microfluidics. (Right) The traditional hot embossing process is employed to fabricate the cyclic-olefin copolymer (COC) microfluidic device from the epoxy master mold.

nucleic acid detection.

CONCLUSIONS

Rapid prototyping workflows enable researchers to develop microfluidic technologies at speeds that are impractical using traditional cleanroom-based methods. However, a fundamental gap persists between the capabilities of most prototyping approaches and the scalability required for industrial or clinical deployment. This thesis explored three complementary fabrication methods—digital light projection (DLP) 3D printing, micromilling in cyclic-olefin copolymer (COC), and hot embossing—with a focus on developing nucleic acid detection assays for point-of-care diagnostics.

DLP 3D printing is widely used in academic settings due to its low cost and accessibility. In this work, a commercially available MiiCraft 50 printer and CADworks Bv007a resin were used to fabricate curved microchannels as small as 100 μm wide. The resin's low viscosity allowed high-resolution features with good optical clarity; however, thermal testing revealed instability above 35 °C, limiting its use for common diagnostic reactions like PCR or LAMP. To address this, post-processing protocols were evaluated to leach inhibitory compounds from the resin. Preliminary results suggest that ethanol and PBS soaking may improve compatibility for lower-temperature reactions such as recombinase polymerase amplification (RPA), although further quantitative analysis is needed.

To bridge the gap between prototyping and clinical translation, a full workflow for rapid micromilling in COC was developed. A method for embossing machinable COC plaques was first established to enable low-cost CNC fabrication. Feed rates and spindle speeds were evaluated for two COC grades (8007 and 6013), with 6013 showing superior thermal resilience and surface quality. Additionally, a custom chip-to-world interface was designed for thermal control and reagent loading, and RPA was successfully performed in bonded COC chips with real-time fluorescence imaging. These results support the feasibility of concurrent device and assay development directly in the end-use material.

While micromilling was an effective fabrication method, there are some limitations that should be discussed. First, dimensional variability was found due to the Nomad 3's open-loop stepper control system. Additionally, micro end mills were found to be prone to tool breakage if there was excessive runout, or if too deep of a cut was taken. Second, while RPA was successfully demonstrated, the current workflow introduced over a 30 minute delay between reagent loading and thermal incubation, which effects the reproducibility and reliability of the RPA reaction. Future work should focus on reducing this delay by implementing a warm-start polymerase, automating the loading procedure, or using less channel ports.

To demonstrate future scalability of the rapid prototyping methods, hot embossing was evaluated as a mid-throughput fabrication method. While some features were successfully transferred into COC, the PDMS mold used during embossing exhibited deformation and breakdown under heat. Therefore, in the future a more robust approach is recommended: fabricating a rigid epoxy mold from a SU-8 master and using it as the mold for hot embossing. This method offers higher durability, improved fidelity, and better reproducibility while still being accessible in academic labs.

In conclusion, this thesis presents reproducible, low barrier-of-entry fabrication workflows for microfluidic devices using commercially available equipment and materials. These methods enable high-resolution prototyping in both 3D printed and thermoplastic platforms, with promising future directions for scaled manufacturing via hot embossing. Together, these methods provide a practical foundation for researchers seeking to integrate molecular diagnostic assays into microfluidic devices designed for translational use.

REFERENCES CITED

[1] T. D. Brock. "The value of basic research: discovery of Thermus aquaticus and other extreme thermophiles". eng. In: *Genetics* 146.4 (Aug. 1997), pp. 1207–1210. ISSN: 0016-6731. doi:10.1093/genetics/146.4.1207.

[2] *Scientific American Volume 262, Issue 4*. en. Apr. 1990. https://www.scientificamerican.com/issue/sa/1990/04-01/ (visited on 05/19/2025).

[3] *Kary B. Mullis – Facts*. en-US. https://www.nobelprize.org/prizes/chemistry/1993/mullis/facts/ (visited on 05/19/2025).

[4] Joe Fore, Ilse R Wiechers, and Robert Cook-Deegan. "The effects of business practices, licensing, and intellectual property on development and dissemination of the polymerase chain reaction: case study". In: *Journal of Biomedical Discovery and Collaboration* 1 (July 2006), p. 7. ISSN: 1747-5333. doi:10.1186/1747-5333-1-7. https://www.ncbi.nlm.nih.gov/pmc/articles/PMC1523369/ (visited on 05/19/2025).

[5] Wing Cheung Mak, Valerio Beni, and Anthony P. F. Turner. "Lateral-flow technology: From visual to instrumental". In: *TrAC Trends in Analytical Chemistry*. Past , Present and Future challenges of Biosensors and Bioanalytical tools in Analytical Chemistry: a tribute to Prof Marco Mascini 79 (May 2016), pp. 297–305. ISSN: 0165-9936. doi:10.1016/j.trac.2015.10.017. https://www.sciencedirect.com/science/article/pii/S0165993615301084 (visited on 05/06/2025).

[6] A. Manz, N. Graber, and H. M. Widmer. "Miniaturized total chemical analysis systems: A novel concept for chemical sensing". In: *Sensors and Actuators B: Chemical* 1.1 (Jan. 1990), pp. 244–248. ISSN: 0925-4005. doi:10.1016/0925-4005(90)80209-I. https://www.sciencedirect.com/science/article/pii/092540059080209I (visited on 05/19/2025).

[7] Martin U. Kopp, Andrew J. de Mello, and Andreas Manz. "Chemical Amplification: Continuous-Flow PCR on a Chip". In: *Science* 280.5366 (May 1998). Publisher: American Association for the Advancement of Science, pp. 1046–1048. doi:10.1126/science.280.5366.1046. https://www.science.org/doi/10.1126/science.280.5366.1046 (visited on 05/27/2025).

[8] David C. Duffy et al. "Rapid Prototyping of Microfluidic Systems in Poly (dimethylsiloxane)". In: *Analytical Chemistry* 70.23 (Dec. 1998). Publisher: American Chemical Society, pp. 4974–4984. ISSN: 0003-2700. doi:10.1021/ac980656z. https://doi.org/10.1021/ac980656z (visited on 05/06/2025).

[9] Kiran Giri and Chia-Wen Tsao. "Recent Advances in Thermoplastic Microfluidic Bonding". en. In: *Micromachines* 13.3 (Mar. 2022), p. 486. doi:10.3390/mi13030486. https://pmc.ncbi.nlm.nih.gov/articles/PMC8949906/ (visited on 10/25/2024).

[10] Michael W. Toepke and David J. Beebe. "PDMS absorption of small molecules and consequences in microfluidic applications". en. In: *Lab on a Chip* 6.12 (Nov. 2006). Publisher:

The Royal Society of Chemistry, pp. 1484–1486. ISSN: 1473-0189. doi:10.1039/B612140C. https://pubs.rsc.org/en/content/articlelanding/2006/lc/b612140c (visited on 05/13/2025).

[11] Rajendrani Mukhopadhyay. "When PDMS isn't the best". In: *Analytical Chemistry* 79.9 (May 2007). Publisher: American Chemical Society, pp. 3248–3253. ISSN: 0003-2700. doi:10.1021/ac071903e. https://doi.org/10.1021/ac071903e (visited on 05/13/2025).

[12] Patrícia Rodrigues et al. *Critical Analysis of the Absorption/Adsorption of Small Molecules by Polydimethylsiloxane in Microfluidic Analytical Devices*. en. SSRN Scholarly Paper. Rochester, NY, Feb. 2022. doi:10.2139/ssrn.4038046. https://papers.ssrn.com/abstract=4038046 (visited on 05/13/2025).

[13] Anthony K. Au et al. "3D-Printed Microfluidics". In: *Angewandte Chemie International Edition* 55.12 (Mar. 2016). Publisher: John Wiley & Sons, Ltd, pp. 3862–3881. ISSN: 1433-7851. doi:10.1002/anie.201504382. https://onlinelibrary.wiley.com/doi/full/10.1002/anie.201504382 (visited on 10/02/2024).

[14] Nurul Mohd Fuad et al. "Characterization of 3D-Printed Moulds for Soft Lithography of Millifluidic Devices". In: *Micromachines* 9.3 (Mar. 2018), p. 116. ISSN: 2072-666X. doi:10.3390/mi9030116. https://www.ncbi.nlm.nih.gov/pmc/articles/PMC6187831/ (visited on 05/08/2025).

[15] Anna V. Nielsen et al. "3D Printed Microfluidics". In: *Annual review of analytical chemistry (Palo Alto, Calif.)* 13.1 (June 2020), pp. 45–65. ISSN: 1936-1327. doi:10.1146/annurev-anchem-091619-102649. https://www.ncbi.nlm.nih.gov/pmc/articles/PMC7282950/ (visited on 05/08/2025).

[16] Kelsey M. Leong et al. "Democratizing Access to Microfluidics: Rapid Prototyping of Open Microchannels with Low-Cost LCD 3D Printers". In: *ACS Omega* 9.45 (Nov. 2024). Publisher: American Chemical Society, pp. 45537–45544. doi:10.1021/acsomega.4c07776. https://doi.org/10.1021/acsomega.4c07776 (visited on 11/12/2024).

[17] Matt D. Nelson et al. "Achieving biocompatibility and tailoring mechanical properties of SLA 3D printed devices for microfluidic and cell culture applications". en. In: *Lab on a Chip* 24.19 (2024). Publisher: Royal Society of Chemistry, pp. 4632–4638. doi:10.1039/D4LC00354C. https://pubs.rsc.org/en/content/articlelanding/2024/lc/d4lc00354c (visited on 04/08/2025).

[18] Lucas C. Duarte et al. "A review of the recent achievements and future trends on 3D printed microfluidic devices for bioanalytical applications". In: *Analytica Chimica Acta* 1299 (Apr. 2024), p. 342429. ISSN: 0003-2670. doi:10.1016/j.aca.2024.342429. https://www.sciencedirect.com/science/article/pii/S0003267024002307 (visited on 05/14/2025).

[19] Charalampos Tzivelekis et al. "Microfluidic chip fabrication and performance analysis of 3D printed material for use in microfluidic nucleic acid amplification applications". en. In: *Journal of Micromechanics and Microengineering* 31.3 (Jan. 2021). Publisher: IOP

Publishing, p. 035005. ISSN: 0960-1317. doi:10.1088/1361-6439/abd9a9. https://dx.doi.org/10.1088/1361-6439/abd9a9 (visited on 05/14/2025).

[20] Laura Schittecatte et al. "From resin formulation and process parameters to the final mechanical properties of 3D printed acrylate materials". en. In: *MRS Communications* 13.3 (June 2023), pp. 357–377. ISSN: 2159-6867. doi:10.1557/s43579-023-00352-3. https://doi.org/10.1557/s43579-023-00352-3 (visited on 05/23/2025).

[21] *Considerations When Switching from PDMS to Thermoplastic Microfluidics*. https://www.edgeprecision.com/news-and-insights/considerations-when-switching-from-pdms-to-thermoplastic-microfluidics?hs_amp=true (visited on 05/08/2025).

[22] *Microfluidics: The Evolution from PDMS to Thermoplastics for Enhanced Scalability and Cost-Effectiveness - Potomac Photonics*. en-US. https://www.potomac-laser.com/blog/microfluidics-the-evolution-from-pdms-to-thermoplastics-for-enhanced-scalability-and-cost-effectiveness/ (visited on 05/08/2025).

[23] Harrison Khoo et al. "Rapid prototyping of thermoplastic microfluidic devices via SLA 3D printing". en. In: *Scientific Reports* 14.1 (July 2024). Publisher: Nature Publishing Group, p. 17646. ISSN: 2045-2322. doi:10.1038/s41598-024-68761-5. https://www.nature.com/articles/s41598-024-68761-5 (visited on 05/08/2025).

[24] Abdulrahman Agha et al. "A Review of Cyclic Olefin Copolymer Applications in Microfluidics and Microdevices". en. In: *Macromolecular Materials and Engineering* 307.8 (2022). ISSN: 1439-2054. doi:10.1002/mame.202200053. https://onlinelibrary.wiley.com/doi/abs/10.1002/mame.202200053 (visited on 05/28/2024).

[25] Albert Folch. *Introduction to BioMEMS*. en. Google-Books-ID: ejrSBQAAQBAJ. CRC Press, Apr. 2016. ISBN: 978-1-4665-0938-2.

[26] Elodie Sollier et al. "Rapid prototyping polymers for microfluidic devices and high pressure injections". en. In: *Lab on a Chip* 11.22 (2011). Publisher: Royal Society of Chemistry, pp. 3752–3765. doi:10.1039/C1LC20514E. https://pubs.rsc.org/en/content/articlelanding/2011/lc/c1lc20514e (visited on 05/19/2025).

[27] S. Ali Aghvami et al. "Rapid prototyping of cyclic olefin copolymer (COC) microfluidic devices". In: *Sensors and Actuators B: Chemical* 247 (Aug. 2017), pp. 940–949. ISSN: 0925-4005. doi:10.1016/j.snb.2017.03.023. https://www.sciencedirect.com/science/article/pii/S0925400517304318 (visited on 05/28/2024).

[28] F Bundgaard, G Perozziello, and O Geschke. "Rapid prototyping tools and methods for all-Topas® cyclic olefin copolymer fluidic microsystems". en. In: *Proceedings of the Institution of Mechanical Engineers, Part C: Journal of Mechanical Engineering Science* 220.11 (Nov. 2006). Publisher: IMECHE, pp. 1625–1632. ISSN: 0954-4062. doi:10.1243/09544062JMES295. https://doi.org/10.1243/09544062JMES295 (visited on 11/07/2024).

[29] Bong Suk Kim et al. “Facile fabrication of plastic template for three-dimensional micromixer-embedded microfluidic device”. en. In: *BioChip Journal* 7.2 (June 2013), pp. 104–111. ISSN: 2092-7843. doi:10.1007/s13206-013-7204-x. https://doi.org/10.1007/s13206-013-7204-x (visited on 11/07/2024).

[30] Pin-Chuan Chen et al. “Micromachining Microchannels on Cyclic Olefin Copolymer (COC) Substrates with the Taguchi Method”. en. In: *Micromachines* 8.9 (Aug. 2017), p. 264. doi:10.3390/mi8090264. https://pmc.ncbi.nlm.nih.gov/articles/PMC6190106/ (visited on 11/07/2024).

[31] David J. Guckenberger et al. “Micromilling: A method for ultra-rapid prototyping of plastic microfluidic devices”. In: *Lab on a chip* 15.11 (June 2015), pp. 2364–2378. ISSN: 1473-0197. doi:10.1039/c5lc00234f. https://www.ncbi.nlm.nih.gov/pmc/articles/PMC4439323/ (visited on 05/19/2025).

[32] Benedikt Emde, Karsten Niehaus, and Lara Tickenbrock. “Evaluation of 3D-Printed Microfluidic Structures for Use in AML-Specific Biomarker Detection of PML::RARA”. en. In: *International Journal of Molecular Sciences* 26.2 (Jan. 2025). Number: 2 Publisher: Multidisciplinary Digital Publishing Institute, p. 497. ISSN: 1422-0067. doi:10.3390/ijms26020497. https://www.mdpi.com/1422-0067/26/2/497 (visited on 05/16/2025).

[33] Hannah. B. Musgrove, Megan. A. Catterton, and Rebecca. R. Pompano. “Applied tutorial for the design and fabrication of biomicrofluidic devices by resin 3D printing”. In: *Analytica Chimica Acta* 1209 (May 2022), p. 339842. ISSN: 0003-2670. doi:10.1016/j.aca.2022.339842. https://www.sciencedirect.com/science/article/pii/S0003267022004135 (visited on 05/16/2025).

[34] Megan E. Dueck et al. “Precision cancer monitoring using a novel, fully integrated, microfluidic array partitioning digital PCR platform”. en. In: *Scientific Reports* 9.1 (Dec. 2019). Publisher: Nature Publishing Group, p. 19606. ISSN: 2045-2322. doi:10.1038/s41598-019-55872-7. https://www.nature.com/articles/s41598-019-55872-7 (visited on 05/17/2024).

[35] Alexandra P. Kuo et al. “High-Precision Stereolithography of Biomicrofluidic Devices”. eng. In: *Advanced Materials Technologies* 4.6 (June 2019), p. 1800395. ISSN: 2365-709X. doi:10.1002/admt.201800395.

[36] M. Neubauer et al. “3D printing on glass for direct sensor integration”. en. In: *Engineering Research Express* 1.2 (Dec. 2019). Publisher: IOP Publishing, p. 025051. ISSN: 2631-8695. doi:10.1088/2631-8695/ab5e9f. https://dx.doi.org/10.1088/2631-8695/ab5e9f (visited on 10/01/2024).

[37] Seren Kecili and H. Cumhur Tekin. “Adhesive bonding strategies to fabricate high-strength and transparent 3D printed microfluidic device”. In: *Biomicrofluidics* 14.2 (Apr. 2020), p. 024113. ISSN: 1932-1058. doi:10.1063/5.0003302. https://www.ncbi.nlm.nih.gov/pmc/articles/PMC7173975/ (visited on 05/22/2025).

[38] Pablo Martínez Cruz et al. “An inexpensive, versatile, compact, programmable temperature controller and thermocycler for simultaneous analysis and visualization within a microscope”. en. In: *Microfluidics and Nanofluidics* 25.5 (Apr. 2021), p. 40. ISSN: 1613-4990. doi:10.1007/s10404-021-02440-z. https://doi.org/10.1007/s10404-021-02440-z (visited on 05/16/2025).

[39] Sajad Razavi Bazaz et al. “3D Printing of Inertial Microfluidic Devices”. en. In: *Scientific Reports* 10.1 (Apr. 2020). Number: 1 Publisher: Nature Publishing Group, p. 5929. ISSN: 2045-2322. doi:10.1038/s41598-020-62569-9. https://www.nature.com/articles/s41598-020-62569-9 (visited on 11/15/2023).

[40] Vi T. Nguyen et al. “Low-Cost Microfluidic Fluorescence-Based Assay for Screening Viral Diseases at the Point of Care”. In: *2024 IEEE Healthcare Innovations and Point of Care Technologies (HI-POCT)*. Sept. 2024, pp. 49–52. doi:10.1109/HI-POCT64255.2024.10876199. https://ieeexplore.ieee.org/abstract/document/10876199 (visited on 05/13/2025).

[41] Laura A. Milton et al. “Vat Photopolymerization 3D printed microfluidic devices for organ-on-a-chip applications”. In: *Lab on a chip* 23.16 (Aug. 2023), pp. 3537–3560. ISSN: 1473-0197. doi:10.1039/d3lc00094j. https://www.ncbi.nlm.nih.gov/pmc/articles/PMC10448871/ (visited on 05/16/2025).

[42] Megan A. Catterton, Alexander G. Ball, and Rebecca R. Pompano. “Rapid Fabrication by Digital Light Processing 3D Printing of a SlipChip with Movable Ports for Local Delivery to Ex Vivo Organ Cultures”. en. In: *Micromachines* 12.8 (Aug. 2021). Number: 8 Publisher: Multidisciplinary Digital Publishing Institute, p. 993. ISSN: 2072-666X. doi:10.3390/mi12080993. https://www.mdpi.com/2072-666X/12/8/993 (visited on 04/22/2024).

[43] Stefan Kefer et al. “Micromilling-assisted fabrication of monolithic polymer ridge-type waveguides with integrated photonic sensing structures”. EN. In: *Optical Materials Express* 11.8 (Aug. 2021). Publisher: Optica Publishing Group, pp. 2389–2400. ISSN: 2159-3930. doi:10.1364/OME.425778. https://opg.optica.org/ome/abstract.cfm?uri=ome-11-8-2389 (visited on 11/07/2024).

[44] *Cervical Cancer Statistics — Key Facts About Cervical Cancer*. en. https://www.cancer.org/cancer/types/cervical-cancer/about/key-statistics.html (visited on 04/10/2025).

[45] MD Anderson News Release. *Cervical cancer rates rising in low-income U.S. counties*. en. https://www.mdanderson.org/newsroom/cervical-cancer-rates-rising-in-low-income-u-s--counties.h00-159694389.html (visited on 04/10/2025).

[46] Ashna Gupta et al. “Prognostic value of circulating HPV cell-free DNA in cervical cancer using liquid biopsy”. en. In: *Scientific Reports* 15.1 (Apr. 2025). Publisher: Nature Publishing Group, p. 11480. ISSN: 2045-2322. doi:10.1038/s41598-025-93152-9. https://www.nature.com/articles/s41598-025-93152-9 (visited on 04/10/2025).

[47] Jia Li, Joanne Macdonald, and Felix von Stetten. “Review: a comprehensive summary of a decade development of the recombinase polymerase amplification”. en. In: *Analyst* 144.1 (Dec. 2018). Publisher: The Royal Society of Chemistry, pp. 31–67. ISSN: 1364-5528. doi:10.1039/C8AN01621F. https://pubs.rsc.org/en/content/articlelanding/2019/an/c8an01621f (visited on 05/01/2025).

[48] I. R. G. Ogilvie et al. “Reduction of surface roughness for optical quality microfluidic devices in PMMA and COC”. en. In: *Journal of Micromechanics and Microengineering* 20.6 (May 2010), p. 065016. ISSN: 0960-1317. doi:10.1088/0960-1317/20/6/065016. https://dx.doi.org/10.1088/0960-1317/20/6/065016 (visited on 11/07/2024).

[49] Robert Keever. *Optimized Machining With Miniature End Mills - In The Loupe*. en-US. July 2020. https://www.harveyperformance.com/in-the-loupe/how-to-optimize-results-while-machining-with-miniature-end-mills/ (visited on 05/19/2025).

[50] I D Johnston et al. “Mechanical characterization of bulk Sylgard 184 for microfluidics and microengineering”. en. In: *Journal of Micromechanics and Microengineering* 24.3 (Feb. 2014). Publisher: IOP Publishing, p. 035017. ISSN: 0960-1317. doi:10.1088/0960-1317/24/3/035017. https://dx.doi.org/10.1088/0960-1317/24/3/035017 (visited on 05/19/2025).

[51] *Epoxym Kit - Microfluidics Mold Solution*. en-US. https://eden-microfluidics.com/epoxym-microfluidics-mold-solution/ (visited on 05/19/2025).

Bibliography

[1] T. D. Brock. "The value of basic research: discovery of Thermus aquaticus and other extreme thermophiles". eng. In: *Genetics* 146.4 (Aug. 1997), pp. 1207–1210. ISSN: 0016-6731. doi:10.1093/genetics/146.4.1207.

[2] *Scientific American Volume 262, Issue 4*. en. Apr. 1990. https://www.scientificamerican.com/issue/sa/1990/04-01/ (visited on 05/19/2025).

[3] *Kary B. Mullis – Facts*. en-US. https://www.nobelprize.org/prizes/chemistry/1993/mullis/facts/ (visited on 05/19/2025).

[4] Joe Fore, Ilse R Wiechers, and Robert Cook-Deegan. "The effects of business practices, licensing, and intellectual property on development and dissemination of the polymerase chain reaction: case study". In: *Journal of Biomedical Discovery and Collaboration* 1 (July 2006), p. 7. ISSN: 1747-5333. doi:10.1186/1747-5333-1-7. https://www.ncbi.nlm.nih.gov/pmc/articles/PMC1523369/ (visited on 05/19/2025).

[5] Wing Cheung Mak, Valerio Beni, and Anthony P. F. Turner. "Lateral-flow technology: From visual to instrumental". In: *TrAC Trends in Analytical Chemistry*. Past , Present and Future challenges of Biosensors and Bioanalytical tools in Analytical Chemistry: a tribute to Prof Marco Mascini 79 (May 2016), pp. 297–305. ISSN: 0165-9936. doi:10.1016/j.trac.2015.10.017. https://www.sciencedirect.com/science/article/pii/S0165993615301084 (visited on 05/06/2025).

[6] A. Manz, N. Graber, and H. M. Widmer. "Miniaturized total chemical analysis systems: A novel concept for chemical sensing". In: *Sensors and Actuators B: Chemical* 1.1 (Jan. 1990), pp. 244–248. ISSN: 0925-4005. doi:10.1016/0925-4005(90)80209-I. https://www.sciencedirect.com/science/article/pii/092540059080209I (visited on 05/19/2025).

[7] Martin U. Kopp, Andrew J. de Mello, and Andreas Manz. "Chemical Amplification: Continuous-Flow PCR on a Chip". In: *Science* 280.5366 (May 1998). Publisher: American Association for the Advancement of Science, pp. 1046–1048. doi:10.1126/science.280.5366.1046. https://www.science.org/doi/10.1126/science.280.5366.1046 (visited on 05/27/2025).

[8] David C. Duffy et al. "Rapid Prototyping of Microfluidic Systems in Poly (dimethylsiloxane)". In: *Analytical Chemistry* 70.23 (Dec. 1998). Publisher: American Chemical Society, pp. 4974–4984. ISSN: 0003-2700. doi:10.1021/ac980656z. https://doi.org/10.1021/ac980656z (visited on 05/06/2025).

[9] Kiran Giri and Chia-Wen Tsao. "Recent Advances in Thermoplastic Microfluidic Bonding". en. In: *Micromachines* 13.3 (Mar. 2022), p. 486. doi:10.3390/mi13030486. https://pmc.ncbi.nlm.nih.gov/articles/PMC8949906/ (visited on 10/25/2024).

[10] Michael W. Toepke and David J. Beebe. "PDMS absorption of small molecules and consequences in microfluidic applications". en. In: *Lab on a Chip* 6.12 (Nov. 2006). Publisher:

The Royal Society of Chemistry, pp. 1484–1486. ISSN: 1473-0189. doi:10.1039/B612140C. ht tps://pubs.rsc.org/en/content/articlelanding/2006/lc/b612140c (visited on 05/13/2025).

[11] Rajendrani Mukhopadhyay. "When PDMS isn't the best". In: *Analytical Chemistry* 79.9 (May 2007). Publisher: American Chemical Society, pp. 3248–3253. ISSN: 0003-2700. doi:10 .1021/ac071903e. https://doi.org/10.1021/ac071903e (visited on 05/13/2025).

[12] Patrícia Rodrigues et al. *Critical Analysis of the Absorption/Adsorption of Small Molecules by Polydimethylsiloxane in Microfluidic Analytical Devices*. en. SSRN Scholarly Paper. Rochester, NY, Feb. 2022. doi:10.2139/ssrn.4038046. https://papers.ssrn.com/abstract =4038046 (visited on 05/13/2025).

[13] Anthony K. Au et al. "3D-Printed Microfluidics". In: *Angewandte Chemie International Edition* 55.12 (Mar. 2016). Publisher: John Wiley & Sons, Ltd, pp. 3862–3881. ISSN: 1433-7851. doi:10.1002/anie.201504382. https://onlinelibrary.wiley.com/doi/full/10.1002/anie.20 1504382 (visited on 10/02/2024).

[14] Nurul Mohd Fuad et al. "Characterization of 3D-Printed Moulds for Soft Lithography of Millifluidic Devices". In: *Micromachines* 9.3 (Mar. 2018), p. 116. ISSN: 2072-666X. doi:10.3 390/mi9030116. https://www.ncbi.nlm.nih.gov/pmc/articles/PMC6187831/ (visited on 05/08/2025).

[15] Anna V. Nielsen et al. "3D Printed Microfluidics". In: *Annual review of analytical chemistry (Palo Alto, Calif.)* 13.1 (June 2020), pp. 45–65. ISSN: 1936-1327. doi:10.1146/annurev-anch em-091619-102649. https://www.ncbi.nlm.nih.gov/pmc/articles/PMC7282950/ (visited on 05/08/2025).

[16] Kelsey M. Leong et al. "Democratizing Access to Microfluidics: Rapid Prototyping of Open Microchannels with Low-Cost LCD 3D Printers". In: *ACS Omega* 9.45 (Nov. 2024). Publisher: American Chemical Society, pp. 45537–45544. doi:10.1021/acsomega.4c07776. https://doi.org/10.1021/acsomega.4c07776 (visited on 11/12/2024).

[17] Matt D. Nelson et al. "Achieving biocompatibility and tailoring mechanical properties of SLA 3D printed devices for microfluidic and cell culture applications". en. In: *Lab on a Chip* 24.19 (2024). Publisher: Royal Society of Chemistry, pp. 4632–4638. doi:10.1039/D4LC00354C. ht tps://pubs.rsc.org/en/content/articlelanding/2024/lc/d4lc00354c (visited on 04/08/2025).

[18] Lucas C. Duarte et al. "A review of the recent achievements and future trends on 3D printed microfluidic devices for bioanalytical applications". In: *Analytica Chimica Acta* 1299 (Apr. 2024), p. 342429. ISSN: 0003-2670. doi:10.1016/j.aca.2024.342429. https://www.sciencedirec t.com/science/article/pii/S0003267024002307 (visited on 05/14/2025).

[19] Charalampos Tzivelekis et al. "Microfluidic chip fabrication and performance analysis of 3D printed material for use in microfluidic nucleic acid amplification applications". en. In: *Journal of Micromechanics and Microengineering* 31.3 (Jan. 2021). Publisher: IOP

Publishing, p. 035005. ISSN: 0960-1317. doi:10.1088/1361-6439/abd9a9. https://dx.doi.org/10.1088/1361-6439/abd9a9 (visited on 05/14/2025).

[20] Laura Schittecatte et al. "From resin formulation and process parameters to the final mechanical properties of 3D printed acrylate materials". en. In: *MRS Communications* 13.3 (June 2023), pp. 357–377. ISSN: 2159-6867. doi:10.1557/s43579-023-00352-3. https://doi.org/10.1557/s43579-023-00352-3 (visited on 05/23/2025).

[21] *Considerations When Switching from PDMS to Thermoplastic Microfluidics*. https://www.edgeprecision.com/news-and-insights/considerations-when-switching-from-pdms-to-thermoplastic-microfluidics?hs_amp=true (visited on 05/08/2025).

[22] *Microfluidics: The Evolution from PDMS to Thermoplastics for Enhanced Scalability and Cost-Effectiveness - Potomac Photonics*. en-US. https://www.potomac-laser.com/blog/microfluidics-the-evolution-from-pdms-to-thermoplastics-for-enhanced-scalability-and-cost-effectiveness/ (visited on 05/08/2025).

[23] Harrison Khoo et al. "Rapid prototyping of thermoplastic microfluidic devices via SLA 3D printing". en. In: *Scientific Reports* 14.1 (July 2024). Publisher: Nature Publishing Group, p. 17646. ISSN: 2045-2322. doi:10.1038/s41598-024-68761-5. https://www.nature.com/articles/s41598-024-68761-5 (visited on 05/08/2025).

[24] Abdulrahman Agha et al. "A Review of Cyclic Olefin Copolymer Applications in Microfluidics and Microdevices". en. In: *Macromolecular Materials and Engineering* 307.8 (2022). ISSN: 1439-2054. doi:10.1002/mame.202200053. https://onlinelibrary.wiley.com/doi/abs/10.1002/mame.202200053 (visited on 05/28/2024).

[25] Albert Folch. *Introduction to BioMEMS*. en. Google-Books-ID: ejrSBQAAQBAJ. CRC Press, Apr. 2016. ISBN: 978-1-4665-0938-2.

[26] Elodie Sollier et al. "Rapid prototyping polymers for microfluidic devices and high pressure injections". en. In: *Lab on a Chip* 11.22 (2011). Publisher: Royal Society of Chemistry, pp. 3752–3765. doi:10.1039/C1LC20514E. https://pubs.rsc.org/en/content/articlelanding/2011/lc/c1lc20514e (visited on 05/19/2025).

[27] S. Ali Aghvami et al. "Rapid prototyping of cyclic olefin copolymer (COC) microfluidic devices". In: *Sensors and Actuators B: Chemical* 247 (Aug. 2017), pp. 940–949. ISSN: 0925-4005. doi:10.1016/j.snb.2017.03.023. https://www.sciencedirect.com/science/article/pii/S0925400517304318 (visited on 05/28/2024).

[28] F Bundgaard, G Perozziello, and O Geschke. "Rapid prototyping tools and methods for all-Topas® cyclic olefin copolymer fluidic microsystems". en. In: *Proceedings of the Institution of Mechanical Engineers, Part C: Journal of Mechanical Engineering Science* 220.11 (Nov. 2006). Publisher: IMECHE, pp. 1625–1632. ISSN: 0954-4062. doi:10.1243/09544062JMES295. https://doi.org/10.1243/09544062JMES295 (visited on 11/07/2024).

[29] Bong Suk Kim et al. “Facile fabrication of plastic template for three-dimensional micromixer-embedded microfluidic device”. en. In: *BioChip Journal* 7.2 (June 2013), pp. 104–111. ISSN: 2092-7843. doi:10.1007/s13206-013-7204-x. https://doi.org/10.1007/s13206-013-7204-x (visited on 11/07/2024).

[30] Pin-Chuan Chen et al. “Micromachining Microchannels on Cyclic Olefin Copolymer (COC) Substrates with the Taguchi Method”. en. In: *Micromachines* 8.9 (Aug. 2017), p. 264. doi:10.3390/mi8090264. https://pmc.ncbi.nlm.nih.gov/articles/PMC6190106/ (visited on 11/07/2024).

[31] David J. Guckenberger et al. “Micromilling: A method for ultra-rapid prototyping of plastic microfluidic devices”. In: *Lab on a chip* 15.11 (June 2015), pp. 2364–2378. ISSN: 1473-0197. doi:10.1039/c5lc00234f. https://www.ncbi.nlm.nih.gov/pmc/articles/PMC4439323/ (visited on 05/19/2025).

[32] Benedikt Emde, Karsten Niehaus, and Lara Tickenbrock. “Evaluation of 3D-Printed Microfluidic Structures for Use in AML-Specific Biomarker Detection of PML::RARA”. en. In: *International Journal of Molecular Sciences* 26.2 (Jan. 2025). Number: 2 Publisher: Multidisciplinary Digital Publishing Institute, p. 497. ISSN: 1422-0067. doi:10.3390/ijms26020497. https://www.mdpi.com/1422-0067/26/2/497 (visited on 05/16/2025).

[33] Hannah. B. Musgrove, Megan. A. Catterton, and Rebecca. R. Pompano. “Applied tutorial for the design and fabrication of biomicrofluidic devices by resin 3D printing”. In: *Analytica Chimica Acta* 1209 (May 2022), p. 339842. ISSN: 0003-2670. doi:10.1016/j.aca.2022.339842. https://www.sciencedirect.com/science/article/pii/S0003267022004135 (visited on 05/16/2025).

[34] Megan E. Dueck et al. “Precision cancer monitoring using a novel, fully integrated, microfluidic array partitioning digital PCR platform”. en. In: *Scientific Reports* 9.1 (Dec. 2019). Publisher: Nature Publishing Group, p. 19606. ISSN: 2045-2322. doi:10.1038/s41598-019-55872-7. https://www.nature.com/articles/s41598-019-55872-7 (visited on 05/17/2024).

[35] Alexandra P. Kuo et al. “High-Precision Stereolithography of Biomicrofluidic Devices”. eng. In: *Advanced Materials Technologies* 4.6 (June 2019), p. 1800395. ISSN: 2365-709X. doi:10.1002/admt.201800395.

[36] M. Neubauer et al. “3D printing on glass for direct sensor integration”. en. In: *Engineering Research Express* 1.2 (Dec. 2019). Publisher: IOP Publishing, p. 025051. ISSN: 2631-8695. doi:10.1088/2631-8695/ab5e9f. https://dx.doi.org/10.1088/2631-8695/ab5e9f (visited on 10/01/2024).

[37] Seren Kecili and H. Cumhur Tekin. “Adhesive bonding strategies to fabricate high-strength and transparent 3D printed microfluidic device”. In: *Biomicrofluidics* 14.2 (Apr. 2020), p. 024113. ISSN: 1932-1058. doi:10.1063/5.0003302. https://www.ncbi.nlm.nih.gov/pmc/articles/PMC7173975/ (visited on 05/22/2025).

[38] Pablo Martínez Cruz et al. “An inexpensive, versatile, compact, programmable temperature controller and thermocycler for simultaneous analysis and visualization within a microscope”. en. In: *Microfluidics and Nanofluidics* 25.5 (Apr. 2021), p. 40. ISSN: 1613-4990. doi:10.1007/s10404-021-02440-z. https://doi.org/10.1007/s10404-021-02440-z (visited on 05/16/2025).

[39] Sajad Razavi Bazaz et al. “3D Printing of Inertial Microfluidic Devices”. en. In: *Scientific Reports* 10.1 (Apr. 2020). Number: 1 Publisher: Nature Publishing Group, p. 5929. ISSN: 2045-2322. doi:10.1038/s41598-020-62569-9. https://www.nature.com/articles/s41598-020-62569-9 (visited on 11/15/2023).

[40] Vi T. Nguyen et al. “Low-Cost Microfluidic Fluorescence-Based Assay for Screening Viral Diseases at the Point of Care”. In: *2024 IEEE Healthcare Innovations and Point of Care Technologies (HI-POCT)*. Sept. 2024, pp. 49–52. doi:10.1109/HI-POCT64255.2024.10876199. https://ieeexplore.ieee.org/abstract/document/10876199 (visited on 05/13/2025).

[41] Laura A. Milton et al. “Vat Photopolymerization 3D printed microfluidic devices for organ-on-a-chip applications”. In: *Lab on a chip* 23.16 (Aug. 2023), pp. 3537–3560. ISSN: 1473-0197. doi:10.1039/d3lc00094j. https://www.ncbi.nlm.nih.gov/pmc/articles/PMC10448871/ (visited on 05/16/2025).

[42] Megan A. Catterton, Alexander G. Ball, and Rebecca R. Pompano. “Rapid Fabrication by Digital Light Processing 3D Printing of a SlipChip with Movable Ports for Local Delivery to Ex Vivo Organ Cultures”. en. In: *Micromachines* 12.8 (Aug. 2021). Number: 8 Publisher: Multidisciplinary Digital Publishing Institute, p. 993. ISSN: 2072-666X. doi:10.3390/mi12080993. https://www.mdpi.com/2072-666X/12/8/993 (visited on 04/22/2024).

[43] Stefan Kefer et al. “Micromilling-assisted fabrication of monolithic polymer ridge-type waveguides with integrated photonic sensing structures”. EN. In: *Optical Materials Express* 11.8 (Aug. 2021). Publisher: Optica Publishing Group, pp. 2389–2400. ISSN: 2159-3930. doi:10.1364/OME.425778. https://opg.optica.org/ome/abstract.cfm?uri=ome-11-8-2389 (visited on 11/07/2024).

[44] *Cervical Cancer Statistics — Key Facts About Cervical Cancer*. en. https://www.cancer.org/cancer/types/cervical-cancer/about/key-statistics.html (visited on 04/10/2025).

[45] MD Anderson News Release. *Cervical cancer rates rising in low-income U.S. counties*. en. https://www.mdanderson.org/newsroom/cervical-cancer-rates-rising-in-low-income-u-s--counties.h00-159694389.html (visited on 04/10/2025).

[46] Ashna Gupta et al. “Prognostic value of circulating HPV cell-free DNA in cervical cancer using liquid biopsy”. en. In: *Scientific Reports* 15.1 (Apr. 2025). Publisher: Nature Publishing Group, p. 11480. ISSN: 2045-2322. doi:10.1038/s41598-025-93152-9. https://www.nature.com/articles/s41598-025-93152-9 (visited on 04/10/2025).

[47] Jia Li, Joanne Macdonald, and Felix von Stetten. “Review: a comprehensive summary of a decade development of the recombinase polymerase amplification”. en. In: *Analyst* 144.1 (Dec. 2018). Publisher: The Royal Society of Chemistry, pp. 31–67. ISSN: 1364-5528. doi:10.1039/C8AN01621F. https://pubs.rsc.org/en/content/articlelanding/2019/an/c8an01621f (visited on 05/01/2025).

[48] I. R. G. Ogilvie et al. “Reduction of surface roughness for optical quality microfluidic devices in PMMA and COC”. en. In: *Journal of Micromechanics and Microengineering* 20.6 (May 2010), p. 065016. ISSN: 0960-1317. doi:10.1088/0960-1317/20/6/065016. https://dx.doi.org/10.1088/0960-1317/20/6/065016 (visited on 11/07/2024).

[49] Robert Keever. *Optimized Machining With Miniature End Mills - In The Loupe*. en-US. July 2020. https://www.harveyperformance.com/in-the-loupe/how-to-optimize-results-while-machining-with-miniature-end-mills/ (visited on 05/19/2025).

[50] I D Johnston et al. “Mechanical characterization of bulk Sylgard 184 for microfluidics and microengineering”. en. In: *Journal of Micromechanics and Microengineering* 24.3 (Feb. 2014). Publisher: IOP Publishing, p. 035017. ISSN: 0960-1317. doi:10.1088/0960-1317/24/3/035017. https://dx.doi.org/10.1088/0960-1317/24/3/035017 (visited on 05/19/2025).

[51] *Epoxym Kit - Microfluidics Mold Solution*. en-US. https://eden-microfluidics.com/epoxym-microfluidics-mold-solution/ (visited on 05/19/2025).